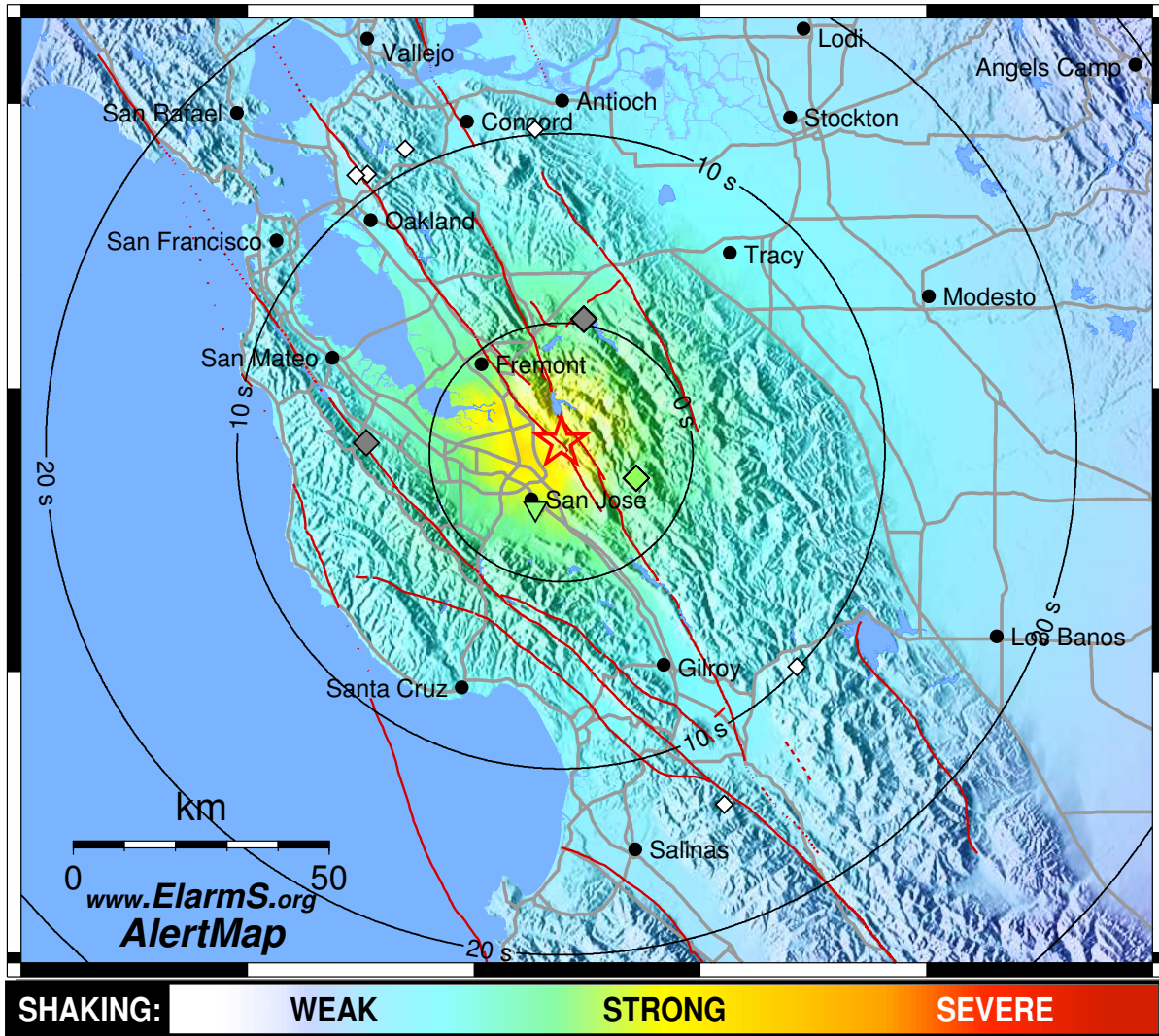


Berkeley Seismological Laboratory



Annual Report July 2007 - June 2008

Berkeley Seismological Laboratory
Annual Report
July 2007 - June 2008

Cover Picture

Alum Rock AlertMap: On October 30, 2007 the magnitude 5.4 Alum Rock earthquake rippled across the San Francisco Bay Area. The largest earthquake in the region since the 1989 Loma Prieta earthquake, it was felt by most people but caused little damage. The CISN early warning test system named ElarmS caught the earthquake. This map shows the distribution of ground shaking intensity predicted using the first few seconds of data recorded by seismometers near the epicenter in San Jose. The epicenter is shown as a star and the estimated magnitude is 5.2.

The warmer colors show where the stronger shaking was predicted near the epicenter and the cooler colors show weaker shaking at greater distances. The predicted ground shaking is very accurate. The data used to generate this map was available a few seconds before the shaking was felt in San Francisco. (This picture is a simplified version of Figure 2.59 in Research Study 26.)

Contents

1	Director's Report	1
1.	Introduction	1
2.	Background and Facilities	1
3.	Highlights of 2007-2008	3
4.	BSL staff news	4
5.	Acknowledgements	5
2	Research Studies	7
1.	Stress preconditioning and magma chamber pressure evolution at Piton de la Fournaise	8
2.	Rigid Block Motion, Interseismic Strain, and Backarc Deformation in the Aegean	10
3.	Linking faults: Subsurface creep directly connecting the Hayward and Calaveras faults	12
4.	No Apparent Accelerating Moment Release in Areas of High Stress	14
5.	Probing the Rheology of Tibet using Postseismic Motion from Large Earthquakes	16
6.	Automated Time-Domain Spike Identification for MT Data	18
7.	Stress Changes on the Sunda Megathrust Preceding the M_w 8.4 2007 Earthquake	21
8.	GPS exploration of the elastic properties across and within the Northern San Andreas Fault zone and heterogeneous elastic dislocation models	23
9.	A look in the eyes of hurricanes by Global Positioning System	26
10.	Observations of Infragravity Waves at the Endeavour Ocean Bottom Broadband Seismic Station (KEBB)	28
11.	Western USA mantle structure and its implications for mantle convection processes	30
12.	A simple method for improving crustal corrections in waveform tomography	33
13.	Effects of water on seismic attenuation	36
14.	Analysis of Long-Period Noise at the Farallon Islands Broadband Seismic Station FARB	38
15.	Tomography of the Alpine Region from Observations of Seismic Ambient Noise	40
16.	3-D Isotropic and Anisotropic S-velocity Structure in North America	42
17.	Towards Regional tomography using the Spectral Element Method	45
18.	A Brief Review of Observation of the Slichter Mode	48
19.	What Does a Waveform Obtained by Correlation of a Diffuse Anisotropic Wavefield Contain?	50
20.	Measurement and implications of frequency dependence of attenuation	52
21.	Nonvolcanic tremor activity modified by the 2003 M6.5 San Simeon and 2004 M6.5 Parkfield, California earthquakes	54
22.	Mapping the Rupture of the M_w 5.4 Alum Rock Earthquake	56
23.	Moment Tensors for Very Long Period Signals at Etna Volcano, Italy	58
24.	Source Analysis of the February 24, 2008 M6 Wells, Nevada Earthquake	60
25.	Triggering effect of $M > 4$ earthquakes on the observed occurrence of repeating events at Parkfield	62
26.	Realtime Test of the ElarmS Earthquake Early Warning Methodology	64
27.	Testing the ElarmS Methodology on Japanese Earthquakes	66
28.	Detection of Low-Frequency Earthquakes in the non-volcanic tremor beneath the San Andreas Fault: a prospective tool for investigating deep fault dynamics?	68
29.	Apparent Stress and Corner Frequency Variations in the 1999 Taiwan (Chi-Chi) Sequence	71
30.	Source Analysis of the Crandall Canyon, Utah, Mine Collapse	73
31.	Interactions Between Early Earthquake Slip History and Final Magnitude	75
32.	Correlated Changes in Nonvolcanic Tremor, Seismic Velocity and Fault Displacement Associated with the 2003 San Simeon and 2004 Parkfield Earthquakes.	78

33.	Moderate earthquake ground motion validation in the San Francisco Bay Area	80
34.	Recalibrating M_L for CISN	83
35.	Seismic Deployments across the Pacific Northwest	85
36.	TMTS, the interactive moment tensor review interface, and the Berkeley Moment Tensor Catalog	87
3	BSL Operations	91
1.	Berkeley Digital Seismic Network	93
2.	California Integrated Seismic Network	103
3.	Northern Hayward Fault Network	109
4.	Parkfield Borehole Network (HRSN)	118
5.	Bay Area Regional Deformation Network	127
6.	Northern California Earthquake Data Center	135
7.	Data Acquisition and Quality Control	145
8.	Northern California Earthquake Monitoring	149
9.	Instrumentation Testing	155
10.	Outreach and Educational Activities	161
	Glossary	163
	Appendix I Publications, Presentations, and Panels 2007-2008	165
	Appendix II Seminar Speakers 2007-2008	176
	Appendix III Organization Chart 2007-2008	178

Chapter 1

Director's Report

1. Introduction

During the year 2007-2008, we experienced the largest earthquake in the San Francisco Bay Area since the M 6.9 1989 Loma Prieta earthquake. The M_w 5.4 Alum Rock earthquake occurring in the evening of October 30, 2007, local time, was felt widely. It caused surprisingly little damage, however, because its epicenter lay to the south-east of the population centers, and it ruptured southward, away from them. This was a gentle reminder that we live in earthquake country, as well as a good opportunity to test the performance of the Northern California earthquake notification system which we operate jointly with the US Geological Survey in Menlo Park, and that of the Early Warning System currently being tested at the BSL. In contrast, this past year was also marked by the tragic M_w 7.8 Sichuan Earthquake (May 12, 2008), which caused 70,000 deaths and 4.8 million homeless, the largest earthquake in China since the 1976 Tangshan earthquake. This earthquake occurred at the eastern boundary of the Tibet Plateau. It is now the subject of intense geophysical study, as it is thought to hold some important keys to the nature of the tectonics and crustal structure of this remarkable region of the world. Researchers at the BSL are actively studying this earthquake.

For those of you familiar with our Annual Report, please skip the background section, which provides a historical introduction to the BSL and has not changed significantly from past years.

2. Background and Facilities

The Berkeley Seismological Laboratory (BSL), formerly the Berkeley Seismographic Stations (BSS), is the oldest Organized Research Unit (ORU) on the UC Berkeley campus. Its mission is unique in that, in addition to research and education in seismology and earthquake-related science, it is responsible for providing timely information on earthquakes (particularly those that occur in Northern and Central California) to the UC Berkeley constituency, the general public, and various local and state government and private organizations. The BSL

is therefore both a research center and a facility/data resource, which sets it apart from most other ORUs. A major component of our activities is focused on developing and maintaining several regional observational networks, and participating, along with other agencies, in various aspects of the collection, analysis, archival, and distribution of data pertaining to earthquakes. At the same time, we maintain a vigorous research program on earthquake processes and Earth structure. In addition, the BSL staff spends considerable time on public relations activities, including tours, talks to public groups, responding to public inquiries about earthquakes, and, more recently, World-Wide-Web presence (<http://seismo.berkeley.edu/>).

UC Berkeley installed the first seismograph in the Western Hemisphere at Mount Hamilton (MHC) in 1887. Since then, it has played a leading role in the operation of state-of-the-art seismic instruments and in the development of advanced methods for seismic data analysis and interpretation. Notably, the installation, starting in 1927, of Wood-Anderson seismographs at 4 locations in Northern California (BKS, ARC, MIN and MHC) allowed the accurate determination of local earthquake magnitude (M_L). This was the beginning of a unique historical catalog of regional earthquakes, which continues to grow, providing crucial input to earthquake probabilities studies.

Over the years, the BSS continued to keep apace of technological improvements. The first centrally telemetered network using phone lines in an active seismic region was installed by the BSS in 1960. The BSS was the first institution in California to operate a 3-component "broadband" system (1963). Notably, the BSS played a major role in the early characterization of earthquake sources using "moment tensors" and source-time functions, and made important contributions to the early definitions of detection/discrimination of underground nuclear tests and to earthquake hazards work, jointly with UCB Engineering. Starting in 1986, the BSS acquired 4 state-of-the-art broadband instruments (STS-1), while simultaneously developing PC-based digital telemetry, albeit with limited resources. As telecommunica-

tion and computer technologies made rapid progress, in parallel with broadband instrument development, paper record reading was soon completely abandoned in favor of largely automated digital data analysis.

The current facilities of the BSL have been progressively built over the past two decades, initiated by significant “upgrade” funding from UC Berkeley in 1991-1995. The BSL currently operates and acquires data, continuously and in real-time, from over 60 regional observatories, which house a combination of broadband and strong motion seismic instrumentation installed in vaults, borehole seismic instrumentation, permanent GPS stations of the Bay Area Regional Deformation (BARD) network, and electromagnetic sensors. The seismic data are fed into the BSL real-time processing and analysis system and are used in conjunction with data from the USGS NCSN network in the joint earthquake notification program for Northern California, started in 1996. This program capitalizes on the complementary capabilities of the networks operated by each institution to provide rapid and reliable information on the location, size and other relevant source parameters of regional earthquakes. In recent years, a major emphasis in BSL instrumentation has been in densifying the state-of-the-art seismic and geodetic networks. A second important focus of research has been the development of robust methods for quasi-real time, automatic determination of earthquake source parameters, and predicting strong ground motion, using a sparse network combining broadband and strong motion seismic sensors, as well as permanent geodetic GPS receivers. A recent emphasis has been the development of “earthquake early warning” capabilities.

The backbone of the BSL operations is a regional network of 32 digital broadband and strong motion seismic stations, the Berkeley Digital Seismic Network (BDSN), with continuous telemetry to UC Berkeley. This network provides the basic regional data for the real-time estimation of location, size and rupture parameters for earthquakes of M 3 and larger in Central and Northern California, within our Rapid Earthquake Data Integration (REDI) program. It is the Berkeley contribution to the California Integrated Seismic Network (CISN). It also provides a fundamental database for the investigation of three-dimensional crustal structure and its effects on regional seismic wave propagation, which is ultimately crucial for estimating ground shaking for future earthquakes. Most stations also record auxiliary temperature/pressure channels, valuable in particular for background noise quality control. Complementing this network is a ~ 25 station “high-resolution” network of borehole seismic sensors located along the Hayward Fault (HFN) and under the Bay Area bridges, operated jointly with the USGS/Menlo Park and linked to the Bridge Safety Project of the California Department of Transportation (Caltrans). The latter has facilitated the in-

stallation of sensor packages at 15 bedrock boreholes along 5 East Bay bridges in collaboration with Lawrence Livermore National Laboratory (LLNL). A major science goal of this network is to collect high signal-to-noise data for micro-earthquakes along the Hayward Fault to gain insight into the physics that govern fault rupture and its nucleation. The BSL is also involved in the operation and maintenance of the 13 element Parkfield borehole seismic array (HRSN), which is providing high quality data on micro-earthquakes, clusters, and, most recently, tremors, and provides an important reference for the San Andreas Fault Observatory at Depth (SAFOD). Since April 2002, the BSL is also involved in the operation of a permanent broadband ocean bottom station, MOBB, in collaboration with the Monterey Bay Aquarium Research Institute (MBARI).

In addition to the seismic networks, the BSL archives and distributes data for the permanent geodetic BARD Network as well as operating and maintaining 30 sites and processing the data from them. Whenever possible, BARD sites are collocated with BDSN sites in order to minimize telemetry costs. In particular, sites continue to be upgraded to 1 Hz sampling. This benefits the development of analysis methods which combine seismic and geodetic data for the rapid estimation of the source parameters of significant earthquakes, which is one focus of BSL research.

Finally, two of the BDSN stations (PKD, SAO) also share data acquisition and telemetry with 5-component electromagnetic sensors installed with the goal of investigating whether tectonic signals can be detected. In 2002-2003, automated quality control software was implemented to monitor the electromagnetic data.

Data from these and other regional networks are archived and distributed at the Northern California Earthquake Data Center (NCEDC), operated at the BSL in collaboration with USGS/Menlo Park. The data reside on a mass-storage device (current holdings ~ 30 TerraBytes), and are accessible “on-line” over the Internet (<http://www.ncedc.org>). Among others, data from the USGS Northern California Seismic Network (NCSN), are archived and distributed through the NCEDC. The NCEDC also compiles, maintains, archives and distributes the ANSS earthquake catalog. Core University funding to our ORU currently provides salary support for 2 field engineers, one computer expert, 2 data analysts, 1 staff scientist and 2 administrative staff. This supports a diminishing portion of the operations of the BDSN and provides seed funding for our other activities. All other infrastructure programs are supported through extra-mural grants primarily from the USGS, NSF, and the State of California, through its Office of Emergency Services (OES). We acknowledge valuable recent contributions from other sources such as Caltrans and PEER, as well as our Earthquake Research Affiliates.

3. Highlights of 2007-2008

3.1 Research Accomplishments

Chapter 2 documents the main research contributions of the past year. Research at the BSL spans a broad range of topics, from the study of microseismicity at the local scale to global deep earth structure, and includes the use of seismological, geodetic, and remote sensing (InSAR) techniques. Productivity continues to be high: over forty papers in refereed journals have been authored or co-authored by BSL researchers in the last year, a steady number compared to previous years.

Once again, the data provided by the borehole stations of the HRSN (Parkfield) network have led to important and exciting results. Following the discovery two years ago of non-volcanic tremors in the Parkfield area, a highlight of this past year's research is the use of a noise correlation approach to document seismic velocity changes correlated with fault zone deformation as measured by GPS, as well as with tremor activity, following the M6.5 San Simeon and M6.0 Parkfield earthquakes (Research Study 32.). This study is a powerful illustration of the successful continuing collaboration between BSL and IPG (Institut de Physique du Globe de Paris) researchers. The collaboration started with a workshop in Paris in January 2007 and is supported on the French side by funding from CNRS through a PICS (Projet international de Coopération Scientifique) and, on the Berkeley side, through a combination of BSL core funds and two France Berkeley Fund awards. A second workshop was held at BSL in December 2007, and a third one is being planned for January 2009 in Paris.

Monitoring of tremor activity at Parkfield continues with new intriguing observations, such as the occurrence of quasi-periodic bursts of tremor activity (Research Study 21.), or the identification of several classes of tremors with different locations (Research Study 28.). On the other hand, acceleration of the recurrence of repeating microseisms since the early 1990's has been confirmed (Research Study 25.).

BSL researchers made important contributions to the analysis of the data in the wake of the tragic 08/06/07 Crandall Canyon mine collapse. Through the use of seismic broadband waveform inversion tools developed at BSL, Sean Ford and Doug Dreger, with LLNL collaborator Bill Walter, demonstrated that the recorded seismic signals could not be due to a tectonic earthquake, but rather the collapse itself (Research Study 30.).

The occurrence of the 10/30/07 M_w 5.4 Alum Rock earthquake, widely felt in the San Francisco Bay Area, provided an opportunity to demonstrate the capabilities of both the Northern California real time systems (Research Study 22.) and the ElarmS earthquake Early Warning methodology (Research Study 26.). It also highlighted the possibility of slip transfer between the Hay-

ward and Calaveras faults (Research Study 3.).

The comparison of low frequency noise at the ocean floor broadband station MOBB and the island station FARB has provided important constraints on the generation of this noise and its relation to infragravity waves in the ocean (Research Study 14.).

BSL researchers continue to investigate the recently widely advertised Accelerated Moment Release hypothesis (AMR) and have documented the high sensitivity of "observed" AMR to the choice of free parameters considered (Research Study 4.).

On the global seismology front, a new method has been developed to separate the effects of depth dependence and intrinsic frequency dependence on seismic attenuation as measured using free oscillations (Research Study 20.) and progress is being made in the construction of tomographic models at global and regional scales, using 3D numerical wave propagation computations (Research Studies 12. and 17.).

Finally, the development of new electronics for the STS-1 seismometer has been completed. BSL researchers and engineers have been involved in the testing and evaluation of these successful new electronics (Chapter 3, Section 9.) and in particular, have already utilized their convenient remote calibration capabilities at several BDSN stations.

3.2 Infrastructure and Earthquake Notification

As in previous years, BSL's infrastructure development efforts have centered around several major projects:

- operation and enhancement of the joint earthquake notification system with USGS/Menlo Park.
- the continuing development of the California Integrated Seismic Network
- participation, at various levels, in two components of the national Earthscope program: archival of borehole strainmeter data in the framework of the Plate Boundary Observatory (PBO), and the preparation for archival of the data from the San Andreas Fault Observatory at Depth (SAFOD). The USArray Transportable Array has now moved out of California.
- development of borehole networks at Parkfield and along the Hayward Fault
- operation and further enhancements of the BARD network of continuous GPS
- operation of the Northern California Earthquake Data Center

The main goal of the CISN (see Chapter 3, Section 2.) is to ensure a uniform system for earthquake monitoring and reporting in California. The highest priority, from the point of view of emergency responders in California, is to improve the robustness of statewide real-time notification and to achieve a uniform interface across the State to the California OES and other emergency responders. This represents a major challenge, as the CISN started as a heterogeneous collection of networks with disparate instrumentation, software systems, and cultures. Over the past few years, much effort has gone into developing coordinated software between Southern and Northern California and, in Northern California, between Berkeley and USGS/Menlo Park. These two institutions are joined together in the Northern California Earthquake Management Center (NCEMC). A highlight of the past year has been the re-installation of five sites (SUTB, RAMR, HATC, HAST, HELL) previously occupied by USArray Travelling Array, with permanent broadband equipment acquired through FEMA grants and OES funds. In particular, BSL engineers improved the installation design to remove condensation inside the vaults, an important issue for long term deployments. One other site is awaiting transfer of permit to BSL, while two additional former USArray sites are awaiting funding to acquire permanent seismic equipment.

2007-2008 is the last year of the 3 year funding cycle for CISN from the Office of Emergency Services (OES). In the past year, progress has been made on unifying the way leap seconds are treated in Southern and Northern California, and on magnitude calibration across the state. The *Jiggle* analysis software has been modified and installed in Northern California in November 2006 and will be offered to other regions of the Advanced National Seismic System soon. Data from the Northern Hayward Fault Network have been integrated into the Northern California Seismic System.

BSL staff continue to spend considerable efforts in organizational activities for CISN, notably by participating in the CISN Project Management Group (Neuhauser and Hellweg), which includes weekly 2 hour phone conferences, and the Standards Committee (Neuhauser-chair, Hellweg, Lombard), which strives to define and coordinate software development tasks. Romanowicz and Hellweg serve on the CISN Steering Committee. The CISN also represents California as a designated region of ANSS (Advanced National Seismic System) and the BSL is actively involved in planning activities for the ANSS.

The Parkfield borehole network (HRSN, see Chapter 3, Section 4.) continues to play a key role in support of the Earthscope SAFOD (San Andreas Fault Observatory at Depth) drilling project, by providing low noise waveforms for events in the vicinity of the target drilling zone. Efforts have been started this year to minimize the costs of this network, in particular the land fees, by moving

key elements of the telemetry away from a very costly site.

The BARD continuous GPS (C-GPS) network (see Chapter 3, Section 5.) has focused its efforts on the development of local collaborations to densify the network and reduce telemetry costs associated with the installation of new stations. Also, BSL engineers have been working on the design of meteorological sensors to be installed at GPS sites. Corrections using data from these sensors will help minimize the effects of the troposphere on BARD solutions.

Finally, the NCEDC has continued to expand its data holdings and enhance access to the data; in particular, we have made progress in archiving continuous seismograms read from NCSN tapes, to satisfy numerous requests from researchers interested in looking for non-volcanic tremors in the background noise, as well as for the study of teleseisms, and have ported the entire NSCN earthquake catalog into the CISN database schema.

4. BSL staff news

Changes in BSL staff in 2007-2008 are as follows.

The following graduate students associated with BSL completed their PhD's in the past year: Mei Xue, now a faculty member at Tongji University in Shanghai, and Karl Kappler, who is still around. Eileen Evans obtained her MS in May 2008 and worked through the summer before starting a PhD at Harvard this fall.

In the global seismology group, Aimin Cao, graduate student and later post-doc left for Rice University, and Fabio Cammarano left for ETH (Zurich). There have been several new arrivals: Laurent Stehly joined the global seismology group as a post-doc in January, and Paul Cupillard in June. Laurent obtained his PhD at the Universite Joseph Fourier in Grenoble, and Paul, at IPG in Paris. They bring expertise on the use of noise cross-correlations for structure studies, and on the Spectral Element Method, respectively. Zhao Zheng (Allen), from Peking University and Sanne Cottaar, from Utrecht University, have joined the group as graduate students.

Bob Uhrhammer, who started working at the Berkeley Seismographic Stations in 1975, retired in January 2008, and has come back to work part time as a retiree appointee. His help in training Taka'aki Taira, our new staff seismologist who arrived in August, is invaluable. Dr. Taira obtained his PhD at Hokkaido University in Japan, followed by post-docs at Carnegie and the Univ. of Utah. His research interests include earthquake nucleation and rupture processes, as well as fault rheology and time dependent phenomena in fault zones.

BSL hosted the following visiting scientists in 07-08: Jean Pierre Vilotte (IPG Paris), Georges Poupinet (Grenoble, France), Hui-Hsuan (Kate) Chen (National Taiwan Normal University, Taiwan), DV Chandrasekhar

(National Geophysical Research Institute, Hyderabad India), Luca Malagnini (Istituto Nazionale di Geofisica e Vulcanologia, Italy), Paramesh Banerjee (Newcastle University, England), Fabian Walter (ETH Zurich), Shweta Sangewar (Indian Institute of Technology, India), Andrea Cannata (University of Catania, Italy), Stefano Gresta (University of Catania, Italy), and the following summer 07 interns: Jake Lippman, from UC Davis, and Andrew Tran, from Cal Poly.

Alexey Kireev left BSL in early April. Oleg Khainovski, a 2006 UCB engineering Physics graduate, was hired in August as a programmer to work on the CISON and Early Warning projects. Angela Chung left the BSL in June to pursue a PhD in geophysics at Stanford University.

5. Acknowledgements

I wish to thank our technical and administrative staff, scientists and students for their efforts throughout the year and their contributions to this Annual Report. Individual contributions to activities and report preparation are mentioned in the corresponding sections, except for the Appendix section, prepared by Kate Lewis (Conner), Kristen Jensen and Jennifer Taggart.

I also wish to specially thank the individuals who have regularly contributed to the smooth operation of the BSL facilities: Mario Aranha, Rich Clymer, Angela Chung, Doug Dreger, John Friday, Jarrett Gardner, Peggy Hellweg, Nicolas Houlié, Bill Karavas, Alexei Kireev, Rick Lellinger, Pete Lombard, Kevin Mayeda, Rick McKenzie, Bob Nadeau, Doug Neuhauser, Charley Paffenbarger, Jennifer Taggart, Bob Uhrhammer, and Stephane Zuzlewski, and in the administrative office, Kristen Jensen, Kate Lewis (Conner), Tina Barber-Riggins, and Yolanda Andrade. I also wish to thank our undergraduate assistants, Eileen Evans, Sarah Minson, Eric Winchell, and Jozef Matlak for their contributions to our research and operations activities.

I am particularly thankful to Jennifer Taggart and Peggy Hellweg, for their help in putting together this Annual Report.

The Annual Report of the Berkeley Seismological Laboratory is available on the WWW at http://seismo.berkeley.edu/annual_report.

Barbara Romanowicz
September 30, 2008

Chapter 2

Research Studies

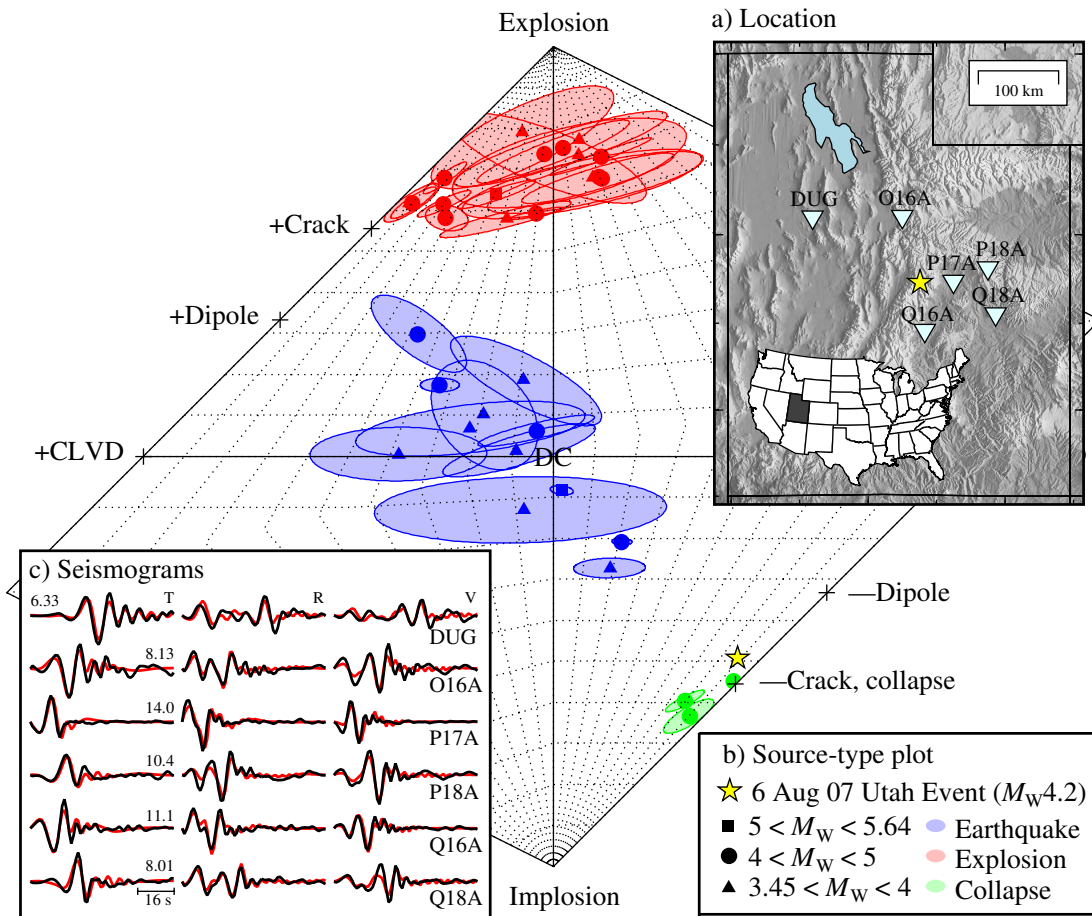


Figure 2.1: a) Locations of the August 6, 2007 event and 6 of the closest USArray and ANSS stations. b) Source type plot from the method of *Hudson et al* (1989) shows clear separation of populations of earthquakes, explosions and collapses. The yellow star shows the solution for the August 6, 2007 seismic event. c) Observed seismograms (black) are compared to synthetics (red) for the non-double-couple solution, which is dominated by a horizontal closing crack (b). The maximum displacement (10^{-7} m) of each set of tangential (T), radial (R), and vertical (V) observations is given. (Figure from Section 30.)

1. Stress preconditioning and magma chamber pressure evolution at Piton de la Fournaise

Nicolas Houlié, J.C. Komorowski, and J. Dufek

1.1 Introduction

The pressure in upper crustal magma reservoirs is a key parameter for understanding pre-eruptive surface deformation and the governing processes leading to an eruptive crisis. Although much progress has been made in documenting pre-eruptive measurements, it remains difficult to incorporate measurements that span the full range of temporal scales of deformation (from seconds to years) using existing geophysical networks.

Instrumental limitations constitute a significant difficulty in the study of processes occurring over large frequency domains. Each geophysical measurement has its own sensitivity and thus is able to describe aspects of particular source mechanisms (Figure 2.2a). For instance, short period seismic monitoring is able to track magma motion (typically 1Hz range) during seismic crises. However, the use of microseismic observations is limited during quiescence of volcanic activity. Broadband seismometers ($Period < 60\text{s}$) have been successfully used to constrain magma flow in secondary conduits, dyke vibration and dyke propagation (Chouet, 1996). Deformation survey networks (GPS, InSAR, extensometers, and tiltmeters) typically describe inter-crisis periods and highlight that the volcanic edifice is active between main flank eruptive events when the seismicity level is low. Deformation monitoring is thus complementary to seismic instrumentation. Despite the use of all techniques available from GPS to short-period seismometers, the period domain from 100 to 1000 seconds remains unfortunately inaccessible to all but very broadband seismometers (corner period > 200 seconds). These instruments require high quality installations that are complex to complete in volcanic areas. Also, the integration of velocity into displacement time-series remains challenging, and distinguishing tilt from horizontal motion (Wielandt *et al.*, 1999) is not always possible. As a consequence, theoretical numerical models that simulate continuous magmatic injection cannot be fully tested. This limits the reliability of the prediction (both time and location) of eruptive events and explains why our understanding of processes is typically restricted to pressure drops assuming single geometries (location and shape) for the source.

The creation of a physical model of a whole edifice will not be achieved until the unaccounted magma volumes injected in the volcano can be quantified properly. Most techniques (deformation, CO_2/SO_2 concentration drops, etc.) evaluate the change in pressure and not the pressure relative to lithostatic pressure. We estimate the

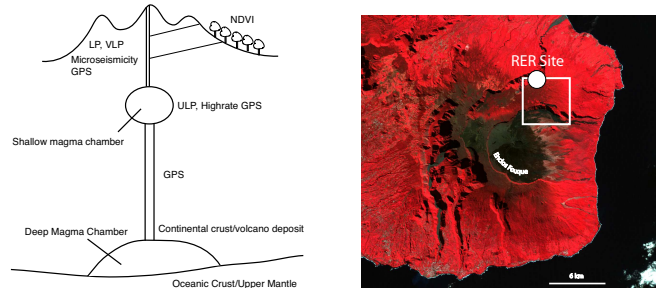


Figure 2.2: a) General sketch of the Piton de la Fournaise. Already successfully applied techniques are indicated on the sketch. b) Near infrared composite (432) of the Piton de la Fournaise volcano. Vegetated areas are red. The NDVI methodology cannot be applied on the upper part of the volcano, as there is a lack of vegetation. BAND 4 (Near infra-red, $760 - 900\text{nm}$) is the color red, BAND 3 (Visible red, $630 - 690\text{nm}$) is the color green, BAND 2 (Visible Green, $520 - 600\text{nm}$) is the color blue.

absolute pressure in the magma chamber as a reference pressure for the whole edifice. In order to achieve this goal, we need to estimate the volumes intruded into or extruded from the magma chamber. We propose to address both instrumental and theoretical limitations by defining a geophysical model centered on the upper magma reservoir.

Here, we integrate seismic data, supported by geodetic observations, in a multi-scale model of the pressure in the magma chamber over the last two decades for the Piton de la Fournaise. We set up a physical model able to integrate various techniques which is consistent with the wide range of length and time scales of signals recorded on the field. As an example, we present an application (included in this framework) made at different time and space scales for different magmatic sources with different characteristic periods.

We reconstruct the pressure-history at Piton de la Fournaise (PdF) over the past two decades based on a collection of pressure drops to describe upper-crustal magma injection processes in relation to eruptive events. The choice of PdF as a study case is four-fold: First, this volcano is one of the few volcanic edifices with a very-broadband seismometer located within 10 km of the summit. Second, PdF volcano is minimally affected by tectonic stress or continental deformation. The maximal extension across the magmatic edifice was estimated at 3mm/yr (Houlié, 2005). The upper magma chamber lo-

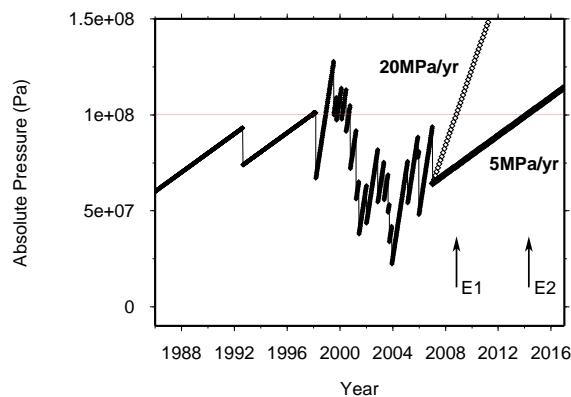


Figure 2.3: When will the next flank eruption occur at Piton de la Fournaise? Projection of the Pressure during the next decade ($I2/I1 = 8$). Assuming the pressurization rate would decrease to 20MPa/yr (period 1998-2000) or possibly to 5MPa/yr (back to the pre-1998 injection rate), the next eruptive flank event would occur between 2009 (E1) and 2012 (E2).

cated at sea-level is thus not affected by a large flank deformation of the volcano. Third, it has been one of the most active volcanoes during the last decade, with more than fifteen eruptions since 1998. And lastly, this volcano is vegetated enough (Figure 2.2b) to test the Normalized Difference Vegetation Index (NDVI) (Richardson, 1977) following guidelines defined previously (Houlié *et al.*, 2006).

1.2 Discussion

By proposing to model each event in the framework of the absolute pressure in the magma chamber, we hope to integrate models/datasets from various origins in order to set up a physical model of the volcano. The estimates provided in this work can be scaled according to any new available dataset (tiltmeters, degassing monitoring, etc.).

As a first step, we show that the injection rate in the upper magma chamber increased by at least a factor of 8 in two years (1999-2001), following the 1998 flank eruption. This result demonstrates the ability of the absolute pressure parameter to describe eruptive activity over decades using simple geometry reservoirs.

Additionally, computed amplitudes of the 2-year periodic magma bursts are consistent with previous long-term intrusion estimates and justify our choice of pressure of the magma chamber. The observed periodicity suggests an interaction between magma reservoirs and the changing stress state of the crust. This interaction was previously suggested (Aki and Ferrazzini, 2001). Representation of the volcano edifice mainly generated by monitoring habits that emphasize isolated events may be at odds with the physical model presented here.

The increased activity since 1998 may be preparing the

next flank event along the fractures left open by the 1998 dyke injections. According to NDVI results, we encourage the community to also monitor the fractures formed by the 1998 eruption that have not emitted any magma yet.

References

- Aki, K., and V. Ferrazzini (2001), Comparison of Mount Etna, Kilauea, and Piton de la Fournaise by a quantitative modeling of their eruption histories, *J. Geophys. Res.*, *106*(B3), 4091–4102.
- Chouet, B. (1996), Long-period volcano seismicity: its source and use in eruption forecasting, *Nature*, *380*, 309–316.
- Houlié, N. (2005), Mesure et Modélisation de données GPS de volcans. Applications à des études de déformation à diverses échelles et à la tomographie des panaches atmosphériques., Ph.D. thesis, Institut de Physique du Globe de Paris.
- Houlié, N., J.-C. Komorowski, M. de Michele, M. Kasereka, and H. Ciraba (2006b), Early detection of eruptive dykes revealed by Normalized Difference Vegetation Index (NDVI) on high-resolution satellite imagery., *Earth & Planet. Sc. Lett.*, *246*(3-4), 231–240, doi:10.1016/j.epsl.2006.03.039.
- Richardson, A. J., and C. Wiegand (1977), Distinguishing vegetation from soil background information, *Photogramm. Eng. Remote Sens.*, *43*, 1541–1552.
- Wielandt, E., and T. Forbriger (1999), Near-field seismic displacement and tilt associated with the explosive activity of stromboli, *Ann. Geofis.*, *42*(3), 407–416.

2. Rigid Block Motion, Interseismic Strain, and Backarc Deformation in the Aegean

Edwin (Trey) Apel, Roland Bürgmann, and Enrico Serpelloni (INGV - Bologna, Italy)

2.1 Introduction

We combine available GPS data in and around the Aegean region to model plate boundary deformation and earthquake cycle effects in the observed velocity field. Typically, GPS data in the region have been used as evidence that a southern Aegean block behaves coherently and rigidly (e.g. *Nyst and Thatcher, 2004; Reilinger et al., 2006*). These first-order models match the observed data quite well, suggesting little intra-plate or plate-boundary deformation. There has been little suggestion that the GPS data record anything other than rigid plate motion. However, the $M_w \sim 8.4$ (*Shaw et al., 2008*) Crete earthquake of AD 365 (Figure 2.4) and some other historic earthquakes likely occurred along the Hellenic subduction zone (*Burton et al., 2004*), which implies that a substantial portion of the subduction thrust may be locked. Depending on the locking required to generate earthquakes of this magnitude, a measureable elastic strain signal reaching far into the overriding plate should be evident in the surface velocity field. Alternatively, slow accumulation of elastic strain and dominantly aseismic creep on the subduction thrust may generate a signal different from the pattern commonly observed along subduction zones. It is also possible that the surface velocities generated by convergence at a locked subduction zone are masked by simultaneous back-arc extension, creating the illusion of rigid block motion. We consider multiple possibilities in an attempt to interpret the current geodetic signal in the region and its implications for earthquake hazard assessment. We use a block modeling approach that considers both rigid rotations of plates and elastic strain fields along plate boundary faults to examine the possible trade-off between these components. As many of the observations are located away from the plate boundaries in question, it is difficult to constrain boundary parameters, such as locking depth and dip, using only the GPS data. We generate multiple models to explore the solution space of all reasonable parameters. Our modeling suggests that it is possible for coeval extension and convergence to occur at opposite ends of a plate masquerading as rigid block motion. Eventually, precisely determined vertical motions of GPS stations above the Hellenic subduction zone are needed to resolve this important question.

2.2 GPS Velocities

Our primary data in this study is a solution of 166 stations, concentrated primarily in Western Europe, pro-

cessed by Enrico Serpelloni. Processing details can be found in (*Serpelloni et al., 2007*). Selected, globally distributed IGS sites were used to define an ITRF00 reference frame.

In addition to our own analysis, we integrate GPS-station velocities from published work in Africa, Central Greece, and Turkey. We integrate these published solutions (*Stamps et al., 2008; Reilinger et al., 2006; Hollenstein et al., 2008; Clarke et al., 1998*) with our own solution. These velocities were combined with our solutions by rotating them into a common reference frame. We combine velocities published in an ITRF00 reference frame into our own solution by minimizing the misfit at co-located stations. After the combination, we compare our combined solution the published values to estimate misfit. For most sites the RMS is $\sim 1-2$ mm/yr, well within the 95% confidence intervals for these sites.

2.3 Plates and Blocks

Plate boundary locations are critical for characterizing GPS velocities and the plate kinematics of a particular region. While some plate boundaries in the Aegean region are well defined by active fault traces, youthful geomorphology, and abundant local seismicity, others appear more diffuse and ambiguous. We draw on the distribution and kinematics of 20th century seismicity, local geology, and mapped faults, and the GPS velocity itself to define our block model boundaries. Within this paper the term plate (and microplate) refers to the rigid, coherent, lithospheric entity defined by faults, seismicity etc. The term block is the specific implementation of these data into a parameterized set of variables within our block model (e.g. *Apel et al., 2006*).

We define our blocks as rigid entities on a spherical earth bounded by dislocations in an elastic halfspace and invert for poles and rates of rotation that minimize the misfit to the GPS velocities using the block modeling code by *Meade and Hager (2005)*. Because our inversion combines rigid block rotation with elastic strain accumulation effects, the parameterization of the block boundary geometry is critical. Geometry of the block boundaries is based heavily on seismicity and adopted from prior analyses (*Nyst and Thatcher 2004; Reilinger et al., 2006*) or adjusted as indicated by the geodetic data.

2.4 Results

Some block motions are well defined and vary little within our model. The Eurasian block and Nubian block

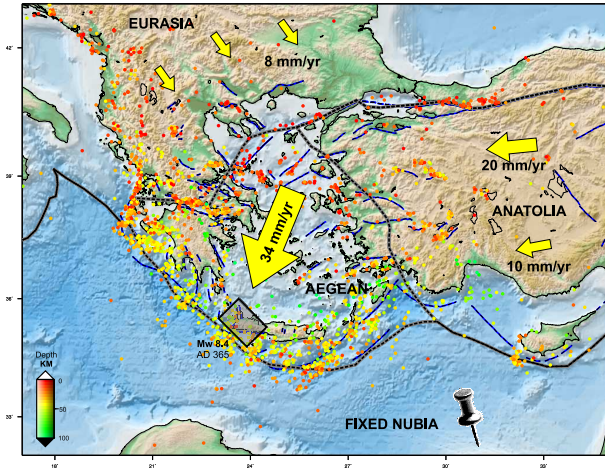


Figure 2.4: Seismicity of the Aegean region for depths less than 100km. Arrows show relative block motions in a fixed Nubian reference frame.

rotation parameters are defined primarily by the sites that lie within the stable interior and are affected very little by plate boundary strain. The inferred motion of smaller blocks (Aegean and Anatolian) can change based on the parameterization of the boundaries of these blocks. The stability of the major blocks provides robust constraints on far-field motions and allows us to test variable segment geometries along those boundaries used to develop our preferred model.

Figure 2.5 shows observed and predicted velocities through a model of simultaneous extension and contraction within the Aegean block. We model the subduction zone with variable locking dips which generate a series of non-unique fits to our data. It remains unclear whether or not the rigid block model with no elastic boundaries actually fits the horizontal GPS data better than models that include elastic block boundaries. At present, our models suggest that it is possible to accumulate some amount of elastic strain along the subduction zone. Our continuing research includes incorporating vertical uplift rates in models to fully capture and constrain any amount of elastic strain that is accumulating along the Hellenic subduction zone.

2.5 References

Apel, E. V., R. Bürgmann, G. Steblov, N. Vasilenko, R. King, and A. Prytkov, Independent active microplate tectonics of northeast Asia from GPS velocities and block modeling, *Geophysical Research Letters*, 33, L11303, doi:10.1029/2006GL026077, 2006.

Burton, P., X. Yebang, C. Qin, G. Tselentis, and E. Sokos, A catalogue of seismicity in Greece and the adjacent areas for the twentieth century, *Tectonophysics*, Vol 390, pg. 117127, 2004.

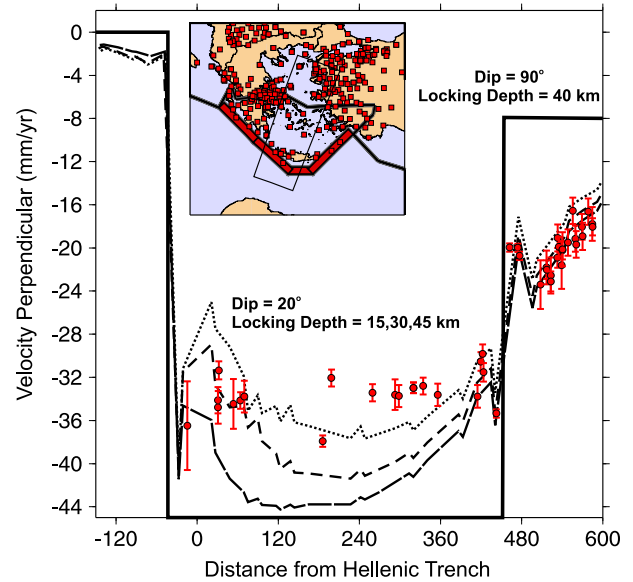


Figure 2.5: Velocity profile of measured (circles) and predicted velocities (dashed lines) through the Aegean region. The inset figure shows the block configuration used in the inversion.

Clarke, P. et al., Crustal strain in central Greece from repeated GPS measurements in the interval 1989-1997, *Geophysical Journal International*, Vol 135, pg. 195-214, 1998.

Hollenstein, Ch., M. Müller, A. Geiger, and H.-G. Kahle, Crustal motion and deformation in Greece from a decade of GPS measurements, 1993-2003, *Tectonophysics*, Vol 449, pg. 1740, 2008.

Meade, B. J., and B. H. Hager, Block models of crustal motion in southern California constrained by GPS measurements, *Journal of Geophysical Research*, 110, B03403, 10.1029/2004JB003209, 2005.

Nyst, M., and W. Thatcher, New constraints on the active tectonic deformation of the Aegean, *Journal of Geophysical Research*, 109, B11406, doi:10.1029/2003JB002830, 2004.

Reilinger R., et al., GPS constraints on continental deformation in the Africa-Arabia-Eurasia continental collision zone and implications for the dynamics of plate interactions, *Journal of Geophysical Research*, 111, B05411, doi:10.1029/2005JB004051, 2006.

Shaw B., et al., Eastern Mediterranean tectonics and tsunami hazard inferred from the AD 365 earthquake, *Nature - Geoscience*, Vol 1, doi:10.1038/ngeo151, 2008.

Stamps, S., E. Calais, E. Saria, C. Hartnady, J.-M. Nocquet, C. Ebinger, and R. Fernandes, A kinematic model for the East African Rift, *Geophysical Research Letters*, 35, L05304, doi:10.1029/2007GL032781, 2008.

3. Linking faults: Subsurface creep directly connecting the Hayward and Calaveras faults

Eileen Evans and Roland Bürgmann

3.1 Introduction

Identifying and understanding the geometry of the Hayward and neighboring faults is crucial for determining the earthquake hazard of the San Francisco Bay Area. Although creeping along most of its surface trace, the Hayward fault can and does produce major earthquakes; the last rupture occurred in 1868. Slip on the Calaveras and Hayward faults may be transferred directly between the two faults through a contiguous stepover, requiring reassessment of potential earthquake scenarios on both faults. Seismicity on the fault shows that the near-vertical Hayward Fault dips to the east towards the southern end of its trace (Waldhauser and Ellsworth, 2002). Characteristic repeating earthquakes through the stepover provide an estimate of subsurface creep through the juncture. Incorporating InSAR and updated GPS campaign data into an elastic dislocation model of the East Bay, we evaluated the validity of the seismically proposed geometry and explored the kinematics of a contiguous structure linking the Hayward and Calaveras faults.

3.2 Seismic Stepover

A seismic trend east of the southernmost trace illuminates a possible contiguous structure linking the Hayward Fault with the Calaveras Fault to the east (Manaker et al., 2005). Accurate hypocenter locations in the seismic trend between the Hayward and Calaveras faults begin to reveal the structure of this stepover region. A tomographically derived velocity structure of the eastern Bay Area, combined with hypo-dd relocations of clustered events, made better absolute relocations of microseismicity possible (Hardebeck et al., 2007). We used these relocations to define the geometry of fault planes in our dislocation model. The relative relocations of the hypo-dd method, (Waldhauser and Ellsworth, 2002) sharpen fault structures and clearly show the eastward dip of the Hayward fault (Figure 2.6). Additionally, characteristic repeating earthquakes (Nadeau et al., 1994) exist through the stepover (Figure 2.6), identifying a relatively narrow band of seismicity within the background seismicity. We consider these repeaters as a proxy for creep, confirming aseismic slip through the stepover.

3.3 Modeling GPS and InSAR data

GPS campaigns, conducted over the last year in the Grant network in Halls Valley and the Calaveras network surrounding the Calaveras reservoir, give updated

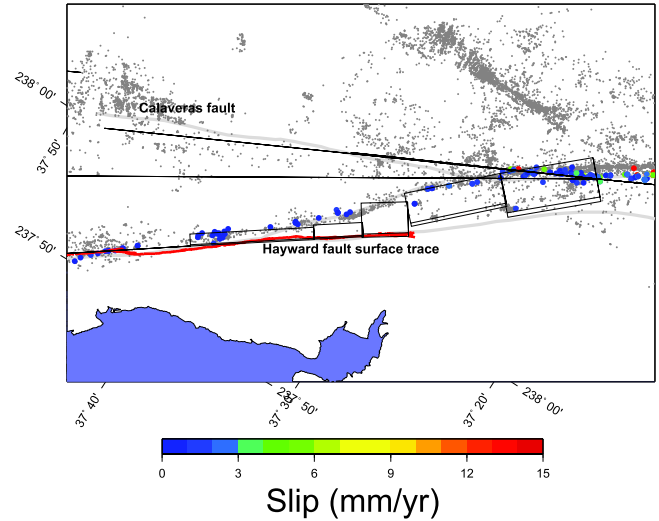


Figure 2.6: The Mission trend between the Hayward and Calaveras faults is well defined in the background seismicity. Characteristic repeating earthquakes are superimposed on seismicity and color coded by slip rate. Rectangles are the surface projections of model faults.

surface velocities for the region, demonstrating deformation consistent with a dipping Hayward Fault. In our slip inversion, we also include GPS data from the Bay Area's permanent network and PS-InSAR (Permanent scatter-interferometric synthetic aperture) data. We use an elastic dislocation model (Okada, 1985) of Bay Area faults (Bürgmann et al., 2006), incorporating several shallow rectangular dislocations to model the stepover (constructed to be as contiguous as rectangles will allow)(Figure 2.6). We then perform a joint inversion to solve for slip on these dislocations, finding high slip rates near Fremont and towards the Calaveras. Slip inversions on the step-over structure were robust between InSAR and GPS. In the final inversion, the InSAR data are weighted at 20%. Modeled surface velocities (in gray) and observed velocities (black) are shown in Figure 2.7. As the stepover patches dive underground, modeled slip increases towards the Calaveras fault, which is consistent with creep rates on that section on the Calaveras (Manaker et al., 2003) and with the slip estimates from the repeaters (Nadeau, 1994). Indeed, the existence of characteristic repeating earthquakes through the stepover indicates that creep actively contributes to the direct transfer of slip from the central Calaveras fault to the southern Hayward fault.

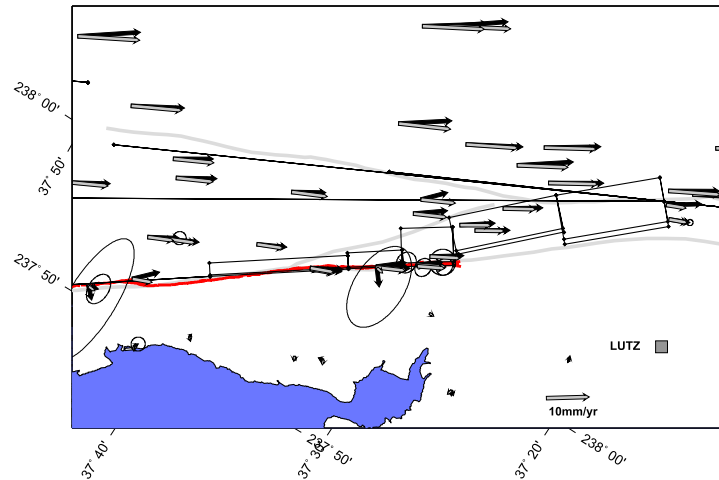


Figure 2.7: Modeled velocities based on our slip inversion are shown in gray. Observed velocities are black. All velocity vectors are shown in reference to station LUTZ

3.4 Alum Rock Earthquake

On October 30, at 8:04 local time, a M_w 5.4 earthquake nucleated just south of the Calaveras Reservoir. The epicenter was located on the central Calaveras fault between the Calaveras network to the north and the Grant network to the south. Aftershocks to the south extended into the Grant network, which had been surveyed only two weeks before. Following the earthquake, we set up GPS receivers in the Grant network. Additionally, several nearby continuous GPS sites observed this earthquake. Coseismic offsets following the Alum Rock earthquake are consistent with right lateral slip. Offsets in the Grant network indicate compression across the fault, although the measurements have large error. Aftershocks continued for several days, and the signal continued to develop for months following the earthquake. Unfortunately, the postseismic signal is too small relative to noise to quantify postseismic deformation.

3.5 Conclusions

The Hayward Fault dips into and merges with the Calaveras Fault at depth, affecting hazard scenarios on both faults. This contiguous step-over appears to directly transfer slip between the two faults. Characteristic repeating earthquakes outline this geometry and confirm subsurface creep through the juncture. GPS velocities and PS-InSAR range change rates verify this geometry and constrain slip rates. Additionally, the 2007 Alum Rock earthquake demonstrated that this region is seismogenic. This implies that a large earthquake on the Hayward or Calaveras fault may transfer slip through the step-over, in previously unanticipated rupture scenario.

3.6 Acknowledgements

Special thanks to Isabelle Ryder, Romain Jolivet, David Shelly, and Rob Porritt for their invaluable field assistance. This project was made possible by NSF grant EAR-0337308.

3.7 References

- Bürgmann, R., G. Hiley, A. Ferretti and F. Novali, Resolving vertical tectonics in the San Francisco Bay Area from permanent scatterer InSAR and GPS analysis, *Geology*, 34 no. 3; p. 221-224, 2006.
- d'Alessio, M.A., I.A. Johanson, R. Bürgmann, D.A. Schmidt, M.H. Murray, Slicing up the San Francisco Bay Area: Block kinematics and fault slip rates from GPS-derived surface velocities, *J. Geophys. Res.*, 110, 2005.
- Hardebeck, J. L., A.J. Michael, and T.M. Brocher, Seismic Velocity Structure and Seismotectonics of the Eastern San Francisco Bay Region, California, *Bull. Seism. Soc. Am.*, 97, 826-842, 2007
- Manaker, D.M. A.J. Michael, and R. Bürgmann, Subsurface Structure and Kinematics of the Calaveras-Hayward Fault Stepover from Three-Dimensional V_p and Seismicity, San Francisco Bay Region, California, *Bull. Seism. Soc. Am.*, 95, 446-470
- Manaker, D.M., R. Bürgmann, W.H. Prescott, and J. Langbein, Distribution of interseismic slip rates and the potential for significant earthquakes on the Calaveras fault, central California, *J. Geophys. Res.*, 108, 2287, 2003.
- Okada, Y., Surface Deformation due to shear and tensile faults in a half-space, *Bull. Seism. Soc. Am.*, 75, 1135-1154, 1985
- Waldhauser, F., W.L. Ellsworth, Fault structure and mechanics of the Hayward Fault, California, from double-difference earthquake locations, *J. Geophys. Res.*, 107, B32054, 2002

4. No Apparent Accelerating Moment Release in Areas of High Stress

Aurélie Guilhem and Roland Bürgmann

4.1 Introduction

The search for spatio-temporal interactions between earthquakes is fundamental in order to understand the stress evolution in the lithosphere as well as the earthquake mechanism. Many studies have been conducted to analyze the evolution of seismicity in relation to the stress field, with the idea that continuous plate motion needs to be accommodated on faults by the occurrence of earthquakes releasing the accumulated stress. This earthquake cycle theory, first developed by Reid in 1910, introduced the relation between elastic stress accumulated along the fault zone and occurrence of earthquakes. The Accelerating Moment Release (AMR) idea was developed by *Bowman et al.* (1998) and is based on the hypothesis that prior to a large earthquake the stress field in the vicinity of the next rupture increases in such a way that one can observe an acceleration of the background seismicity following a power-law function. The change in the seismicity rate produces a regional increase in the cumulative Benioff strain, which is a measure of the cumulative seismic energy of the seismic events considered prior to a mainshock. To quantify the AMR, one examines the ratio, called *c*-value, between the root-mean-square of a power-law time-to-failure function versus a linear fit to the cumulative energy of the events. A strong case for AMR would be for *c* less than 0.5. Previous works (*Guilhem et al.*, 2007; *Hardebeck et al.*, 2008) showed that AMR, observed for all M6.5+ earthquakes in Southern California of recent times (*Bowman et al.*, 1998; *Bowman and King*, 2001), is very sensitive to three free parameters: magnitude range of the pre-seismicity, area surrounding the events (considering a circular search) and the time period prior to a large earthquake. Because of the large dependence on the choice of the free parameters, doubts about the validity of the analysis have emerged (*Hardebeck et al.*, 2008).

4.2 AMR search in Parkfield region

Mignan et al. (2007) suggested that if AMR exists, one should in theory observe it over an entire earthquake cycle. The Parkfield region is an excellent example for studying AMR where M6.0 earthquakes, since 1857, repeat over a relatively short earthquake cycle (22 years on average). We studied the AMR during the last two earthquake cycles, from 1935 to 1966 and 1967 to 2004, using the ANSS seismicity catalog ($2.0 \leq M \leq 7.0$ in a 5-by-5 degree region centered on the nucleation zone). Computation of the AMR in the area was performed using various magnitude and distance ranges. The lowest

c-values noticed during the first earthquake cycle (about 32 years, from 1934 to 1966) was 0.65 for a search area radius of 85 km, indicating that no AMR was objectively observed during the time period. The second earthquake cycle (1967 to 2004) did not show any case of AMR; the *c*-value is equal to 1 over all radii considered (0 to 200 km) (Figure 2.8). The AMR results appeared to be very sensitive to the occurrences of the 1983 M6.5 Coalinga and 2003 M6.5 San Simeon earthquakes and in particular to their aftershock sequences. Declustering the earthquake catalog to remove most of the aftershocks was performed, but still no change was detected in the AMR.

AMR appears to be biased by the occurrence of large earthquakes during the studied period (Figure 2.8). A large event in the beginning of a chosen observation period tends to dominate the analysis and to increase the *c*-value, compared to a mainshock at the end of the time period that would significantly decrease the *c*-value and support the case for AMR (small *c*-value).

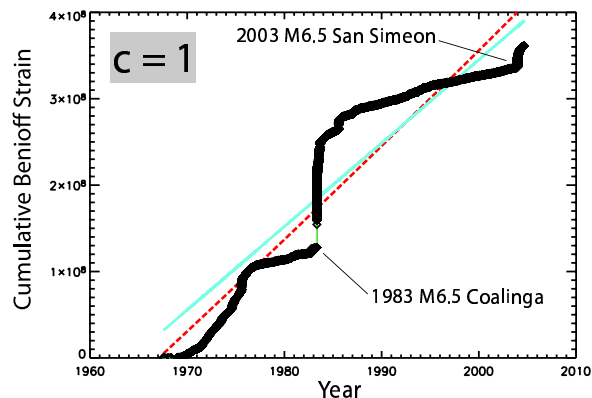


Figure 2.8: AMR in the Parkfield region in a 60-km radius region. The *c*-value for the 1967-2004 period does not show any AMR, with a *c*-value equal to 1. The red dashed line shows the power-law function, and the blue line shows the best-fit linear trend of the cumulative Benioff strain. The occurrences of the 1983 M6.5 Coalinga and 2003 M6.5 San Simeon earthquakes, and their aftershock sequences, dominate the signal.

4.3 AMR and Stress

In order to complete the analysis of AMR in Southern California, we evaluated AMR in apparent high stress regions. Maps of stress changes were computed by An-

Andrew Freed at Purdue University considering the coseismic, postseismic and interseismic stress changes of all M7+ earthquakes in Southern California for the last 200 years (Freed *et al.*, 2007). We tested for AMR in the areas of high stress (Figure 2.9), using the hypothesis that the high stress regions represent the places of eventual future events, compared to the regions of low stress, and where we would expect to detect significant AMR if the AMR idea is correct. We studied the AMR for the two high stress regions presented in Figure 2.9 over various time ranges, starting in 1950 to 2008. The test was performed for an eventual mainshock in the region on June 1st, 2008, about 6 months after the end of the analyzed earthquake catalog. We considered all seismic events occurring in the high stress regions ($\Delta\sigma \geq 10$ bars), excluding events in lower stress areas, and we computed the AMR in such way that we considered the entire high stress regions. No AMR was detected in those two regions (*c*-values remained between 0.8 and 1.0). We performed an AMR search in the area of low stress resulting from the occurrence of the great Fort Tejon earthquake, and we did not find evidence of AMR. No difference is observed in the AMR between high and low stress areas. Also, we performed an AMR study over the entire region, considering all events in regions where the stress exceeds 10 bars as well as all events with no condition on the stress field, and again no significant variation was observed.

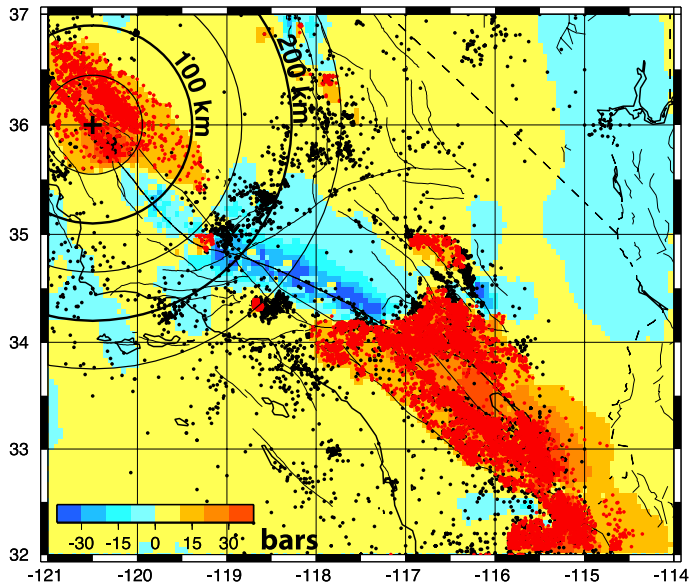


Figure 2.9: AMR study in the northern high stress region. The circles materialize the distance every 50 km from a possible epicenter (black cross). The red dots are the M2.5+ earthquakes located in a high stress region (stress larger than 10 bars), and the black dots show other M2.5+ events in the study region. The background colors show the stress field computed by Andrew Freed for 2005.

4.4 Conclusions

Recent AMR studies (Guilhem *et al.*, 2007; Hardebeck *et al.*, 2008) emphasize the high sensitivity to the choice of free parameters considered in the AMR idea, which becomes a data-fitting exercise with no real power in earthquake forecasting. No evidence of AMR was noticed in the Parkfield region where periodic M6.0 earthquakes occur. AMR, which should be related to high stress regions, is not observed in Southern California, even considering various time, magnitude and distance ranges. Finally we noticed the significant impact of the timing of large events during the pre-mainshock period on the AMR calculations. A large earthquake occurring in the early time period will cancel an eventual AMR case by adding a significant cumulative Benioff strain in a very short time. The contrary is observed when the large shock occurs at the end of the time analysis, forcing to an AMR case.

4.5 References

- Bowman, D.D., G. Ouillon, C.G. Sammis, A. Sornette, and D. Sornette (1998), An observational test of the critical earthquake concept, *Journ. of Geophys. Res.*, *103*, B10, 24,349-24,372.
- Bowman, D.D. , and G.C.P. King (2001), Accelerating seismicity and stress accumulation before large earthquakes, *Geophys. Res. Lett.*, *28*, 4039-4042.
- Freed, A.M., S.T. Ali, and R. Bürgmann (2007), Evolution of stress in Southern California for the past 200 years from coseismic, postseismic and interseismic stress changes, *Geophys. Journ. Intern.*, *169*, doi: 10.1111/j.1365-1246X.2007.03391.x.
- Guilhem, A., R. Bürgmann, A.M. Freed, and T. Ali (2007), Accelerating Moment Release in Areas of High Stress? Preliminary Results, *2006-2007 Berkeley Seismological Laboratory Annual Reports*.
- Hardebeck, J.L., K.R. Felzer, and A.J. Michael (2008), Improved Tests Reveal that the Accelerating Moment Release Hypothesis is Statistically Insignificant, *Journ. of Geophys. Res.*, *in press*.
- Mignan, A., D.D. Bowman, and G.C.P. King (2007), A Mathematical Formulation of Accelerating Moment Release Based on the Stress Accumulation Model, *Journ. of Geophys. Res.*, *111*, B11304.

5. Probing the Rheology of Tibet using Postseismic Motion from Large Earthquakes

Isabelle Ryder and Roland Bürgmann

5.1 Introduction

For the last three decades, a rather vigorous debate has been going on about the most fundamental aspects of the style of continental deformation in the India-Eurasia collision zone. While one school of thought envisions Tibet to be a thickened, weak and fluid-like zone (e.g. *Cook and Royden, 2008*), others consider the tectonics in the region as that of essentially rigid microplates bounded by major lithospheric faults (e.g. *Thatcher, 2007*). Until this issue is resolved, it will be difficult to gain a clear idea of what forces drive the deformation of the upper crust in this region. Large earthquakes initiate rock mechanics experiments of lithospheric dimensions in which a sudden stress change leads to stress relaxation at depth. Surface measurements of the resulting deformation provide a basis for testing structural and rheological models of the lithosphere.

Our main objective in this project is the elucidation of lithospheric rheological structure in northern Tibet, chiefly through InSAR investigation of postseismic motion following three recent major earthquakes. These events are the 1997 M_w 7.6 Manyi earthquake (*Funning et al., 2007; Ryder et al., 2007*), the 2001 M_w 7.9 Kokoxili earthquake (*Lasserre et al., 2005*) and the 2008 M_w 7.2 Yutian earthquake. By analysing the spatio-temporal characteristics of the postseismic signals, and testing the data against various candidate models, we hope to determine whether deformation in the mid to lower crust is localized or distributed, and constrain rheological parameters associated with our preferred model. Our broader objective is to inform the geophysical debate concerning the nature of the Tibetan Plateau: specifically, whether it behaves more like a viscous fluid or a series of rigid blocks.

5.2 InSAR Observations

We use the satellite geodetic technique of Interferometric Synthetic Aperture Radar (InSAR) to observe postseismic deformation for several years following each of the three major earthquakes. For the Manyi case, we use data from the European Space Agency’s (ESA) ERS-2 satellite, and for the Kokoxili case we use radar scenes from ESA’s Envisat. The Yutian earthquake occurred after the launch of Japan’s L-band ALOS satellite, so we will be able to utilize postseismic data from this as well as the C-band Envisat. Postseismic interferograms

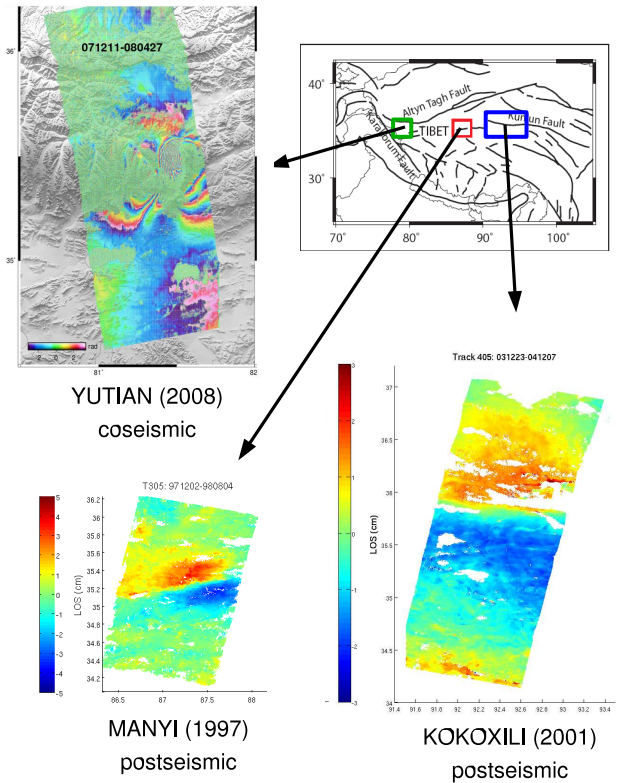


Figure 2.10: Interferograms for the three earthquakes considered in this study. Postseismic interferograms are shown for the 1997 Manyi earthquake and the 2001 Kokoxili earthquake. For the Manyi case, ERS-2 SAR data covering an 8-month time interval are used, and for the Kokoxili case, Envisat data covering a 1-year time interval are used. A coseismic interferogram is shown for the 2008 Yutian earthquake, with each fringe representing about 12 cm of line-of-sight displacement.

for both the Manyi and Kokoxili earthquakes reveal several centimeters of line-of-sight transient displacement in both cases (Figure 2.10). The wavelength of the postseismic signal suggests that relaxation processes occur at a depth of 15-20 km, which is approximately the seismogenic depth in this area. A deformation time series for the Manyi event can be constructed from multiple interferograms, and yields a relaxation time of 0.7 years. It is

not possible to make early postseismic interferograms for the Kokoxili case, and so making a time series is difficult, but GPS data from a network of 65 sites either side of the rupture will ultimately give temporal information about the postseismic transient. We are currently waiting for postseismic data for the Yutian earthquake; coseismic interferograms have been processed, and show clear deformation fringes despite the ice cover in the area. Figure 2.10 shows interferograms for each of the three events.

5.3 Viscoelastic Models

In order to interpret the observed surface deformation in terms of sub-surface rheological structure, we implement models of postseismic stress relaxation in a viscoelastic medium. The idea here is that stress changes near the fault induced during the earthquake are relaxed due to viscous flow beneath an elastic upper crust. The thickness and viscosity of a Maxwell viscoelastic layer are varied in the models, and we seek parameters which best fit the data. For both the Manyi and Kokoxili cases, the best-fit viscosity is between 5×10^{18} and 1×10^{19} Pa·s; a single thick viscoelastic layer is preferred, suggesting that the entire mid to lower crust flows, with no stratification in viscous properties.

5.4 Future Work

A Maxwell viscoelastic medium is the simplest type of linear viscoelastic rheology, and it is reasonable to run initial models using such a rheology. However, the Manyi time series is not fit consistently throughout the entire 3.5 year observation period by a single Maxwell viscosity; rather, the effective viscosity increases over time. Another linear rheology which could produce this effect is a Burgers body, which consists of a Maxwell and a Kelvin element in series. We are currently running further models, varying the transient and steady-state viscosities as well as the ratio of Maxwell and long term shear moduli. Another candidate relaxation mechanism is localized afterslip on an extension of the coseismic rupture plane at depth. The data will also be tested against models simulating this mechanism. For strike-slip earthquakes such as Manyi and Kokoxili, surface deformation due to distributed viscous flow and localized afterslip can look very similar. The postseismic signature of the normal-faulting Yutian earthquake should be particularly useful for distinguishing between mechanisms, since the surface deformation from the two processes looks very different for dip-slip events.

5.5 Acknowledgements

This project is funded by NSF grant number EAR-0738298. All SAR data are from the European Space Agency (ESA), obtained through Category-1 Proposal No. 5119.

5.6 References

- Cook K.L. and L.H. Royden, The role of crustal strength variations in shaping orogenic plateaus, with application to Tibet. *J. Geophys. Res.*, 112, doi: 10.1029/2007JB005457, 2008.
- Funning, G., B. Parsons and T. Wright, Fault slip in the 1997 Manyi, Tibet earthquake from linear elastic modelling of InSAR displacements, *Geophys. J. Int.*, 169, 988–1008, 2007.
- Lasserre, C., G. Peltzer, F. Crampé, Y. Klinger, J. Van der Woerd and P. Tapponnier, Coseismic deformation of the 2001 Mw = 7.8 Kokoxili earthquake in Tibet, measured by synthetic aperture radar interferometry, *J. Geophys. Res.*, 110, B12408, 2005.
- Ryder, I., B. Parsons, T. Wright and G. Funning, Post-seismic motion following the 1997 Manyi (Tibet) earthquake: InSAR observations and modelling, *Geophys. J. Int.*, 169, 1009–1027, 2007.
- Thatcher, W., Microplate model for the present-day deformation of Tibet, *J. Geophys. Res.*, 112, B01401, 2007.

6. Automated Time-Domain Spike Identification for MT Data

Karl N. Kappler

6.1 Introduction

A method of automatic time domain spike identification for magnetotelluric array data is outlined. The algorithm exploits the simultaneous nature of geomagnetic variations at sites far (100's of km) away from one another. Data time series for instruments of the same field-type at various locations are windowed and condensed into time series of variances over the windows. Time series of the ratios of these variances are then scanned for outliers, where the definition of outlier is defined by an adaptive threshold. Examples are shown applying the method to a pair of MT stations in Central California, each with orthogonal electric dipoles and induction coil magnetometers. The method successfully identifies windows contaminated by spikes, DC offsets, and other strange variations. Only days where less than 10% of the data are contaminated are treated. A separate, but similar method not discussed here is employed to eliminate days where more than 10% of the data are contaminated.

6.2 Spike Identification

Magnetotellurics (MT) relies upon the recording of tiny variations in the earth's magnetic field. The spike identification is predicated on the assumption that these variations are horizontally polarized (spatially uniform) over 100's of km. In the absence of overwhelming noise, this implies that sensors at different sites will be strongly correlated, with the magnetic fields being nearly identical and the electric fields differing by a scale factor which depends on the local conductivity structure. This scale factor is approximately stationary as evidenced by the stability of intersite transfer functions [Eisel and Egbert 2002]. Figure 2.11 shows orthogonal electric and magnetic field data sampled at the earth's surface at two sites a distance of 120km apart. For a detailed description of the sites see [Kappler 2005]. Note the similarity in variations between channels of same orientation and field type, as well as identical scaling of the magnetic components, compared to the scale factor difference in the electric channels. This similarity can be seen to extend from periods of hours to seconds as shown by repeatedly zooming in on the data in Figures 2.12, 2.13, and 2.14.

This inherent similarity in the fields is exploited to identify windows in time when the array is not functioning correctly. Magnetotelluric data is prone to sudden sharp variations in signal of natural origin. These variations can be differentiated from variations whose origins are local noise by comparing channels at different sites, and flagging sharp variations which are not present ar-

raywide. A variety of statistics can be used to identify spikes. The statistic used here is simply the variance of each array channel over short time windows. The variance can be calculated directly in each time window, or alternatively, the variance of the first difference data can be calculated. The ratio of the variance in channels which record the same field type at the same orientation should be stationary about some typical value; in the case of magnetic fields, this value should be 1. In the case of electric fields, the value will be approximately stationary around some value, which reflects site effects such as local field distortion phenomena. The stationarity is only approximate because the observed fields' ratios will vary as a function of frequency, and hence electric field variance ratios will wander somewhat with the frequency content of the incident radiation. We approximately account for this by scaling the electric field data by a 'site factor' s_i which scales the i^{th} channel such that non-contaminated windows of channel i data have variance nearly equal to the variance of the same time window at a reference site. Formally, with the electric field data scaled in V/m and the magnetic field data still in instrument counts (effectively dB/dt), the time series of data collected by the i^{th} sensor S_i is represented as an N-point time series $\mathbf{x}_i(t)$. The N-point time series is chopped into windows of length L and overlap V, resulting in a total of $k=\text{floor}(N/(L-V))$ windows. Thus $\mathbf{x}_i(t)$ is represented as $\mathbf{X}_i(t)$, a $K \times L$ array, whose j^{th} row is the contiguous stream of data centered at $t=j^*(L-V)$. The last row of \mathbf{X} is taken as the final L points of \mathbf{x} in order to avoid zero-padding. The array \mathbf{X} is then contracted to a vector \mathbf{v} whose j^{th} element is the variance of the j^{th} row of \mathbf{X} . We thus obtain a windowed variance time series $\mathbf{v}_i(t)$ for each sensor, where the time increment for \mathbf{v} is $(L-V)$ times the sampling period of \mathbf{x} . In our example, we use day-long time series, sampled at 1Hz (hence $N=86400$), and set $L=256$, $V=64$, thus $k=450$.

The choice of window length should be sufficiently wide to account for possible intersite timing errors and FIR filter noise convolved on top of spikes, but sufficiently narrow that moderate sized spikes drive the window variance well above the value it would have without a spike. To apply the electric field scale factors, we look at the ratios of the \mathbf{v}_i for approximately parallel electrodes at the different sites. In our example, we use SAO as the reference site, and point-by-point ratios of \mathbf{v}_{ExSAO} to \mathbf{v}_{ExPKD} are examined together with point-by-point ratios of \mathbf{v}_{EySAO} to \mathbf{v}_{EyPKD} . Each cardinal sensor orientation is examined separately because of possible site distortion effects. Figure 2.15 shows the variance ratios over a four-year

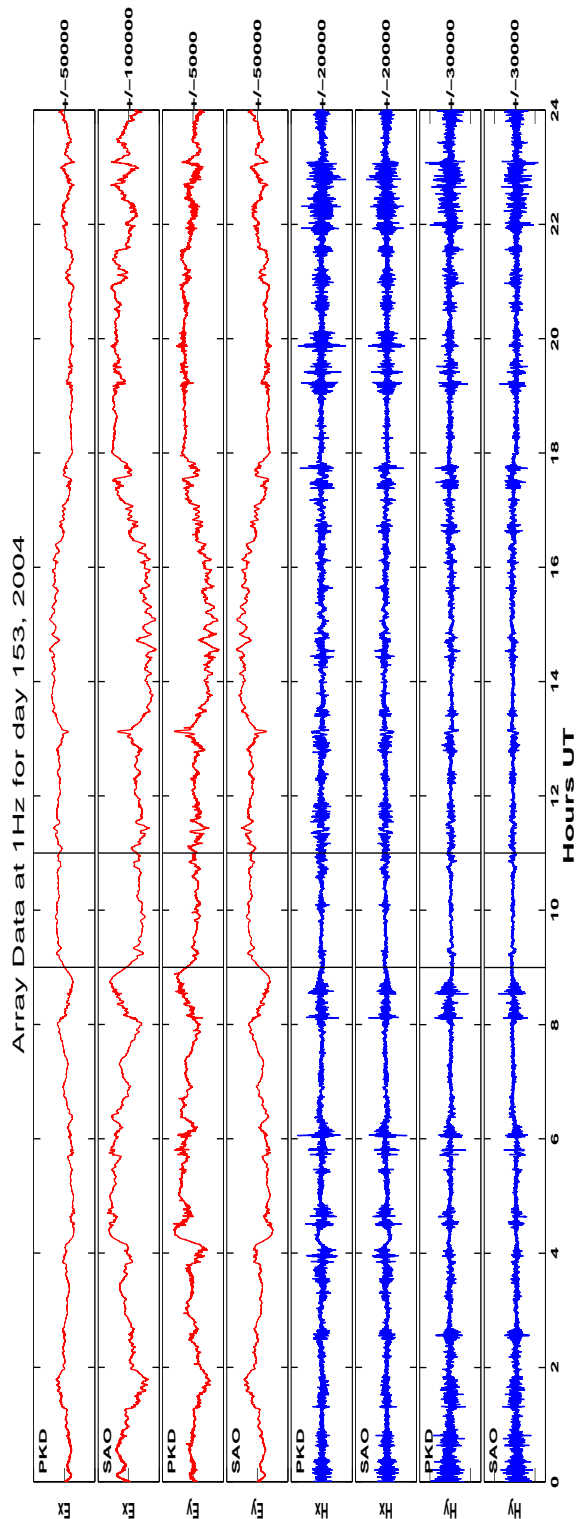


Figure 2.11: A plot of mean-subtracted array data for a full day in 2004. Electric fields are shown in red and magnetic fields in blue. Plots alternate between PKD and SAO at each field polarity. Y values are in counts with axis limits shown to the left. The vertical lines mark the domain boundaries of Figure 2.12.

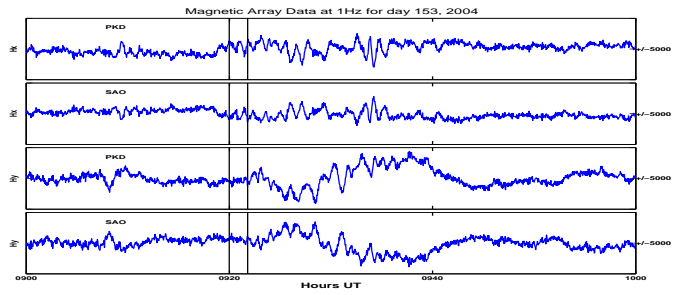


Figure 2.12: Detrended magnetic array data for one hour of the day shown in Figure 2.11. Plots alternate between PKD and SAO at each field polarity. The vertical lines mark the domain boundaries of Figure 2.13.

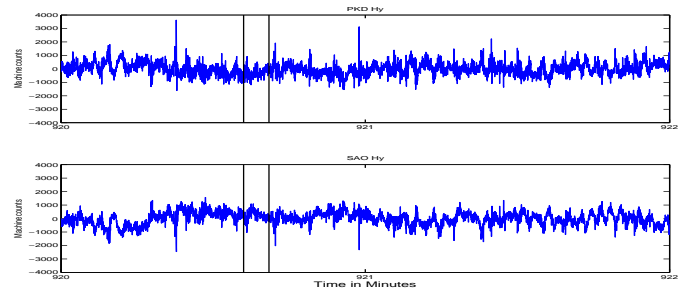


Figure 2.13: Detrended time series of y-polarity magnetic channels for two minutes within the hour shown in Figure 2.12. The vertical lines mark the domain boundaries of 2.14

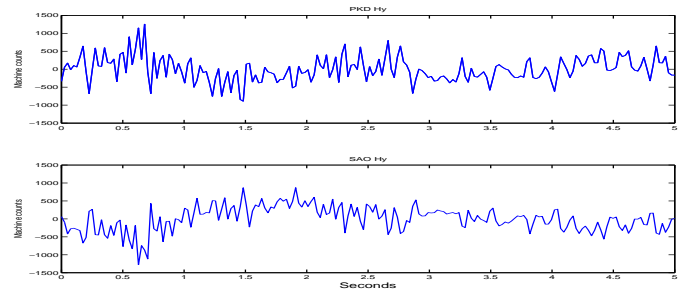


Figure 2.14: Detrended time series of y-polarity magnetic channels for 5 seconds within the window shown in Figure 2.13.

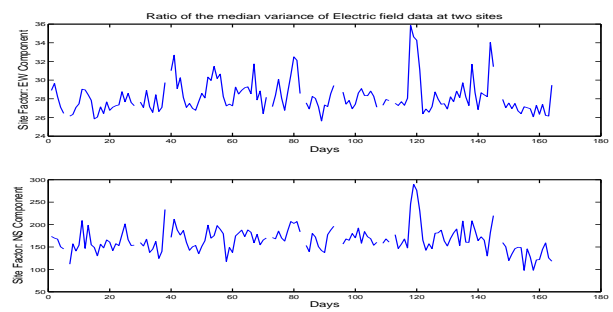


Figure 2.15: Each day, 450 windows of 256s length are input to calculate variance ratios. The daily median is shown above. Note the relative anisotropy between sites.

window. Note that there is a significant difference in the ratio amplitudes between the two cardinal orientations, a median of 28 for EW and 148 for NS, implying a relative electrical anisotropy between the two sites. Some seasonal effects are also apparent, as are offsets due to instrument swaps, or times when sites were not functioning properly. In general however, the ratio is reasonably stable, and stationary on a day-to-day basis. The EW electric field at PKD is thus scaled by $\sqrt{28}$ or equivalently \mathbf{v}_{EewPKD} is scaled by 28, and similarly for the NS component. With E field data appropriately scaled, we recalculate the $\mathbf{v}_i(t)$, but this time the rows of \mathbf{X}_i are first-differenced before variances are calculated. Windows of anomalous variance can now be flagged. Each $\mathbf{v}(t)$ is associated with a two digit code, one digit for field type (E or H) and one for orientation. Channels with the same codes are grouped together (we assume that sites are not significantly rotated w.r.t one another). Within each pairing, the log ratio \mathbf{r} of the variance time series is calculated:

$$\mathbf{r}_{i,j}(t) = \log_{10}\left(\frac{\mathbf{v}_i(t)}{\mathbf{v}_j(t)}\right)\forall t \quad (2.1)$$

For each grouping, the median-subtracted time series $\mathbf{r}(t)$ is searched independantly over each day. An anomalous window at time t is flagged if $\mathbf{r}(t)$ is greater than a threshold. The threshold is chosen adaptively each day as M times the two-sided α -trimmed standard deviation of \mathbf{r} . The two-sided α -trimmed standard deviation of a time series $\mathbf{r}(t)$ is defined as the standard deviation of the collection of all elements of \mathbf{r} which are larger than the $\alpha/2^{th}$ percentile and less than the $(100-\alpha/2)^{th}$. Using this measure prevents a few very large spikes from driving the standard deviation up so high that smaller spikes are not caught. Practically speaking, $n=5$ works well for magnetic fields, and $n=6$ for electrics, with α set to 0.03. Plotted in Figure 2.16 are some examples of the spike ID method. On the left are shown one day's worth of $\mathbf{r}(t)$. The horizontal lines denote the M α -trimmed standard deviation thresholds. The vertical dashed line coincides with a time-window where a channel has been flagged as having a spike. The corresponding plot on the right shows the channel with spike and its 'sister channel' at the other site. The channels used for the numerator of the ratio are shown in blue, and the denominator channels are shown in green. The algorithm described only identifies windows where the variance ratio between two channels is anomalous. Deciding which of the two channels corresponds to non-physical data is another matter. For spikes and sharp offsets, the channel with more energy in the scaled time series is selected as the offending data. One need beware that a malfunctioning amplifier in some system component could result in a channel with a signature smaller than average variance. In this case, the algorithm will flag a normally functioning channel as spiky.

6.3 Conclusions

The method seems to work well. It has application in the monitoring of array health, and possibly in other mutichannel systems where channels typically record stationary time series. There are a very few cases where the method misidentifies data as being a spike. Addition of a hard threshold insisting that spikes be ID-ed as windows having \mathbf{v} greater than 0.3 or M alpha trimmed stds, whichever is greater, seems to protect agianst this. There are several parameters which control the algorithm; these are: initial time series lengths (N), window length (L), window overlap (V), whether or not to 'first-difference the data' (boolean), α (percent of data to reject when calculating thresholds), and M, the threshold multiplier. A code has been written which incorporates these variables into a few simple scripts. Four years of data at 1Hz can be rapidly despiked in a short amount of time.

6.4 References

- Egbert, G.D., Booker, J.R., Multivariate Analysis of Geomagnetic Array Data 1. The Response Space, *Journal of Geophys. Res.*, V94 No.B10 pp14227-14247, 1989
- Eisel M., Egbert G.D., (2001), On the stability of magnetotelluric transfer function estimates and the reliability of their variances, *Geophys. J. Int.*, 144, pp65-82, 2001
- Kappler, K.N., Morrison, H.F., Egbert, G.D., Parkfield-Hollister Electromagnetic Monitoring Array, *BSL Annual Report*, 2005-06

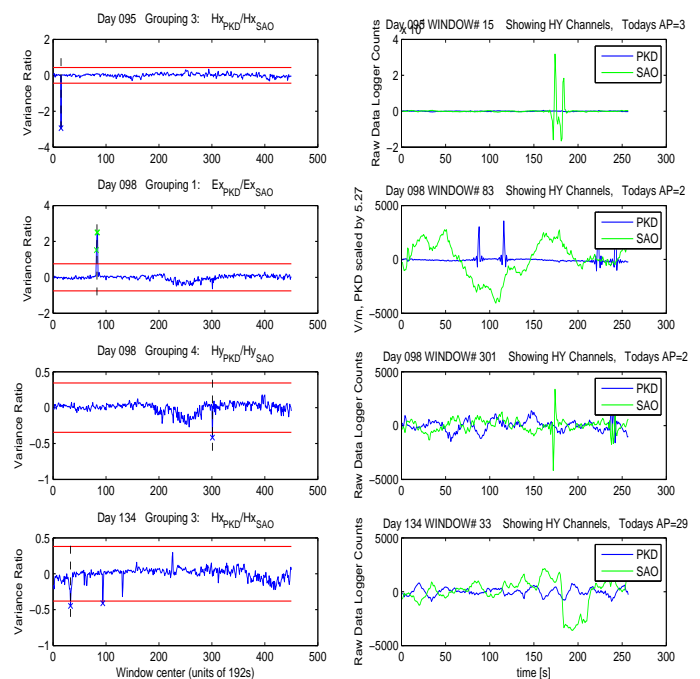


Figure 2.16: Variance ratio time series, together with adaptive threshold bars (left) raw time series (right) for window in time denoted by vertical line on left.

7. Stress Changes on the Sunda Megathrust Preceding the M_w 8.4 2007 Earthquake

Kelly Grijalva, Roland Bürgmann, and Edwin (Trey) Apel

7.1 Introduction

The M_w 8.4 September 12, 2007 Sumatra earthquake's occurrence, close in time and space to the 2004 Sumatra-Andaman and 2005 Nias megathrust events, suggests that it could be a triggered earthquake. The 2007 earthquake initiated ~ 750 km south of the 2005 epicenter, in the southern portion of the historic 1833 rupture zone. Earlier studies of vertical motion, derived from coral growth histories, suggest that interseismic strain accumulating along the 1833 segment had approached levels relieved in the historic earthquake (*Natawidjaja et al.*, 2006). We investigate why the portion of the Sunda subduction zone between the 2005 and 2007 rupture patches, which previously slipped in 1797, did not rerupture or rupture with the 2007 event.

7.2 Coulomb Failure Stress Models

We model the coseismic and viscoelastic postseismic deformation from the 2004-2005 earthquake sequence in order to quantify its influence on the hypocentral region of the 2007 earthquake. The elastic coseismic deformation is calculated in a layered spherical geometry using the method of *Pollitz* (1996) and previously published source parameters (*Banerjee et al.*, 2006; *Konca et al.*, 2007; *Zhou et al.*, 2002). Viscoelastic relaxation is calculated using the method of *Pollitz* (1992), with a bi-viscous rheology in the asthenosphere that includes an initial short-term viscosity of 5×10^{17} Pa s and a long-term viscosity of 1×10^{19} Pa s (*Pollitz et al.*, 2006). We use the deformation calculations to model the Coulomb failure stress (CFS) changes along the Sunda megathrust. Previous studies have shown that CFS increases of 1-3 bars are generally sufficient to trigger seismicity and sometimes even a few tenths of a bar appear sufficient to advance (or retard) the occurrence of large earthquakes (e.g. *Rydelek and Sacks*, 1999; *Lin and Stein*, 2004). We use a CFS function given by $CFS = \Delta\tau + \mu'\Delta\sigma_n$, which defines CFS as a sum of the change in shear stress τ and the change in normal stress (clamping is negative) σ_n , multiplied by an effective coefficient of friction. We assume low frictional fault strength and use an effective coefficient of friction, $\mu' = 0.1$. CFS changes are resolved onto the down-going Sunda slab, with dips increasing at depth, and rake varying along strike.

Although the 2004 event was a M_w 9.2, the ~ 950 km separation distance prevented the coseismic and postseismic CFS changes at the 2007 hypocenter from being > 0.1 bars. The 2005 earthquake was also too far from

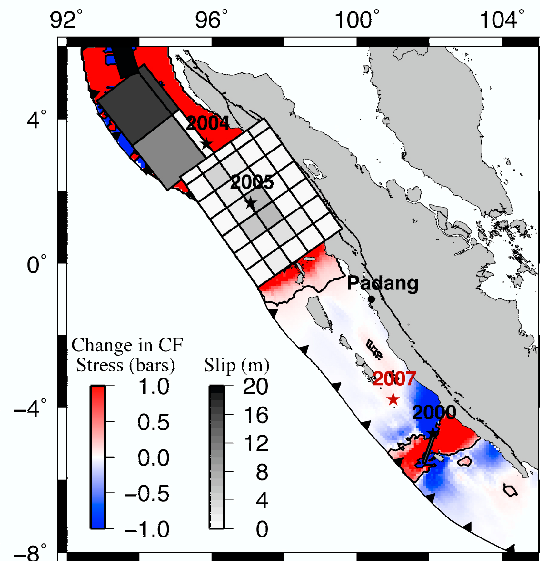


Figure 2.17: Total CFS changes resulting from the combination of the 2000, 2004, and 2005 coseismic and postseismic deformation on the Sunda megathrust. The 0.1 bar contour is plotted in black and the earthquake source models overlay the CFS changes.

the 2007 hypocenter to produce significant CFS changes. The 2004-2005 sequence did produce a slightly negative CFS change in the 1797 rupture patch. Notably, the largest contributor to positive CFS change at the southern portion of the 2007 rupture zone was the M_w 7.9 2000 earthquake. However, the 2000 earthquake still did not produce > 0.1 bars CFS changes at the 2007 hypocenter (Figure 2.17).

7.3 Seismicity Rate Changes

We investigated seismicity changes following the 2004 earthquake using the standard beta-statistic approach (*Hough*, 2005). Beta is defined as $\beta = (N_a - N_e) / \sqrt{\text{variance}}$, where N_a is the number of earthquakes occurring after a major event and N_e is the expected number of earthquakes. Beta will be large and positive when there is increased seismic activity. We compare the annual seismicity $M \geq 4.5$ following the 2004 event with the previous fifteen years of earthquakes. Figure 2.18 shows the beta values for the Sumatra region at the

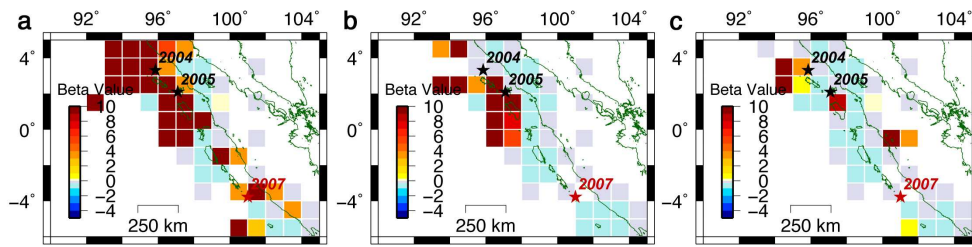


Figure 2.18: Beta values showing the relative change in seismicity following the 2004 earthquake in a) 2005, b) 2006, c) 2007 up to the September earthquake. All beta values are based on seismicity between 15-30 km depth.

depth range of 15-30 km, which includes the depth of the 2007 earthquake. Based on the high beta values, seismicity increased in the vicinity of the 2007 event during the months following the 2004 and 2005 megathrust earthquakes. In 2005, seismicity also increased near Siberut Island, at the northern end of the 2007 rupture patch. This increased seismicity may be related to aseismic slip on the Sunda megathrust, which could have further stressed the 2007 hypocentral region. During 2006 and 2007, the seismicity level dropped off to average conditions at the 2007 hypocenter location.

7.4 Discussion and Future Work

CFS change at the 2007 hypocenter, resulting from the combined 2004-2005 coseismic and postseismic deformation, is likely too small to have triggered the recent earthquake. The slightly negative CFS change in the northern 1797 rupture patch, resulting from the 2004-2005 earthquake sequence, may have delayed the recurrence of the 1797 earthquake. The smaller 2000 earthquake turns out to have had the largest CFS change at the 2007 hypocenter and may help to explain the southern location of the 2007 earthquake. Furthermore, increasing the oblique component to the slab receiver fault geometry, as observed with the larger than average 114° slip direction for the 2007 earthquake, amplifies this positive CFS change. Investigations of the beta-statistic, for the years following the 2004 earthquake, show that there was increased seismic activity during 2005 on the ends of the 2007 rupture patch. We are starting to analyze geodetic data for the years 2005-2007 in order to assess whether accelerated aseismic slip contributed significantly to the timing and location of the 2007 earthquake.

7.5 Acknowledgments

This work is supported by the National Science Foundation grant EAR 0738299.

7.6 References

Banerjee, P. B., F. F. Pollitz, B. Nagarajan, and R. Bürgmann, Coseismic slip distributions of the 26 De-

cember 2004 Sumatra-Andaman and 28 March 2005 Nias earthquakes from GPS static offsets, *Bull. Seism. Soc. Am.*, *97*, S86-S102, 2006.

Hough, S. E., Remotely triggered earthquakes following moderate mainshocks (or, why California is not falling into the ocean), *Seism. Res. Lett.*, *76*, 58-66, 2005.

Konca, A. O., V. Hjorleifsdottir, T. A. Song, J. Avouac, D. V. Helmberger, C. Ji, K. Sieh, R. Briggs, and A. Meltzner, Rupture kinematics of the 2005 M_w 8.6 Nias-Simeulue earthquake from the joint inversion of seismic and geodetic data, *Bull. Seism. Soc. Am.*, *97*, S307-S322, 2007.

Lin, J. and R. S. Stein, Stress triggering in thrust and subduction earthquakes and stress interaction between the southern San Andreas and nearby thrust and strike-slip faults, *J. Geophys. Res.*, *109*, 10.1029/2003JB002607, 2004.

Natawidjaja, D. H., K. Sieh, M. Chlieh, J. Galetzka, B. W. Suwargadi, H. Cheng, R. L. Edwards, J. Avouac, and S. N. Ward, Source parameters of the great Sumatran megathrust earthquakes of 1797 and 1833 inferred from coral microatolls, *J. Geophys. Res.*, *111*, 10.1029/2005JB004025, 2006.

Pollitz, F. F., Postseismic relaxation theory on the spherical earth, *Bull. Seism. Soc. Am.*, *82*, 422-453, 1992.

Pollitz, F. F., Coseismic deformation from earthquake faulting on a layered spherical earth, *Geophys. J. Int.*, *125*, 1-14, 1996.

Pollitz, F. F., P. Banerjee, R. Bürgmann, M. Hashimoto, and N. Chhoosakul, Stress changes along the Sunda trench following the 26 December 2004 Sumatra-Andaman and 28 March 2005 Nias earthquakes, *Geophys. Res. Lett.*, *33*, 10.1029/2005GL024558, 2006.

Rydelek, P. A. and I. S. Sacks, Large Earthquake occurrence affected by small stress changes, *Bull. Seism. Soc. Am.*, *89*, 822-828, 1999.

Zhou, Y. H., L. S. Xu, Y. T. Chen, Source process of the 4 June 2000 Southern Sumatra, Indonesia, Earthquake, *Bull. Seism. Soc. Am.*, *92*, 2027-2035, 2002.

8. GPS exploration of the elastic properties across and within the Northern San Andreas Fault zone and heterogeneous elastic dislocation models

Romain Jolivet (Ecole Normale Supérieure de Paris), Roland Bürgmann and Nicolas Houlié

8.1 Introduction

The Northern San Francisco Bay Area (hereafter “North Bay”) is sliced by three major right-lateral strike-slip faults: the northern San Andreas Fault (SAF), the Rodgers Creek Fault (RCF) and the Green Valley Fault (GVF). The RCF represents the North Bay continuation of the Hayward Fault Zone, and the GVF is the northern extension of the Concord Fault. North of the juncture with the San Gregorio Fault, geodetic and geologic data suggest a SAF slip rate of 20-25 mm/yr (d’Alessio *et al.*, 2007, Lisowski *et al.*, 1991). Geodetically determined slip rates range from $20.2 \pm 1.4 mm/yr$ (d’Alessio *et al.*, 2007) to $23 \pm 3 mm/yr$ (Freymueller *et al.*, 1999). The remainder of the 40 mm/yr of Pacific plate to Sierra Nevada Great Valley microplate motion is primarily accommodated by the RCF and the GVF.

Earthquake cycle deformation is commonly modeled assuming laterally homogeneous elastic properties in the Earth’s crust. First-order variations in rock elastic strength both across and within fault zones can, however, strongly impact inferences of fault slip parameters and earthquake rupture characteristics. Near Point Reyes, the SAF separates two different geologic terranes. On the east side of the fault is the Franciscan Complex, made of a mixture of Mesozoic oceanic crustal rocks and sediments, which were accreted onto the North American continent during subduction of the Farallon plate. On the west side of the SAF is the Salinian terrane, which is composed of Cretaceous granitic and metamorphic rocks, overlain by Tertiary sedimentary rocks and Quaternary fluvial terraces. Prescott and Yu (1986) and Lisowski *et al.* (1991) describe an asymmetric pattern along a geodetically measured surface velocity profile across to SAF at Point Reyes, which can be explained by higher rigidities to the SW of the fault. Le Pichon *et al.*, 2005, also describes an asymmetric pattern further north along the SAF, at Point Arena, but not at Point Reyes. Chen & Freymueller, 2002, rely on near-fault strain rates determined from trilateration and GPS measurements to infer a 2-km-wide near-fault compliant zone (with 50% reduced rigidity) near Bodega Bay and Tomales Bay. Here we use densely spaced GPS velocities across the SAF to evaluate changes in elastic properties and within the SAF zone.

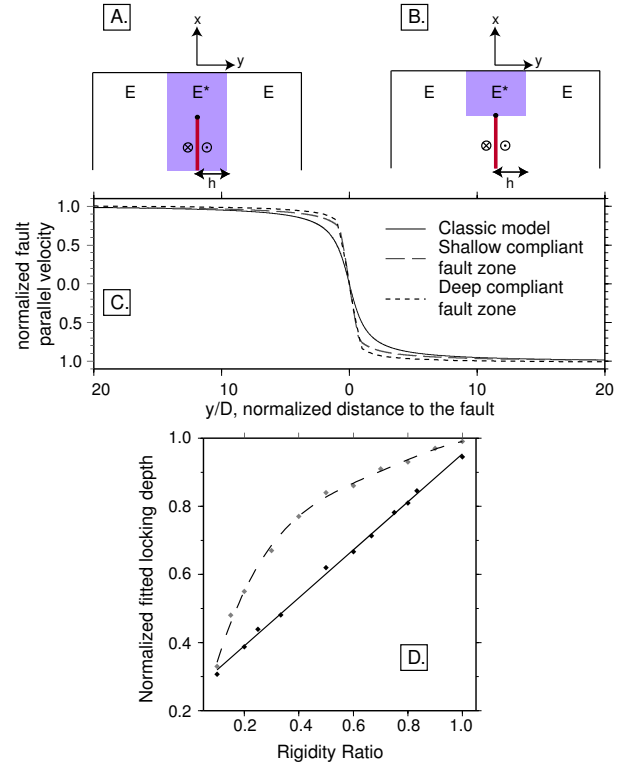


Figure 2.19: Model geometry of A. deep and B. shallow CFZM. The shaded area is the weak fault zone. C. Comparison between a 10 km locking depth classic screw dislocation model (continuous line), a 10 km locking depth Shallow CFZM (long-dashed grey line) and a 10 km locking depth Deep CFZM (dashed black line) with rigidity in the 2-km-wide fault zone being reduced by 80%. D. Locking depth determined by fitting velocity profiles (400 km long with a point spacing of 0.5 km) calculated with the CFZMs with the half-space equation 2.2. The grey dots are the best-fit locking depth for the deep CFZM and the dashed line is the corresponding polynomial fit. The black dots are the fitted locking depth for the shallow CFZM and the continuous line is the corresponding linear fit.

8.2 Heterogeneous Elastic Models

The classic way to interpret a GPS-derived velocity profile across a strike-slip fault is, assuming that the movement is only horizontal, to use the screw dislocation

tion model (*Savage and Burford, 1973*):

$$v(y) = \frac{v_{max}}{\pi} \text{atan}\left(\frac{y}{D}\right) \quad (2.2)$$

Where v is the predicted fault-parallel velocity of a surface point at distance y from the fault and v_{max} is the far field velocity. v_{max} is also the slip rate on the dislocation below the locking depth D . This model assumes an infinite dislocation buried in a semi-infinite elastic medium. Next we consider laterally heterogeneous models that account for variation of elastic properties across and within the fault zone.

We first consider the model developed by *Le Pichon et al., 2005*, where the fault separates two elastic media, with different Young's modulus E_1 and E_2 . They consequently use a rigidity ratio, K , in the following equations:

$$y < 0 \Rightarrow V(y) = KV_{max} + \left(\frac{2KV_{max}}{\pi}\right) \text{atan}\left(\frac{y}{D}\right) \quad (2.3)$$

$$y > 0 \Rightarrow V(y) = KV_{max} + \left(\frac{2(1-K)V_{max}}{\pi}\right) \text{atan}\left(\frac{y}{D}\right)$$

Where $V(y)$ is again the velocity at a distance y from the fault, V_{max} is the far field velocity, D the locking depth, and $K = \frac{E_2}{E_1 + E_2}$ is the asymmetry ratio.

We also evaluate the deep Compliant Fault Zone Model (CFZM) developed in *Chen & Freymueller, 2002*, following *Rybicki and Kasahara, 1977*. A low rigidity fault zone is introduced between two elastic blocks (Figure 2.19).

This model (A. in Figure 2.19) is based on an infinitely deep weak fault zone. If we consider that the fault zone is weak because of damage caused by repeated earthquakes, this zone should not extend deeper than the locking depth. Therefore, we developed, using Finite Element Modeling (*Chéry et al., 2001*), a shallow CFZM (B. in Figure 2.19). Both models tend to localize the deformation close to the fault trace, but the shear is more localized in the shallow CFZM.

We tried to fit the computed velocity profiles obtained with both CFZMs with the classic screw dislocation model, to evaluate the trade-off between the rigidity ratio and the obtained best-fit locking depth. For both models, there is an inverse relationship between the rigidity ratio and the fitted locking depth (linear for the deep CFZM and curved for the shallow CFZM). As the difference between the CFZMs and the fitted classic models is smaller than the typical error obtained with geodetic data (typically 1 mm/yr), we cannot distinguish between a shallow locking depth and a compliant fault zone, relying only on geodetic data. Thus it is important to have independent constraints on the locking depth, for instance, from the depth extent of microseismicity.

8.3 GPS velocities along the Northern San Andreas Fault

We collected GPS data in Bodega Bay and Tomales Bay, using 1996-2000 GPS measurements from *Chen & Freymueller (2002)* to calculate the velocities. We also used data from the Point Reyes profile, provided by the Bay Area Velocity Unification (BAVU), a compilation of the San Francisco bay area GPS velocities (*d'Alessio et al., 2005*). The data are processed using the GAMIT/GLOBK GPS analysis software. The site velocities are shown with respect to BARD continuous GPS station LUTZ in Figure 2.20.

A first analysis with a simple screw dislocation model, based on three parallel faults (SAF, RCF and GVF) provides a $23 \pm 1 \text{ mm/yr}$ slip rate on the SAF, with a $14 \pm 2 \text{ km}$ locking depth, while the whole system is accommodating 40 mm/yr of fault parallel displacement (we find a $8 \pm 1 \text{ mm/yr}$ slip rate on the RCF and $9 \pm 1 \text{ mm/yr}$ on the GVF)(Figure 2.20). *d'Alessio et al. (2007)* show that the velocity of the Farallon islands with respect to the Pacific plate is about 2.9 mm/yr , consistent with our modeled velocity field. But the half-space model velocity for the Farallon Island station is 4 to 5 mm/yr faster than the actual measured velocity. We next consider asymmetric models with a rigidity contrast across the SAF, fitting the data with equation 2.3. We find that the modeled velocity profile better matches the Farallon Islands velocity with a 0.41 K ratio. Thus, we infer that the Salinian terrane has a rigidity 1.4 times higher than the Franciscan complex to the east of the SAF. Our results suggest an 18 mm/yr slip rate on the SAF, with a 10 km locking depth. There is a significant trade-off between the inferred slip rate on the SAF and the rigidity contrast across the fault, with smaller rigidity contrasts leading to higher inferred slip rates.

The two networks across the SAF located further north, one in Tomales Bay and one in Bodega Bay, allow us to consider if the SAF represents a low-rigidity fault zone. Our preferred model for the Tomales Bay profile is a classic dislocation, with a 21 mm/yr slip rate on the SAF, with a 12 km locking depth. We did not explore the corresponding trade-off, but, as our data set doesn't extend far away on both side of the fault, even using the PS-SAR data from *Funning et al., 2007*, the determined parameters are not well constrained. In Bodega Bay, our preferred model is based on a deep CFZM, with a 28 mm/yr slip rate on the SAF, with a 15 km locking depth. The compliant zone is 40% weaker than the surrounding medium. But a classic homogeneous model with a 24 mm/yr slip rate and a 7 km locking depth on the SAF satisfies the near-field data as well, as shown by the first-order trade-off between locking depth and the compliant fault zone rigidity contrast we found in the previous section. We prefer a 15 km locking depth and, consequently, introducing this deep CFZM because

of the microseismicity near the Point Reyes profile, assuming that there is no significant change in the locking depth.

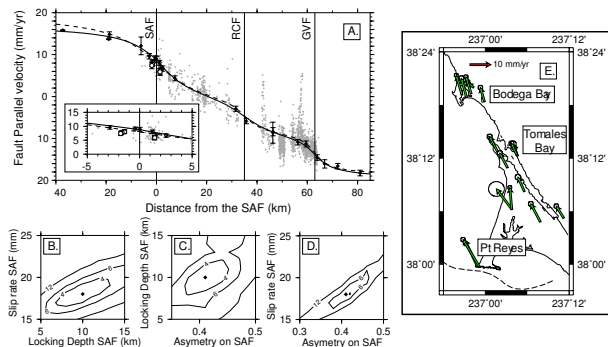


Figure 2.20: A. Best fit dislocation models for the Point Reyes profile. The black dots are the fault-parallel projected GPS velocities with their associated error bars. The grey dots are the PS-SAR data from (Funning *et al.*, 2007). The dashed line is the best classic (elastic half-space) dislocation model. The continuous line is our preferred asymmetric model with a K ratio of 0.41 that better matches the observed velocity of the westernmost GPS site on the Farallon Islands. B. Trade off between the Locking Depth and the Slip Rate on the SAF. Contoured values are the sum of the weighted squared residuals divided by the number of data points C. Trade off between the Asymmetry Ratio and the Locking Depth on the SAF. D. Trade off between the Asymmetry Ratio and the Slip Rate on the SAF.

8.4 Acknowledgements

This project was funded by the USGS National Earthquake Hazard Reduction Program (NEHRP). We would like to thank J. Freymueller for his help during the GPS survey. Thanks to R. Bürgmann for having me in his team during 6 months and to all the Berkeley Active Tectonics Group.

8.5 References

d'Alessio, M. A., Johanson, I. A., Bürgmann, R., Schmidt, D. A. and Murray, M. H., Slicing up the San Francisco Bay Area: Block kinematics and fault slip rates from GPS-derived surface velocities, *J. Geophys. Res.*, *110*, B0640, 2007.

Chen, Q. and Freymueller, J. T., Geodetic evidence for a near-fault compliant zone along the San Andreas Fault in the San Francisco Bay Area, *J. Geophys. Res.*, *92*, 2002.

Chéry, J., Zoback, M. and Hassani, R., Rheology, strain and stress of the San Andreas Dault in Central

and Northern California: A 3-d thermomechanical modeling study, *J. Geophys. Res.*, *106*, , B08406, 2001.

Freymueller, J. T., Murray, M. H., Segall, P. and Castillo, D., Kinematics of the Pacific-North America plate boundary zone, Northern California, *J. Geophys. Res.*, *104*, 7419-7442, 1999.

Funning, G. J., Bürgmann, R., Ferretti, A. and Fumagalli, A. Creep on the Rodgers Creek Fault, northern San Francisco Bay Area, from 10 year ps-insar dataset. *submitted*, 2007.

Le Pichon, X., Kreemer, C. and Chamot-Rooke, N., Asymmetry in elastic properties and the evolution of large continental strike-slip faults, *J. Geophys. Res.*, *110*, B03405, 2005.

Lisowski, M., Savage, J. C. and Prescott, W. H., The Velocity Field Along the San Andreas Fault in Central and Southern California, *J. Geophys. Res.*, *96*, 8369-8389, 1991.

Prescott, W. H. and Yu, S. B., Geodetic measurement of horizontal deformation in the northern San Francisco Bay region, California, *J. Geophys. Res.*, *91*, 7475-7484, 1986

Savage, J. and Burford, R., Geodetic determination of relative plate motion in Central California, *J. Geophys. Res.*, 1973

9. A look in the eyes of hurricanes by Global Positioning System

Nicolas Houlié and Gaetano Festa

9.1 Introduction

The landfall of Hurricanes Frances, Charley, Jeanne, and, more recently, Katrina caused billions of dollars in damage to structures and property, the loss of thousands of lives, and displaced millions of people during the summers 2004 and 2005.

In order to mitigate the risk associated with hurricanes and tropical storms, several studies attempted to predict their occurrence, estimate their number and understand their behavior from birth to death (*De Pondaca and Zou, 2001; Powers and Davis, 2002; Wang and Wu, 2004; Larcombe and Carter, 2004; McConochie et al., 2004; Xu et al., 2005; Tolman and Alves, 2005; Lu and Garrido, 2005; Emanuel, 2005*). Accuracy in the prediction strongly depends on observations such as the temperature and pressure vertical profiles that constrain the modelling of thermodynamic processes involved inside the convection cell. Due to high-speed wind in the outer part of the turbine, however, actual operational tools are limited to measurements at the Earth surface, above and inside the eye of the hurricane. There is thus a need for an instrument capable of scanning the entire hurricane. In order to scan the outer part of the hurricane, which is the most humid and windy, several instruments are limited because they need light (i.e. LASER system) or because the wind velocity is too high (balloons). GPS is strongly attached to the ground and can work in extreme conditions, night and day. The particular sensitivity of the GPS to water vapour in the atmosphere allows us to constrain the temperature profile in the wet part of a hurricane. Indeed, the radio waves emitted by each GPS satellite are delayed by the water vapor contained in the troposphere and can therefore be used as a powerful scanner of the lower atmosphere (*Baby et al., 1988; Bevis et al., 1992; Rocken et al., 1993; Brunner et al., 1993; Bevis et al., 1994; Rocken et al., 1995; Bevis et al., 1996; Rocken et al., 1997; Coster et al., 1998; Ruffini et al., 1999; Pany et al., 2001*). These studies encourage the use of GPS in order to determine the atmosphere state by using both GPS and ground based measurements. However, GPS has not yet been used to investigate hurricanes.

The paths of Hurricanes Charley, Frances, Jeanne, and Katrina have crossed the GPS network in the Southeast United States (Figure 2.21), allowing us to explore perturbations in pressure, temperature and relative humidity due to the passage of hurricanes in the troposphere.

In this paper, we specifically quantify the change of the vertical temperature profile in the wet part of Katrina during its passage over the Louisiana coast.

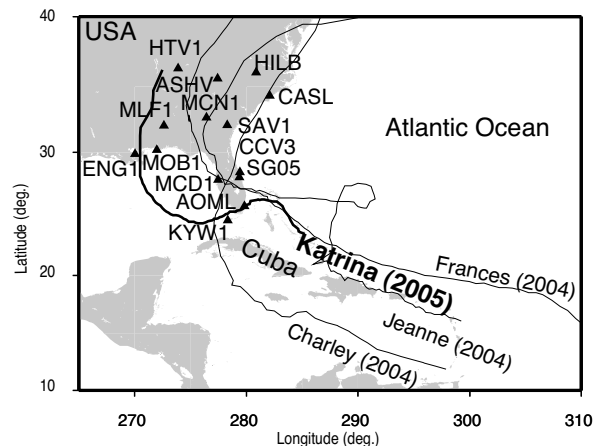


Figure 2.21: The GPS network used in this study. The sites belong to the GPS-MET and IGS networks. Superimposed on the picture, we also plot the paths of the hurricanes that hit the Southeast United States during the summers of 2004 and 2005. The trajectories are derived from MODIS Observation.

9.2 Results

Since we fix the ground temperature at 25°C , the increase in the wet tropospheric delay can be interpreted as an average increase of the temperature along the whole air column above the station. We quantified the vertical gradient increase to be $1^{\circ}\text{C}/\text{km}$. An analogous increase of the temperature vertical gradient has been observed in the central part of the hurricane by dropsonds and Microwave Imager Sounder, with a maximum difference comparable with results presented here.

9.3 Discussion

GPS networks, dedicated to tectonic and geodynamic problems in the US-Caribbean area, could be densified by adding instrumentation on boats or/and islands and could become a forecast tool to study the hurricanes, remotely, in 3D, by night and by day.

Our results suggest that we could evaluate the radial variations of the vertical temperature profile in the wet part of the hurricanes using GPS, improving the real-time state of the hurricanes and allowing for short-term prediction of the trajectory of hurricanes. These profiles would be directly related to the distance between the GPS receivers, the position of which is known, and the eye of the hurricanes, the location of the latter being accurately computed by remote sensing imagery (e. g.

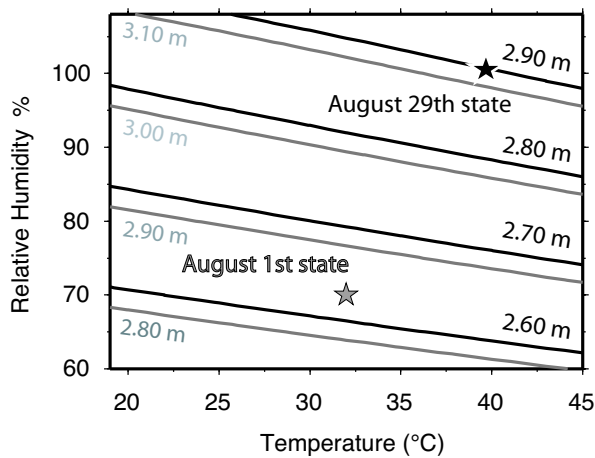


Figure 2.22: Abacus presenting the increase of the tropospheric delay as a function of the temperature T and the relative humidity H . Gray lines represent the tropospheric delay contours for the pressure value of 1.013 bar, as measured on August 1, while black lines are drawn for the pressure value of 916 mbar, as measured on August 29.

MODIS, SPOT). Non-linearity in the hurricane trajectory is owed to sharp changes in the temperature at the sea surface and to the presence of sparse islands. Indeed, the use of GPS measurements could also help describe the air column's state above the starting areas of hurricane, better constraining the prediction of its future path.

The integration of 2D or 3D effects that may not be secondary for the evaluation of the tropospheric delays will be the next step of GPS applications to hurricanes.

References

- H. Baby, P. Golé, and A. Lavergnat, J. Model for tropospheric excess path length of radio waves from surface meteorological measurements. *Radio Science*, 22:1023–1038, 1988.
- M. Bevis, S. Businger, T. A. Herring, C. Rocken, R. A. Anthes, and R. H. Ware. GPS Meteorology: Remote Sensing of Atmospheric Water Vapor Using the Global Positioning System. *J. Geophys. Res.*, 97(16):15787–15801, October 1992. doi: 10.1029/92JD01517.
- M. Bevis, S. Businger, S. Chiswell, T.A. Herring, R.A. Anthes, C. Rocken, and R.H. Ware. Gps meteorology: Mapping zenith wet delays onto precipitable water. *Journal of Applied Meteorology*, 33(3):379–386, 1994. doi: 10.1175/1520-0450(1994)033<0379:GMMZWD>2.0.CO;2.
- M. Bevis, S. Chiswell, S. Businger, T. T. Herring, and Y. Bock. Estimating Wet Delays Using Numerical Weather Analyses and Predictions. *Radio Sci.*, 31(3):477–487, 1996.
- A.J. Coster, A.E. Niell, F.S. Solheim, V.B. Mendes, P.C. Toor, R.B. Langley, and C.A. Upham. The Westford Water Vapor Experiment: Accuracy issues involving the use of GPS to measure total precipitable water vapor. In *Preprints of the 10th Symposium on Meteorological Observations and Instrumentation*, pages J70–J75. 78th Annual Meeting of the American Meteorological Society, 1998.
- M. S. F. V. De Ponte and X. Zou. A case study of the variational assimilation of gps zenith delay observations into a mesoscale model. *Am. Meteor. Soc.*, 40:1559–1576, 2001.
- K.A. Emanuel. Increasing destructiveness of tropical cyclones over the 30 years. *Nature*, 436, 2005.
- R. Hanssen. Atmospheric heterogeneities in ERS tandem SAR interferometry, Chapter 2. *DEOS Report*, 98.1:8–24, 1998.
- P. Lacombe and R.M. Carter. Cyclone pumping, sediment partitioning and the development of the great barrier reef shelf system: a review. *Quaternary Science Reviews*, 23: 107–135, 2004.
- Y. Lu and J. Garrido. Doubly periodic non-homogeneous Poisson models for hurricane data. *Statistical Methodology*, 2:17–35, 2005.
- J.D. Mc Conochie, T.A. Hardy, and L.B. Mason. Modelling tropical cyclone over-water wind and pressure fields. *Ocean Engineering*, (31):1757–1782, 2004.
- T. Pany, P. Pesec, and G. Stangl. Atmospheric GPS slant path delays and ray tracing through numerical weather models, a comparison. *Physics and Chemistry of the Earth A*, 26:183–188, January 2001.
- J. Powers and C.A. Davis. A cloud-resolving regional simulation of tropical cyclone formation. *Atmospheric Science Letters*, 3(1):15–24, 2002.
- C. Rocken, T. Van Hove, J. Johnson, F. Solheim, R. Ware, M. Bevis, S. Chiswell, and S. Businger. GPS/STORMGPS sensing of atmospheric water vapor for meteorology. *Jour. of Atmos. and Ocean. Tech.*, 1995, 12 (3):468–478, 1995.
- C. Rocken, T. Van Hove, and R. Ware. Near real-time GPS sensing of atmospheric water vapor. *Geophys. Res. Lett.*, 24:3221–3224, December 1997. doi: 10.1029/97GL03312.
- Rocken, C. and Ware, R. and Van Hove, T. and Solheim, F. and Alber, C. and Johnson, J. . Sensing atmospheric water vapor with the global positioning system. *Geophys. Res. Lett.*, 20:2631–2634, 1993.
- G. Ruffini, L.P. Kruse, A. Rius, B. Burki, L. Cucurull, and A. Flores. Estimation of Tropospheric Zenith Delay and Gradients over the Madrid Area Using GPS and WVR Data. *Geophys. Res. Lett.*, 26:447–450, 1999.
- H.L. Tolman and J.-H. G.M. Alves. Numerical modeling of wind waves generated by tropical cyclones using moving grids. *Ocean Modelling*, 9:305–323, 2005.
- Y. Wang and C.C. Wu. Current understanding of tropical cyclone structure and intensity changes a review. *Meteorol. Atmos. Phys.*, 87:257–278, 2004. doi: 10.1007/s00703-003-0055-6.
- X. Xu, L. Xie, X. Zhang, and W. Yao. A mathematical model for forecasting tropical cyclone tracks, Nonlinear Analysis. *Real World Applications*, In Press, Corrected Proof, Available online 20 April, 2005.

10. Observations of Infragravity Waves at the Endeavour Ocean Bottom Broadband Seismic Station (KEBB)

David Dolenc (U of Minnesota), Barbara Romanowicz, Paul McGill (MBARI), and William Wilcock (U of Washington)

10.1 Introduction

Infragravity (IG) waves are long-period (20-500 s) ocean surface gravity waves. The pressure fluctuations that they create at the ocean bottom result in seafloor deformation, which is the main source of the long-period noise observed at the ocean-bottom seismic stations. Understanding the properties of the IG waves as well as their coupling to the solid earth is important for the study of the earth's hum and structure using non-seismic sources. Also, modeling of their spatial variability could help with the selection of the most quiet locations for future ocean-bottom seismic deployments.

In our previous work, we found that IG waves are generated in the nearshore region from the shorter-period ocean waves and are observed at the ocean-bottom station KEBB only after they propagate from the shelf into the deeper water and pass over the station. In our recent work (*Dolenc et al.*, 2008), we further studied the IG waves at KEBB to identify the nearshore region where the IG waves are generated.

Station KEBB was installed 247 km offshore Vancouver Island at a water depth of 2376 m in August 2003. It comprised a 3-component broadband seismometer Guralp CMG-1T, a recording, and a battery package. The seismometer was completely buried in the ocean floor sediments and the station was recording the data continuously.

10.2 Results

The analysis of the horizontal velocity ground motions at KEBB throughout the deployment shows that motions are strongly polarized in NW-SE direction (Figure 2.23). Assuming that the IG waves propagated to KEBB as freely propagating waves, we can approximate them as plane waves. In this case we expect the horizontal motions at KEBB to be primarily in the direction of the IG wave propagation. This suggests that the IG waves arrived from the SE direction.

To identify the origin of the IG waves independently of the above observation, we took advantage of their tidal modulation. Tidal modulation of the IG waves has previously been observed at the ocean-bottom seismic stations and can be explained by a mechanism proposed by *Thomson et al.* (2006), in which it results from changes in the beach profile from convex at low-tide to concave at high-tide. To identify the origin of the IG waves we used two parameters. First, the tidal phase changes along the

shore. Second, the distance from the nearshore region to KEBB changes as we move along the shore. Since the freely traveling surface waves are dispersed, the difference between the arrivals of the longer- and shorter-period IG waves at KEBB is a function of distance that IG waves have to travel. We first calculated the predicted traveltime for the IG waves from every buoy to KEBB (Figure 2.24b, solid lines). We then measured the phase delay between the tidal modulation observed at KEBB and tidal phase at individual buoys within different period bins. The comparison with the modeled traveltimes suggests that the IG waves observed at KEBB originated from the nearshore region close to buoy 46041.

10.3 Conclusions

The strong polarization of the horizontal motions at KEBB as well as the analysis of the phase of the tidal modulation observed at KEBB both suggest that IG waves originate from the nearshore region in southern Washington and not from the nearshore regions further to the north that are closer to KEBB. This suggests that long sandy beaches in southern Washington, and not the rocky and rugged coast to the north, play an important role in the IG wave generation.

10.4 Acknowledgements

This work was partially supported by NSF (grant OCE-0648302) as well as BSL funds. The KEBB was deployed as part of the 3-year multidisciplinary prototype NEPTUNE experiment supported by a grant from the W. M. Keck Foundation to the University of Washington. The seismic component of the project was a collaboration between the University of Washington, the University of Oregon, and the Monterey Bay Aquarium Research Institute.

10.5 References

Dolenc, D., B. Romanowicz, P. McGill, and W. Wilcock, Observations of infragravity waves at the ocean-bottom broadband seismic stations Endeavour (KEBB) and Explorer (KXBB), *Geochem., Geophys., Geosys.*, 9, Q05007, doi:10.1029/2008GC001942, 2008.

Thomson, J., S. Elgar, B. Raubenheimer, T. H. C. Herbers, and R. T. Guza, Tidal modulation of infragravity waves via nonlinear energy losses in the surfzone, *Geophys. Res. Lett.*, 33, L05601, doi:10.1029/2005GL025514, 2006.

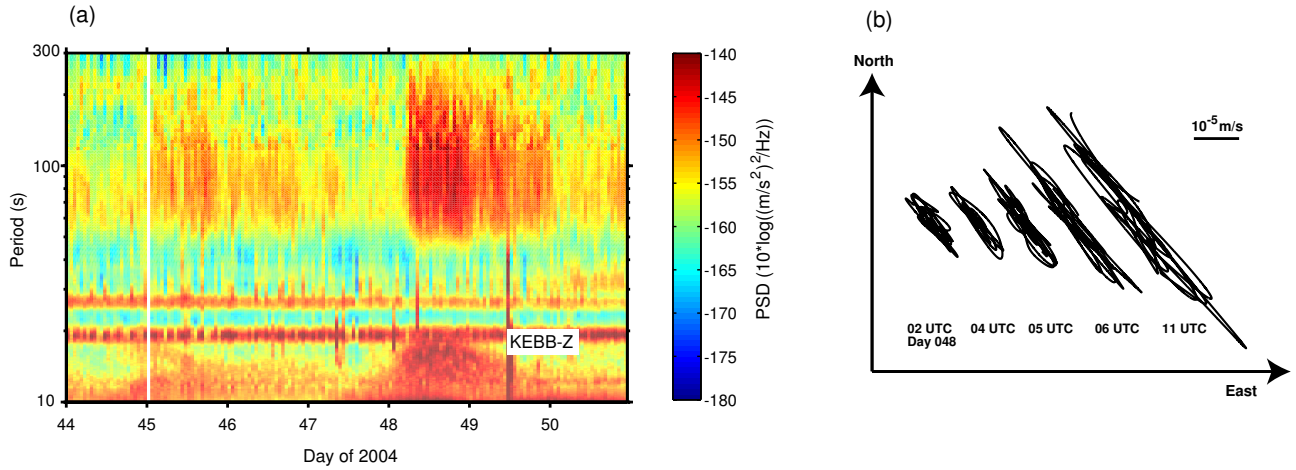


Figure 2.23: (a) Power spectral density for the vertical KEBB component as a function of time and period. A sudden change of the IG peak width and amplitude is observed on day 2004.048 after the storm approaching from the WSW direction reached the coast. (b) Horizontal velocity ground motion at KEBB just before and after the observed change of the IG peak on day 2004.048. The data shown in (b) were filtered in the period band from 40 to 200 s.

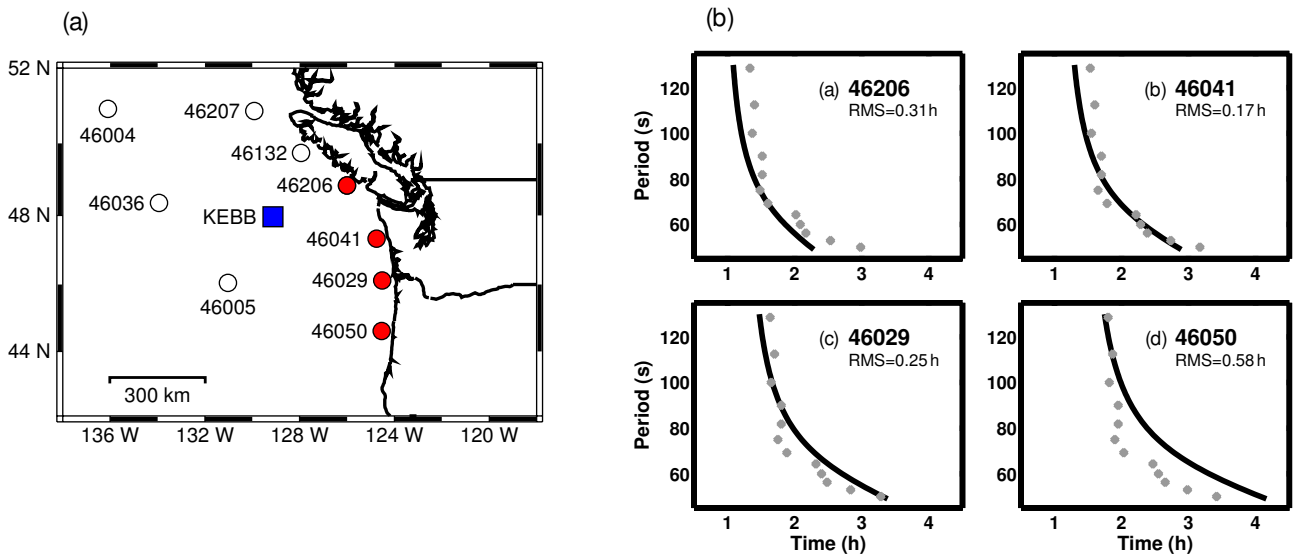


Figure 2.24: (a) Map showing the location of the ocean-bottom station KEBB and ocean buoys. (b) The predicted traveltime for the IG waves from each buoy to KEBB (solid lines) is compared to the measured phase delay between the tidal modulation observed at KEBB and tidal phase at each buoy for different period bins.

11. Western USA mantle structure and its implications for mantle convection processes

Mei Xue and Richard M. Allen

11.1 Introduction

The western USA is on the margin of the North American plate and has complicated and active tectonics. The Juan de Fuca plate, the Pacific plate, and the North American plate meet in this region and form the Mendocino Triple Junction just offshore Northern California. In addition to these primary tectonic objects, many other complicated geologic features are also observed (Figure 2.25). Their corresponding velocity structures have not been well resolved so far and many are still under debate, e.g., the depths the Juan De Fuca plate reaches and the Yellowstone plume originates (*e.g.*, *Humphreys, et al.*, 2000; *Jordan, et al.*, 2004; *Yuan and Dueker*, 2005; *Waite, et al.*, 2006; *Geist and Richards*, 1993).

Here we incorporate the Transportable Array data with all other available networks, resulting in an unprecedented dense distribution of stations in the western USA. This allows us not only to fill the gaps in the resolution of previous studies, but also to see deeper into the mantle, revealing new features. We refer to our seismic velocity models as DNA07-P for P-wave and DNA07-S for S-wave, where DNA07 represents the Dynamic North America model of 2007. Due to the limited space, we only show DNA07-S here, which reveals an extremely heterogeneous mantle structure and provides important clues to mantle convection processes in this tectonically active region.

11.2 Data and Method

The total number of stations we used is 809, and most are from the Transportable Array, with an average station spacing of 70 km (Figure 2.26). The 26 permanent networks are composed of the following: (1) 2 Global Seismograph Networks: (IRIS/IDA and IRIS/USGS); (2) 5 Federal Digital Seismic Networks: the Canadian National Seismograph Network (CNSN), GEOSCOPE (GEO), International Miscellaneous Stations (IMS), Leo Brady Network (LB), and the United States National Seismic Network (USNSN); (3) 14 regional networks: the ANZA Regional Network (ANZA), Berkeley Digital Seismograph Network (BDSN), Cascade Chain Volcano Monitoring (CC), Caltech Regional Seismic Network (CRSN), Montana Regional Seismic Network (MRSN), Northern California Seismic Network (NCSN), Western Great Basin/Eastern Sierra Nevada (WGB/ESN), Princeton Earth Physics Project-Indiana (PEPP), US Bureau of Reclamation Seismic Networks (USBR), Southern California Seismic Network TERRAscope (TERRA), Uni-

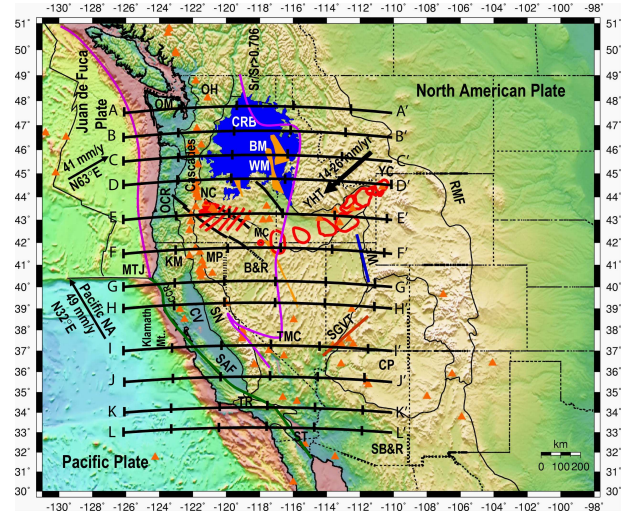


Figure 2.25: Tectonic map for the study region. Labeled features (*Humphreys and Dueker*, 1994b) are OH, Okanogan Highlands; OM, Olympic Mountains; OCR, Oregon Coast Ranges; CCR, California Coast Ranges; KM, Klamath Mountains; MP, Modoc Plateau; MTJ, Mendocino Triple Junction; CV, Central Valley; SN, Sierra Nevada; SAF, San Andreas Fault; TR, Transverse Ranges; ST, Salton Trough; CRB, Columbia River Basalts; BM, Blue Mountains; WM, Wallowa Mountains; NC, Newberry Caldera; MC, McDermitt Caldera; YC, Yellowstone Caldera; YHT, Yellowstone hotspot track along the eastern Snake River Plain; B&R, Basin and Range; SB&R, southern Basin and Range; TMC, Timber Mountain Caldera; SGVT, Saint George Volcanic Trend; CP, Colorado Plateau; WF, Wasatch Front; RMF, Rocky Mountain Caldera. Black lines trending northwest across Oregon indicate right-lateral strike-slip faults. Dike swarms associated with the 17 Ma basaltic outpourings are shown in gold (*Christiansen, et al.*, 2002). Plate motions from HS3-NUVEL 1A are shown as black arrows (*Gripp and Gordon*, 2002). Horizontal black lines indicate the locations of the vertical slices shown in Figure 2.28

versity of Oregon Regional Network (UO), University of Utah Regional Network (UURN), Pacific Northwest Regional Seismic Network (PNSN), and the Yellowstone Wyoming Seismic Network (YWSN); (4) 3 temporary networks: the North Bay Seismic Experiment (NBSE), DELTA LEVY Northern California (DLNC), and the

Wallowa TA 2006-2008 (WTA); and (5) 2 other networks: the Laser Interferometer Gravitational-Wave Experiment (LIGO) and the Network of Autonomously Recording Seismographs (NARS).

We use a technique of teleseismic body wave travel-time tomography and follow the procedure of (Allen, et al., 2002). To correct for source effects and crustal structures, event and station corrections are included in the inversion as a set of free parameters. Rather than leave the station corrections unconstrained, we use corrections calculated from the crustal model of CRUST2.0 as a reference (Bassin, et al., 2000). Station elevations are also corrected. The initial RMS residual is 1.83 sec and is reduced to 0.49 sec after inversion, corresponding to a variance reduction of 73%.

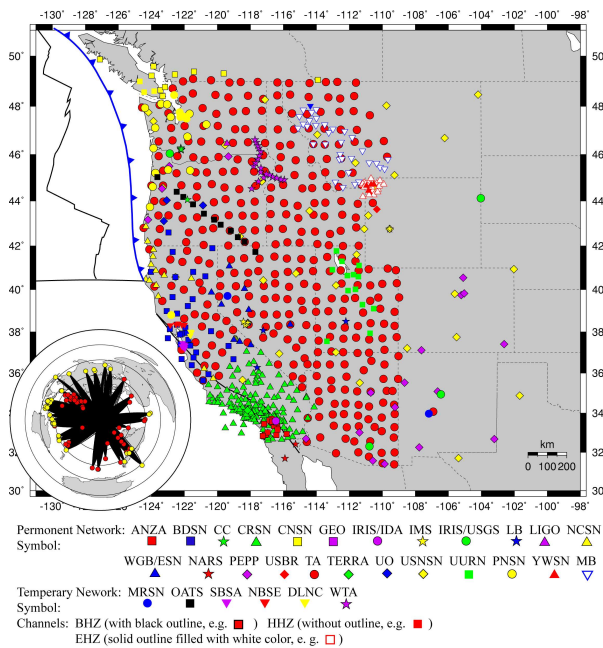


Figure 2.26: The seismic stations used in this study, with a total number of 809. The inset shows the distribution of 88 events and 23233 rays used in the DNA07-S model inversion. The red and yellow dots indicate events providing good direct S phases and SKS phases, respectively.

11.3 Tomographic results and interpretation

Perhaps one of the most striking observations is just how heterogeneous mantle structure is beneath the western USA. Despite this heterogeneity, there is a very strong correspondence with the complicated tectonics of the region. The main features of the velocity models and their implications, shown in Figure 2.27 and Figure 2.28, are listed as follows:

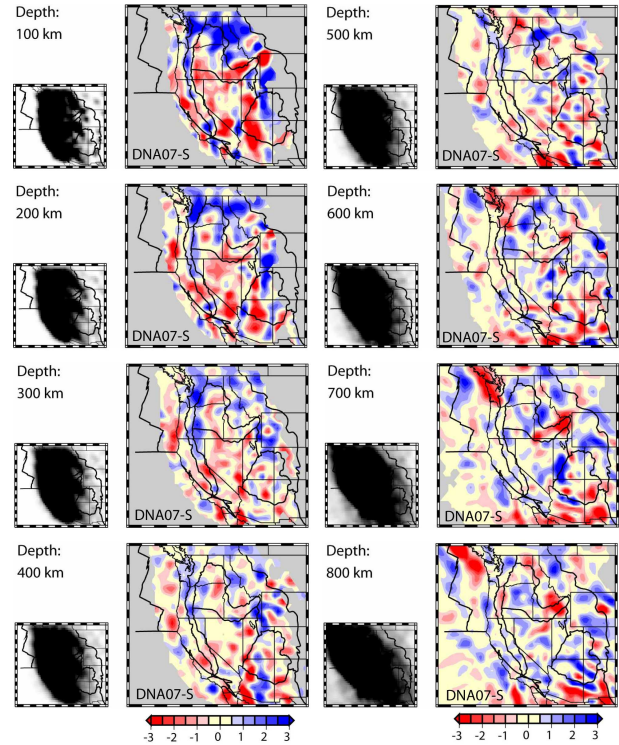


Figure 2.27: Depth slices through the DNA07-S model from 100 km to 800 km depth with an interval of 100 km. Areas with ray hits smaller than 10 are shaded gray. On the right side of each velocity slice is the corresponding ray density plot, where white indicates zero hits and black indicates 100+ hits

- North of the Mendocino Triple Junction:** (1) The Juan de Fuca subduction system stops at ~ 400 km, and is disrupted in Oregon, which we interpret as being due to interaction with the Yellowstone plume head. (2) West of the Cascades the forearc is imaged as a low velocity zone beneath the Coastal Ranges with the strongest velocity anomaly beneath the Olympic Mountains and Northern California. (3) East of the Cascades and above the Juan de Fuca slab, a north-south trending low velocity zone is imaged from southern Washington to northern Nevada. (4) A high velocity region is imaged from central Washington, through northern Oregon, and into Idaho. Beneath Washington the anomalies reach 250 to 300 km depth and deeper, extending to ~ 400 km, beneath the Wallowa Mountains of northeast Oregon. These are likely due to a combination of a cold and thick lithosphere and melt extraction during the eruption of the Columbia River Basalts. (5) The low velocity anomaly beneath Yellowstone dips towards the northwest and stops at 500 km depth. (6) A shallow low velocity zone to ~ 200 km depth lies beneath the Eastern Snake River Plain and does not appear connected to a deeper low velocity zone at the top of the lower mantle. (7) We do not detect a

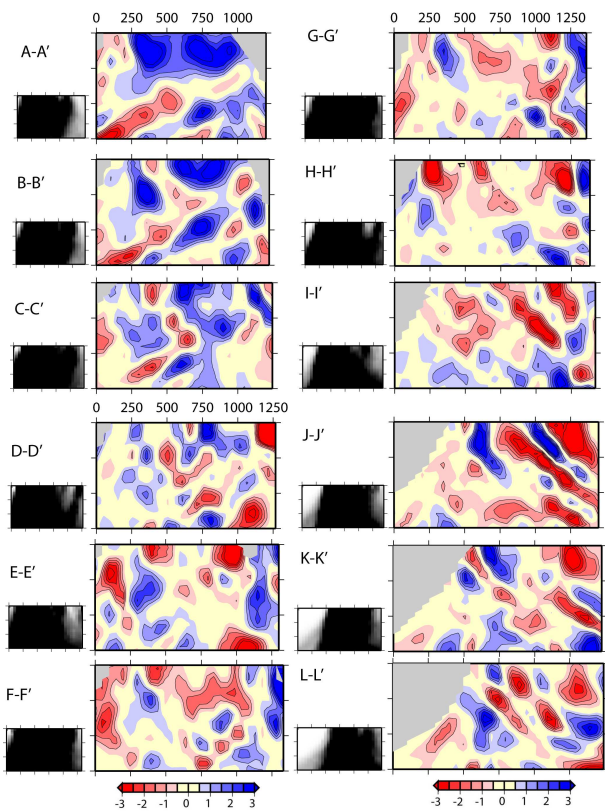


Figure 2.28: Vertical slices through the DNA07-S models. The locations of the cross-sections are shown in Figure 2.25. The color scale is the same as in Figure 2.27

low velocity conduit reaching greater than 500 km depth beneath Yellowstone implying that either (a) any plume was short-lived; or (b) the conduit is < 50 km in diameter and/or the velocity perturbation is less than 1.5% for S and 0.75% for P and therefore unresolved; or (c) there was no deep mantle plume. We prefer the short-lived plume model as it best explains many of the imaged features the Pacific Northwest. (8) There are only shallow low velocity anomalies (< 150 km depth) along the Newberry hotspot track indicate no deep source.

South of the Mendocino Triple Junction: (1) In California, the high velocities of the Pacific plate are imaged abutting against the low velocity North American plate. (2) We image the "slab gap" as low velocity anomalies extending to 400 km depth from the southern end of the Juan de Fuca subduction system to the southern end of the Sierra Nevada. These anomalies are particularly strong just south of the Mendocino Triple Junction. (3) High velocity bodies are imaged beneath the southern tip of the Central Valley/Sierra Nevada and the Transverse Ranges with dips to the east. These may be part of a fossil Farallon subduction system. (4) The Basin and Range is a region of low velocities to a depth of ~ 300 km. In the middle of the Basin and Range, in cen-

tral Nevada, a high velocity feature is imaged extending to 300 km depth. (5) A zone of low velocity is observed to 200 km depth under the Salton Trough consistent with ongoing rifting and small scale convection in the region.

While the upper ~ 400 km of the DNA07 models correlate well with surface tectonics and geologic provinces, the deeper structure (400-750km) is equally complex and not easily explained in terms of either existing geologic or geodynamic models. Further investigation is therefore warranted.

11.4 Acknowledgements

We thank Ana Luz Acevedo-Cabrera for preprocessing some of the data and thank Greg Waite for providing crust correction codes. We thank Doug Dreger, Barbara Romanowicz, and Ved Lekic for beneficial discussions/suggestions. The IRIS DMC provided seismic data. This work was supported by the NSF (EAR-0539987). The figures were produced with SAC and GMT (*Wessel and Smith, 1995*).

11.5 References

- Bassin, C., Laske, G. and Masters, G., The Current Limits of Resolution for Surface Wave Tomography in North America, *EOS Trans AGU*, *81*, F897, 2000.
- Christiansen, R. L., et al., Upper-mantle origin of the Yellowstone hotspot, *Geological Society of America Bulletin*, *114*, 1245-1256, 2002.
- Geist, D. and M. Richards, Origin of the Columbia Plateau and Snake River Plain - Deflection of the Yellowstone Plume, *Geology*, *21*, 789-792, 1993.
- Gripp, A. E. and R. G. Gordon, Young tracks of hotspots and current plate velocities, *Geophysical Journal International*, *150*, 321-361, 2002.
- Hales, T. C., et al., A lithospheric instability origin for Columbia River flood basalts and Willowa Mountains uplift in northeast Oregon, *Nature*, *438*, 842-845, 2005.
- Humphreys, E. D. and K. G. Dueker, Western United-States Upper-Mantle Structure, *Journal of Geophysical Research-Solid Earth*, *99*, 9615-9634, 1994b.
- Humphreys, E. D., et al., Beneath Yellowstone: Evaluating Plume and Noneplume Models Using Teleseismic Images of the Upper Mantle, *GSA Today*, *10*, 1-7, 2000.
- Jordan, B. T., et al., Geochronology of age-progressive volcanism of the Oregon High Lava Plains: Implications for the plume interpretation of Yellowstone, *Journal of Geophysical Research*, *109*, doi:1029/2003JB002776, 2004.
- Waite, G. P., et al., V-pp and Vs structure of the Yellowstone hot spot from teleseismic tomography: Evidence for an upper mantle plume, *Journal of Geophysical Research-Solid Earth*, *111*,, 2006.
- Yuan, H. Y. and K. Dueker, Teleseismic P-wave tomogram of the Yellowstone plume, *Geophysical Research Letters*, *32*, 2005.

12. A simple method for improving crustal corrections in waveform tomography

Vedran Lekic and Barbara Romanowicz

12.1 Introduction

Recordings of surface waves and overtones provide excellent constraints on the structure of the Earth’s crust, upper mantle, and transition zone. This is because they provide good global coverage, and are sensitive to elastic and anelastic structure in both the crust and the mantle. Yet, in order to determine the seismic velocities and anisotropy in the mantle, we must separate the effects of the crust from those due to the sought-after mantle structure. Despite recent improvements in the global mapping of crustal structure (e.g. CRUST2.0: *Bassin et al.*, 2000), the difficulties associated with accurately modeling the effects of the crust seismic on waves mean that these improvements do not automatically translate into better corrections for crustal effects.

Crustal corrections in long period waveform modeling were first applied in a linear fashion, by calculating the effects of perturbations in Mohorovicic depth and surface topography on the (eigen)frequencies of Earth’s free oscillations (*Woodhouse and Dziewonski*, 1984). However, variations in crustal thickness are often large enough to produce non-linear effects on the eigenfrequencies. In order to account for this non-linearity, Montagner and Jobert (1988) proposed a two-step approach in which the eigenfunctions and eigenfrequencies are calculated exactly for a set of tectonic settings (thereby capturing the non-linear effects), while perturbations away from these canonical 1D profiles are handled using linear corrections. This approach has recently been implemented in full-waveform analyses (*Marone and Romanowicz*, 2007). However, when applied to higher modes and to high frequencies, these non-linear crustal corrections can be computationally very expensive.

Here, we present an alternative method for performing crustal corrections. Like the aforescribed methods, we calculate exactly the eigenfunctions and eigenfrequencies for a set of tectonic settings, but instead of using these directly, we solve for scaling coefficients, which, when applied to standard linear crustal corrections, mimic the non-linear effect. The main advantage of this approach is that, once the correction factors have been calculated, it requires no additional computational costs aside from those associated with linear corrections. This allows it to be more easily applied to overtones and to higher frequencies than the standard quasi-non-linear approach.

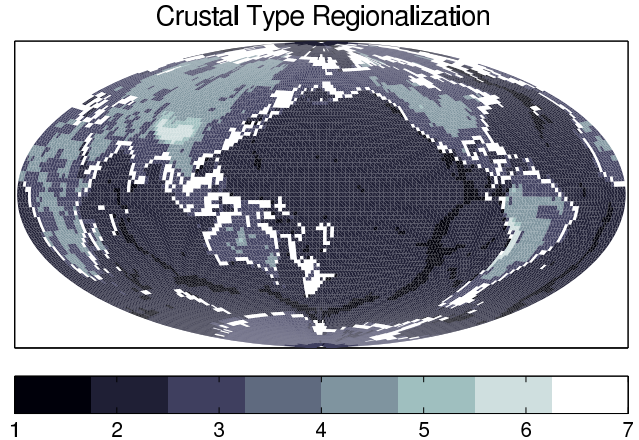


Figure 2.29: Map showing geographical distribution of the 7 crustal types used in this study.

12.2 Modified linear crustal corrections

The effects of lateral heterogeneity, such as variations in crustal velocities and thicknesses, can be approximated by considering how this heterogeneity shifts the frequencies of Earth’s free oscillations, compared to their frequencies in a spherically symmetric reference model such as PREM (*Dziewonski and Anderson*, 1981). For the case relevant to this study, in which only the radii of discontinuities in the Earth are perturbed by δr_d , for an isolated mode branch, local frequency shifts can be calculated in a linear fashion through the use of sensitivity kernels H_k , the expressions for which can be found in *Woodhouse and Dahlen* (1978). Note that these kernels are calculated for the spherically symmetric reference model:

$$\delta\omega_k^2 = \sum_d r_d^2 \delta r_d H_k^d. \quad (2.4)$$

In order to quantify the inadequacy of linear crustal corrections, we divide the Earth’s surface into 7 regions with similar crustal thicknesses and ocean depths. We base this regionalization on Mohorovicic depth from CRUST2.0, with the first 6 regions characterized by Moho depth range of 10-25km, 25-40km, 40-50km, 50-60km, and >60km. The 7th region is introduced to capture the strong effect of a shallow (< 2km) ocean layer that characterizes the continental shelves. Figure 2.29 shows the geographical extent of the 7 regions. For each region, we calculate an average radial profile of density (ρ) and shear (V_S) and compressional (V_P) wave velocity. Armed with a set of radial models that define 7 canoni-

cal crustal types, we proceed to calculate the frequencies ω_k of the fundamental modes for each model. These frequencies are then compared with those of PREM, and frequency shifts between PREM and each of the 7 regional models are calculated as

$$\delta\omega_k^{NL} = \omega_k^{(i)} - \omega_k^{PREM}, \quad (2.5)$$

where the superscript i is an index representing the frequency of mode k in the canonical crustal model i . Since these frequency shifts capture some of the non-linear effects of crustal structure, we identify them with a superscript NL . Figure 2.30 shows the $\delta\omega_k^{NL}$ plotted (solid lines) for spheroidal and toroidal fundamental modes.

We can use the kernels H_k^d that we obtained for the reference spherically symmetric model, in this case PREM, to predict the linearized effects of the canonical crustal structures on the normal mode frequencies. To do this, we only consider the differences in the radii of the discontinuities between each canonical crustal model and PREM, neglecting the differences in crustal velocities and density. This is an often used approximation of the true linear crustal effect, and is appropriate because crustal velocities have been shown to have minimal effect on long period waves (e.g. *Stutzman and Montagner, 1994*). Henceforth, which shall refer to the frequency shifts calculated in this standard, linear fashion as ω_k^{SL} . The dotted lines in Figure 2.30 show the $\delta\omega_k^{SL}$ for each of the canonical crustal structures.

A comparison of the approximate terms $\delta\omega_k^{SL}$ with the $\delta\omega_k^{NL}$ calculated before (and displayed as solid lines) confirms that linear crustal corrections are inadequate, even at long periods. Therefore, we are interested in ways of correcting the $\delta\omega_k^{SL}$ so that they better track $\delta\omega_k^{NL}$. In order to accomplish this task, we are confronted with a crucial choice.

We must decide which term or terms in equation 2.4 to correct. Since H_k^d needs to be calculated for each mode, correcting this term can be computationally expensive. This is what is done in the aforescribed non-linear corrections. Correcting δr_d , on the other hand, does not increase computational costs. The gradual change with frequency of the differences between $\delta\omega_k^{NL}$ and $\delta\omega_k^{SL}$ change gives us hope that modifying δr_d might significantly improve the accuracy of $\delta\omega_k^{SL}$.

We start the procedure by rewriting equation 2.4 in matrix notation, where we only consider N fundamental modes and identify perturbations relating to the Mohorovicic with a subscript m and those pertaining to the surface with t :

$$\begin{pmatrix} \delta\omega_1^{SL} \\ \delta\omega_2^{SL} \\ \vdots \\ \delta\omega_N^{SL} \end{pmatrix} = \begin{pmatrix} r_m H_1^m & r_t H_1^t \\ r_m H_2^m & r_t H_2^t \\ \vdots & \vdots \\ r_m H_N^m & r_t H_N^t \end{pmatrix} \begin{pmatrix} \delta r_m \\ \delta r_t \end{pmatrix} \quad (2.6)$$

We attempt to improve standard linear corrections by

introducing factors $c_{m,t}$, calculated for each canonical crustal type and mode type, that are added to $\delta r_{m,t}$ before being multiplied by the kernel matrix (relabelled \mathbf{H}). Written in vector notation, we seek \mathbf{c} that minimises:

$$\mathbf{w} - \mathbf{H}(\delta\mathbf{r}_{\mathbf{m},\mathbf{t}} + \mathbf{c}_{\mathbf{m},\mathbf{t}}), \quad (2.7)$$

where the vector \mathbf{w} contains the non-linear frequency shifts $\delta\omega_k^{NL}$. The least-squares solution to this minimisation problem is given by:

$$\mathbf{c}_{\mathbf{m},\mathbf{t}} = (\mathbf{H}'\mathbf{H})^{-1}\mathbf{H}'(\mathbf{w} - \mathbf{H}\delta\mathbf{r}_{\mathbf{m},\mathbf{t}}), \quad (2.8)$$

where the apostrophe indicates the transpose.

We could have introduced a multiplicative correction term, instead of the additive one described above. However, solving for such a term becomes unstable when the δr_d 's are small. Given that discontinuity topography is likely to vary both above and below its depth in the reference model, the accompanying zero-crossings of δr_d might have adverse effects.

Because the non-linearity of crustal effects depends strongly on both crustal and mode type, we perform the minimisation in equation 2.8 for spheroidal and toroidal modes separately for each crustal type. Once the set of factors $\mathbf{c}_{\mathbf{m},\mathbf{t}}$ appropriate for a given mode type are obtained, we modify the surface and Mohorovicic topography of CRUST2.0 at each point on the surface by the correction factor appropriate for the relevant crustal type (obtained from Figure 2.29). Therefore, the crustal type and correction factor information is fused into a single file that specifies a modified discontinuity topography for each mode type.

The dashed lines in Figure 2.30 show the frequency shifts predicted by our modified discontinuity radii. Henceforth, we label them $\delta\omega_k^{CL}$. The improvement in fit to $\delta\omega_k^{NL}$ is significant, and good for a large frequency range. When only long period waves ($T > 60s$) are considered, excellent agreement between $\delta\omega_k^{CL}$ and $\delta\omega_k^{NL}$ can be achieved by only correcting the Mohorovicic topography.

12.3 Conclusions

We propose and validate a new method for improving linear crustal corrections. By considering a set of 7 crustal types, we quantify the inadequacy of standard linear corrections at accounting for the effects of the crust on the fundamental mode surface waves. Then, we improve the accuracy of linear corrections by introducing additive factors to the discontinuity topographies. Incorporating an additive correction factor to the discontinuity topography as opposed to the kernels, results in no additional computation costs, compared to standard linear corrections. The correction factors depend on the local crustal type, on the discontinuity considered, and on the reference model used for calculating the sensitivity kernels, as well as mode type.

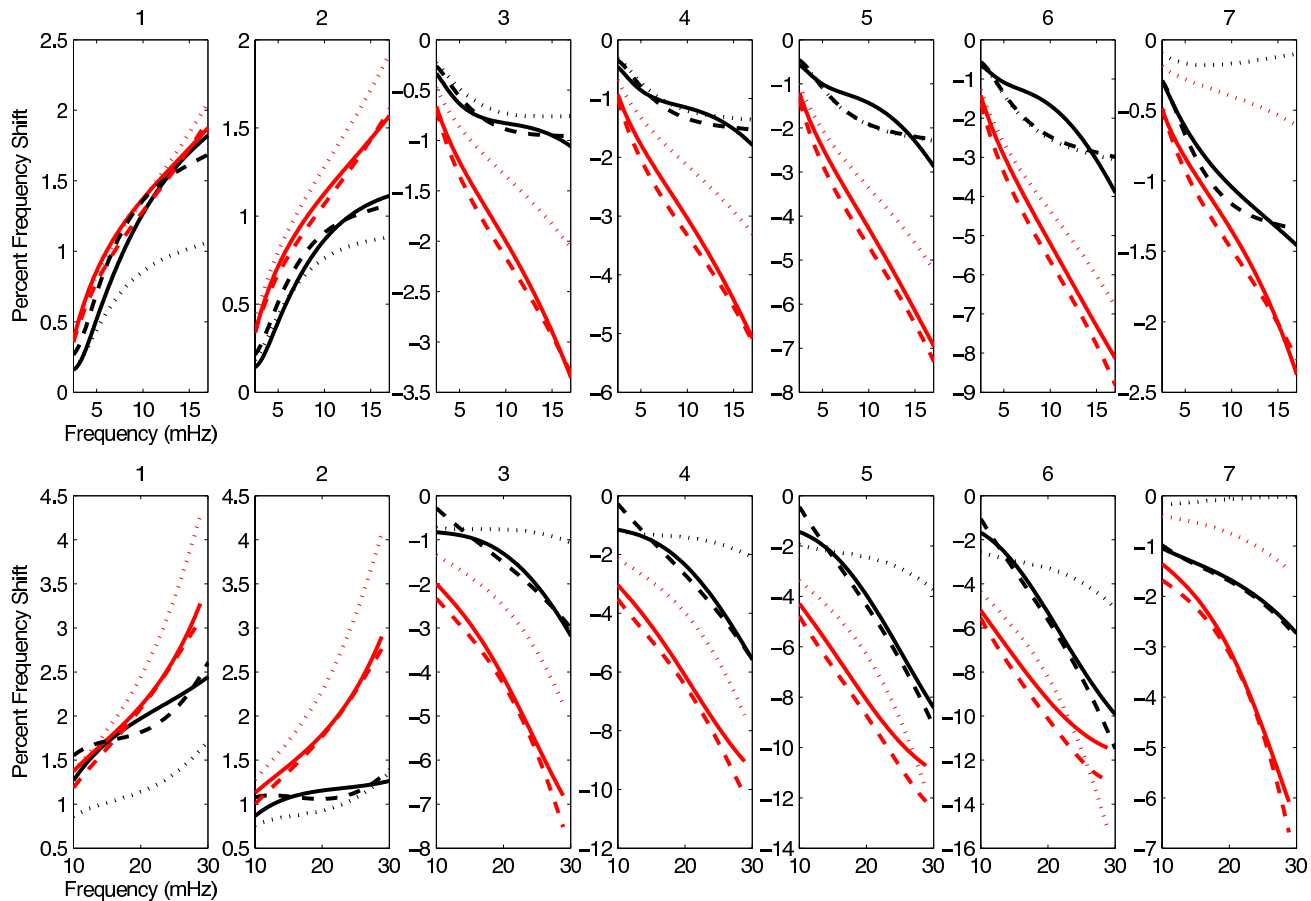


Figure 2.30: Frequency shifts of the fundamental toroidal (grey) and spheroidal (black) modes with respect to PREM anisotropic due to differences in crustal structure between each of the canonical crustal types shown in Figure 2.29. Solid lines denote non-linear corrections ($\delta\omega_k^{NL}$), dotted lines indicate linear corrections ($\delta\omega_k^{SL}$), and the dashed lines indicate linear corrections improved using the method outlined in this paper. Only Mohorovicic corrections are applied in the upper row, while corrections for both surface and Mohorovicic topography are required by the broader frequency range of the bottom row.

12.4 Acknowledgements

This research was supported by National Science Foundation grant NSF/EAR-0308750 and an National Science Foundation Graduate Fellowship held by VL.

12.5 References

Bassin, C., Laske, G. and G. Masters, The Current Limits of Resolution for Surface Wave Tomography in North America. *EOS Trans AGU* 81, F897, 2000.

Dziewonski, A.M. and D.L. Anderson, Preliminary reference Earth model. *Phys. Earth and Planetary Int.*, 25, 297-356, 1981.

Marone, F. and B. Romanowicz, Non-linear crustal corrections in high-resolution regional waveform seismic tomography. *Geophys. J. Int.*, 101 22245-22272, 2007.

Montagner, J.-P. and N. Jobert, Vectorial tomography,

II, Application to the Indian Ocean. *Geophys. J. R. Astron. Soc.* 94, 309-344, 1988.

Stutzmann, E. and J.P. Montagner, Tomography of the transition zone from the inversion of higher-mode surface waves. *Phys. Earth and Planetary Int.*, 86, 99-115, 1994.

Woodhouse, J.H. and F.A., The effect of a general aspherical perturbation on the free oscillations of the earth, *Geophys. J. Int.*, 53, 335-354, 1978.

Woodhouse, J.H. and A.M. Dziewonski, Mapping the upper mantle: three dimensional modeling of Earth structure by inversion of seismic waveforms. *J. Geophys. Res.* 89, 5953-5986, 1984.

13. Effects of water on seismic attenuation

Fabio Cammarano and Barbara Romanowicz

13.1 Introduction

A trace amount of water may be present in the upper mantle and would strongly affect the rheological properties of mantle rocks. Theoretically, this can be explained by the role of hydrogen in enhancing the kinetics of defect motion (for more details, see *Karato, 2006* and *Kohlstedt, 2008*), thus significantly weakening olivine and olivine-rich rocks. A similar behaviour has been predicted for viscoelastic relaxation at seismic frequencies. Geochemical estimates on mid-ocean ridge basalts (MORB) indicate about ~ 0.1 wt% water. Assuming that MORB is the product of ~ 10 -20% melting of peridotite (*Hirth and Kohlstedt, 1996*), the primitive mantle rock should thus have ~ 0.01 wt% H_2O , which is distributed between the individual mineralogical phases according to the partitioning coefficient of each mineral (*Hirth and Kohlstedt, 1996*). In complex tectonic areas and mantle wedges, the amount of water should increase potentially. For the first time, recent laboratory experiments (*Aizawa et al., 2008*) allow the estimation of the effects of water on seismic attenuation. These data, together with previous data on dry olivine (*Faul and Jackson, 2005*), provide values for seismic attenuation to be expected in the upper mantle and can be used to build radial profiles of seismic attenuation based on temperature, grain size and water content, which are able to fit seismic observations (*Cammarano and Romanowicz, 2008*).

13.2 Methods and results

In general, it is reasonable to assume that $Q^{-1} \propto W^{\alpha r}$, where Q^{-1} is attenuation (i.e. $1/Q_S$), W is the water content, α is the frequency dependence, and r is a constant which depends on the process. The value of this constant has been estimated to be between ~ 1 for dislocation mechanisms and ~ 2 in case of grain boundary mechanisms (*Karato, 2006*). To model effects of water, we consider a positive contribution added to the dry attenuation. We define the total attenuation as:

$$Q^{-1} = Q_{dry}^{-1}(P, T, d, \omega) + Q_{wet}^{-1}(P, T, W) \quad (2.9)$$

where Q_{dry}^{-1} is here assumed to be the *Faul and Jackson* value and Q_{wet}^{-1} is the water contribution. The reason for using such an expression is to preserve the knowledge of the T and grain-size dependence of the *Faul and Jackson* (2005) model for dry olivine and to include an empirical correction for water based on recent experimental results at high temperature (*Aizawa et al., 2008*). In spite of large uncertainties, we know

that this correction is always positive (higher attenuation) (see Figure 2.31). The effects on pressure due to the addition of water must also be considered. Therefore,

$$Q_{wet}^{-1}(P, T, W) = A(T, P)W^{\alpha r} \quad (2.10)$$

where α is assumed to be the one from *Faul and Jackson* (i.e. 0.27). The estimated temperature dependence of Q_{wet}^{-1} at low pressure (0.2 GPa) is based on the recent experiments by *Aizawa et al* (2008). We compared the T-dependent attenuation for two natural dunite samples which are characterized by different amounts of water (Figure 2.31a). The “wet” sample probably retains the entire inventory of water (~ 2 wt%) during the high-T experiments, including 0.0187 wt% of molecular water. The “dry” sample, conversely, has lost most of the water and behaves similarly to anhydrous material (Figure 2.31). The effect of water on enhancing viscoelastic relaxation processes has been clearly observed for the first time with these experiments. However, a precise formalism describing the water dependence of solid-state viscoelastic relaxation is hampered because of the structural (and compositional) complexity of the natural samples; the marginal, but not negligible, role of partial melt; and, last but not least, the role of the fluid phase (*Aizawa et al., 2008*). Further studies on simpler material will better characterize the effects of water. At the moment, we can use the available indications to give a rough estimate of the possible effects of water on absolute Q^{-1} . The difference in observed attenuation between the “dry” and “wet” (saturated) samples increases exponentially with temperature, consistent with an enhanced activated process.

Pressure effects can be modeled by multiplying $A(T, P_0)$ with the exponential factor $\exp(PV_W^*/RT)$, where V_W^* is the contribution to activation volume due to water content. Note that P dependence of the dry case is already included in attenuation predicted with *Faul and Jackson’s* model (2005). In the absence of direct constraints on V_W^* , we rely again on information from rheology. If $V_W^* = 1.06 \times 10^{-5} m^3 mol^{-1}$, attenuation for a constant 0.01 wt% water is much larger than for the dry case, both at low and high pressure (Figure 2.31b). With this constant amount of water and the described P-T dependent model, we do not find any attenuation profile that is able to satisfactorily fit the data for any reasonable T and GS profile. For example, assuming isothermal structures for given grain sizes, we found that the best-fit model always has a value > 0.13 for surface wave observations. This is due to the very high values of attenuation

around 100 km. When using a much larger activation volume ($V^* = 2.4 \times 10^{-5} m^3 mol^{-1}$), we find that interpretation in terms of average T does not change much (Cammarano and Romanowicz, 2008). However, only models with $GS \leq 1 \text{ mm}$ and $\langle T \rangle = 1500 \text{ K}$ are able to obtain a similar fit to the dry case. In this case, Q^{-1} values at 100 km (3 GPa) are sensibly lower than before and values at higher P are very similar to the dry case (see Figure 2.31b). We point out that our “water-contribution” to Q^{-1} is independent of grain size, but it does become larger as temperature increases. For example, at a GS of 1 cm and assuming isothermal structure, a $\langle T \rangle = 1600 \text{ K}$ is required for both the dry and the 0.01 wt% wet case. However, values of Q^{-1} for the wet case are significantly higher, especially at shallow depths, and the misfit is not as low as in the dry case. On the other hand, for a given 1 mm GS, seismic observations are best explained with a 1500 K isotherm. In this case, the dry and wet profiles are more similar, as the effect of water on absolute attenuation is less important at lower temperatures.

Finally, we note that when modeling water effects, we should consider the feedback with all the other parameters and not only P and T. We decided to neglect the effect of water on frequency dependence. The Aizawa experiments seem to support such an assumption, not showing any systematic variation of α with water content. In particular, the “wet” sample has a very similar frequency dependence (~ 0.26) to the Faul and Jackson (2005) value. We also assume that there is no feedback between the grain-size dependence and water dependence. In conclusion, water enhances attenuation and trade-offs with temperature. Based on the available constraints, it is likely, however, that water will have a secondary effect on global attenuation measurements. Indeed, Q_S values due solely to a dry mechanism are already low enough compared to what is required seismically in the upper mantle.

13.3 References

Aizawa Y., A. Barnhoorn, U. Faul, J.F. Gerald and I. Jackson, The influence of water on seismic wave attenuation in dunite: an exploratory study, *J. Petrol.*, 49, 841-855, 2008.

Cammarano F. and B. Romanowicz, Radial profiles of seismic attenuation in the upper mantle based on physical models. *GJI*, in press, 2008.

Faul, U.H., and I. Jackson, The seismological signature of temperature and grain size variations in the upper mantle, *Earth Planet. Sci. Lett.*, 234, 119-134, 2005.

Hirth, G. and D. Kohlstedt, Water in the oceanic upper mantle: implications for rheology, melt extraction and evolution of the lithosphere, *Earth Planet. Sci. Lett.*, 144, 93-108, 1996.

Karato, S., Influence of hydrogen-related defects on the

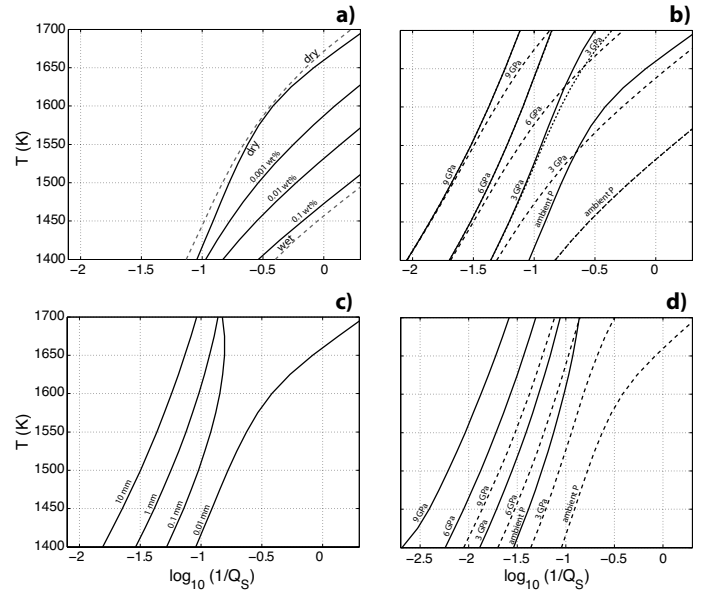


Figure 2.31: Modeled effects of water on P-T dependent attenuation. a) T-dependent attenuation as function of water content at ambient P, period = 150 s and for a GS of 0.01 mm (solid lines). The “wet” and “dry” samples (dashed lines) are, respectively, the attenuation values for two natural dunite samples (1093 and 1066 of Aizawa et al., 2008). The original laboratory data have been interpreted with Burgers model (same formalism as Faul and Jackson, 2005), but in this case, without the (unconstrained) grain size dependence. Both samples have an average grain size around 0.02 mm. b) Modeled T-dependent attenuation at different pressures for the dry case (solid) and with 0.01 wt% water, period = 150 s and grain size of 0.01 mm. Dashed lines are for $V_W^* = 1.06 \times 10^5 m^3 mol^{-1}$. Dotted lines are with $V_W^* = 2.4 \times 10^5 m^3 mol^{-1}$. For comparison, c) and d) show, respectively, variations of Q^{-1} with grain size and effects of pressures for two given grain sizes (solid lines for 1mm and dashed for 0.01mm) computed with the Faul and Jackson model at a period of 150 s.

electrical conductivity and plastic deformation of mantle minerals: A critical review, in *Earth’s Deep Water Cycle*, pp. 113-130, AGU, Washington DC, 2006.

Kohlstedt, D., Constitutive equations, rheological behavior, and viscosity of rocks, *Treatise on Geophysics*, Elsevier, 2008.

14. Analysis of Long-Period Noise at the Farallon Islands Broadband Seismic Station FARB

David Dolenc (U of Minnesota), Robert Uhrhammer, and Barbara Romanowicz

14.1 Introduction

We present a preliminary analysis of the long-period noise observed at the broadband seismic station FARB (Streckeisen STS-2) located on the South Farallon Island, 43 km off the coast of San Francisco, CA. Results from our previous work (Dolenc *et al.*, 2005) showed that long-period noise (20-500 s) observed at the ocean-bottom broadband station MOBB, located offshore Monterey Bay, CA, is mainly due to seafloor deformation under the pressure forcing by infragravity waves (IG; long-period ocean surface gravity waves). A similar type of long-period noise is observed on vertical and both horizontal components of the Farallon Islands station FARB, but not on the nearby mainland stations.

14.2 Results

The long-period noise at FARB is best observed on stormy days when it extends all the way to 1000 s and is even stronger than at MOBB (Figure 2.32). The long-period noise at FARB is stronger on the E-W than on the N-S component, suggesting that it results from the IG waves that propagate from the nearshore region into the deeper ocean.

The comparison of the power spectral density (PSD) at FARB and spectral wave density (SWD) at the nearby buoys for the 2004-2008 period showed that IG waves are generated in the nearshore region close to FARB from the shorter period ocean waves (Dolenc *et al.*, 2008). The energy in the IG wave band at FARB is, as previously observed at MOBB, modulated in phase with tides. The phase of the modulation observed at FARB agrees with the phase of the local tides, suggesting that IG waves observed at FARB are generated locally (Dolenc *et al.*, 2008).

An example of long-period signal observed at FARB and MOBB following the arrival of a dispersed swell on days 2006.037-039 is shown in Figure 2.33. The swell arrived from the NW direction and it can be observed in the 10-30 s period band at FARB and MOBB, as well as the two nearby ocean buoys. The swell signal at the buoys can be seen only when the swell periods fall below ~ 25 s, suggesting that buoys can only record ocean waves with shorter periods. The PSD of the swell signal at MOBB ends once the periods fall below ~ 20 s. Since MOBB is in 1000 m water depth, the 20 s is the short-period cutoff due to hydrodynamic filtering.

The observations at FARB in the 30-500 s period band show that IG waves are generated following the arrival

of the swell. Since the incoming swell is dispersed and has a very narrow period band, it generates IG waves that also appear dispersed. A more detailed analysis reveals that IG waves are generated only once the period of the ocean swell falls below 23 s. The comparison of the incoming swell dispersion and the frequency of the resulting IG waves observed at FARB further shows that nonlinear interaction between a pair of swell components with frequencies f_1 and f_2 results in an infragravity wave with the difference ($f_2 - f_1$) frequency.

Strong horizontal noise observed at FARB in the IG wave band suggests that passing IG waves tilt the island. The swaying of islands and underwater mounds driven by tilting due to infragravity waves could contribute to the recently observed horizontal hum of the Earth (Kurrle and Widmer-Schmidrig, 2008).

14.3 Conclusions

The IG waves are the main source of the long-period noise at FARB. They are generated locally and result from nonlinear interactions between the ocean waves with periods shorter than 23 s. Strong long-period horizontal noise at FARB is probably due to tilting of the island due to passing of IG waves as they propagate away from the shore. The swaying of the islands due to IG waves could contribute to the horizontal hum of the Earth.

14.4 Acknowledgements

The MOBB observatory instrumentation and deployment were supported by funds to the Monterey Bay Aquarium Research Institute from the Lucile and David Packard Foundation, the NSF (grant OCE-9911392), and UC Berkeley funds to the BSL.

14.5 References

Dolenc, D., B. Romanowicz, D. Stakes, P. McGill, and D. Neuhauser, Observations of infragravity waves at the Monterey ocean bottom broadband station (MOBB), *Geochem. Geophys. Geosys.*, 6, Q09002, doi:10.1029/2005GC000988, 2005.

Dolenc, D., R. Uhrhammer, and B. Romanowicz, Analysis of long-period noise at the Farallon Islands broadband seismic station FARB, *Seism. Res. Lett.*, 79, 293, 2008.

Kurrle, D. and R. Widmer-Schmidrig, The horizontal hum of the Earth: A global background of spheroidal and toroidal modes, *Geophys. Res. Lett.*, 35, L06304, 2008.

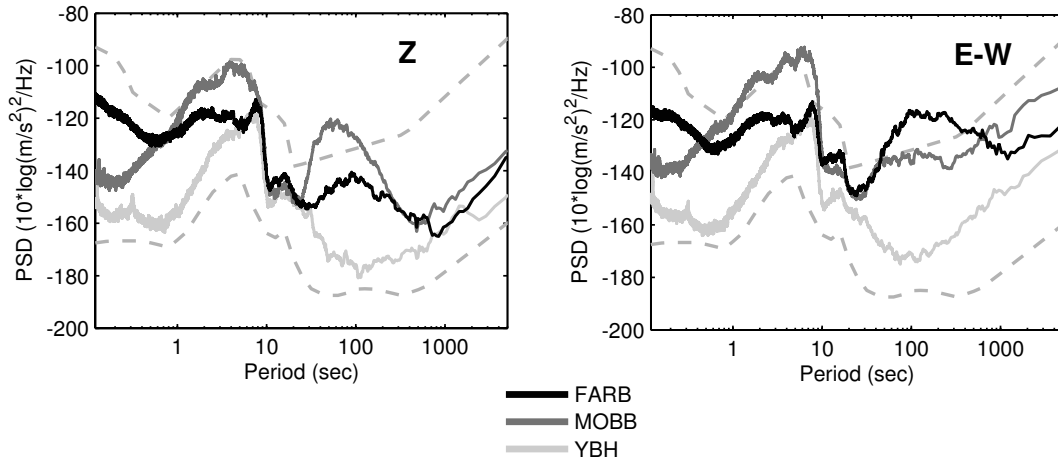


Figure 2.32: Power spectral density (PSD) at FARB, MOBB (Monterey Bay ocean-bottom seismic station), and YBH (560 km north of MOBB, one of the quietest BDSN stations) for the vertical (left) and horizontal (right) component. Results for a stormy day (2005.027) are shown. The USGS high- and low-noise models for land stations are shown as dashed.

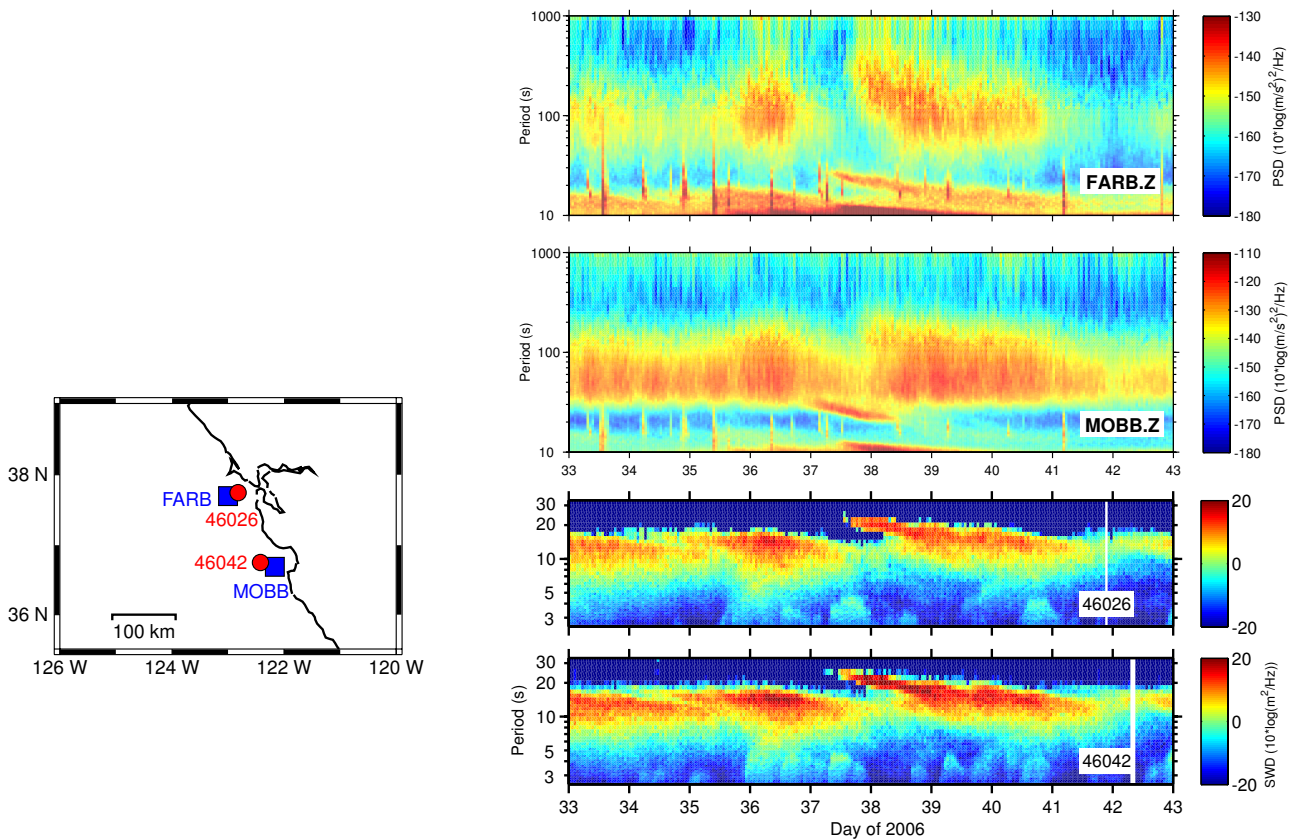


Figure 2.33: PSD for the vertical FARB and MOBB channels as a function of period and time. Bottom panels show spectral wave density (SWD) of the ocean waves calculated at the nearby buoys. The arrival of a dispersed swell on days 037-039 is observed in all 4 panels in the 10-30 s period band. The signal due to infragravity waves generated in the nearshore region following the arrival of a dispersed swell can be seen in the top panel in the 30-500 s period band.

15. Tomography of the Alpine Region from Observations of Seismic Ambient Noise

L. Stehly, B. Fry, M. Campillo, N.M Shapiro, J. Guilbert, L. Boschi and D.Giardini

15.1 Introduction

We use correlations of the ambient seismic noise to study the crust in western Europe (*Shapiro et al, 2005*). Cross correlation of one year of noise recorded at 150 3-component broadband stations yields more than 3000 Rayleigh and Love wave group velocity measurements. These measurements are used to construct Rayleigh and Love group velocity maps of the Alpine region and surrounding area in the 5-80s period band. Finally, we invert the resulting Rayleigh wave group velocity maps to determine the Moho depth.

15.2 Method

We used one year of continuous records from October 2004 to October 2005 from 150 3-component broadband European stations. Our aim is to focus on the Alps, where we have a particularly high density of stations. All the records are processed day by day. First the data are decimated to 1 Hz and corrected for the instrumental response. North and East horizontal components are rotated to get radial and transverse components with respect to the inter-station azimuth. The records are then band-pass filtered and their spectrum whitened between 5 and 150 s. We correlated signals recorded on the components that correspond to Rayleigh and Love waves (ZZ, ZR, RZ, RR, and TT). Correlations of one-day records are stacked.

15.3 Group velocities maps

Rayleigh and Love wave dispersion curves are evaluated from the emerging Green's function using frequency-time analysis (*Levshing et al, 1989, Ritzwoller and Levshin, 1998*) for the 11,000 inter-station paths. For each path, we get eight evaluations of the Rayleigh-wave dispersion curves by considering four components of the correlation tensor (ZZ, RR, RZ and ZR) and both the positive and the negative part of the NCF. Similarly, we get two estimates of the Love-wave dispersion curves from positive and negative parts of TT correlations.

We reject waveforms 1) with S/N (ratio between Rayleigh wave's amplitude and noise variance after it) lower than seven; 2) with group velocities measured on the positive and negative correlation time differing by more than 5 percents, and 3) with paths shorter than two wavelengths at the selected period for the group velocity map. This results in about 3,500 paths over the initial 11,000 inter-station paths at 16 s. We then apply a

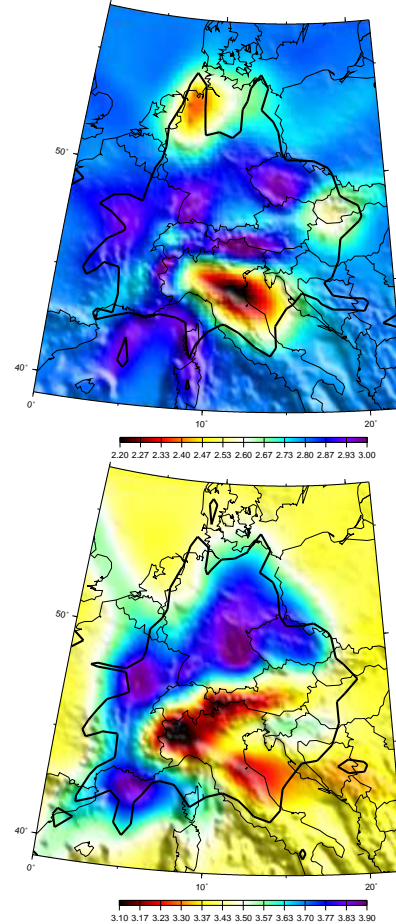


Figure 2.34: Rayleigh group velocity maps at 16s (left) and 35s (right).

tomographic inversion following (*Barmin et al, 2001*) to this data set to obtain group velocity maps on $100 \times 100 = 10,000$ cells of 25×25 km across Europe (Fig. 2.34). Several geological features can be seen on those maps. At 16s, low velocity anomalies are associated with sedimentary basins, such as the Po basin (Northern Italy), the North Sea basin and the Pannonian basin (Slovakia and Hungary). Both Rayleigh and Love waves exhibit smaller values below the molassic sediments (Southern Germany and Austria) than in the surrounding area.

15.4 Moho map of the alpine region

At each cell of our model, we extracted Rayleigh wave dispersion curves from our group velocities map, and

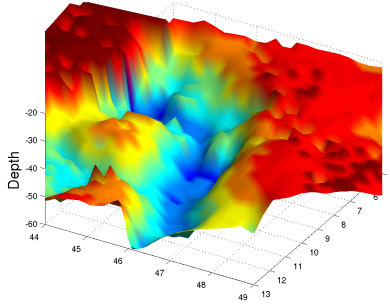


Figure 2.35: 3D view of the Moho depth.

inverted them using a Monte Carlo algorithm in order to determine the depth of the Moho in the Western Alps (Switzerland, Austria, southern Germany). Our results clearly show thickening of the crust below the Alps (Fig2.35). Our map of Moho depth shares striking similarities with the compilation of (Waldhauser *et al*, 1998) in the region where we have a high density of paths. This comparison confirms that seismic noise can be efficiently used to obtain high resolution Love and Rayleigh wave group velocity maps at periods up to 80s and 3D images of the crust and the upper mantle. This method provides spatially continuous seismic velocity distributions on large areas. The resolution of the obtained model depends mostly on the density of stations and is not limited by the uneven distribution of earthquakes. At period less than 10s, the resolution length is not isotropic as the noise is strongly directional.

15.5 References

M. P. Barmin, M. H. Ritzwoller, and A. L. Levshin, A fast and reliable method for surface wave tomography, *Pure and Applied Geophysics*, 158:1351–1375, 2001.

A.L. Levshin, T. B. Yanocskaya, A. V. Lander, B. G. Bukchin, M. P. Barmin, L. I. Ratnikova, and E. N. Its, *Seismic surface waves in a laterally inhomogeneous Earth*, Kluwer Academic Publishers, 1989.

M. Ritzwoller and A. L. Levshin, Eurasian surface wave tomography: group velocities, *Journal of Geophysical Research*, 103(4839-4878):4839, 1998.

N. M. Shapiro, M. Campillo, L. Stehly, and M. H. Ritzwoller, High-resolution surface wave tomography from ambient seismic noise, *Science*, 307:1615–1618, march 2005.

F. Waldhauser, E. Kissling, J. Ansorge, and St. Mueller, Three-dimensional interface modelling with two-dimensional seismic data: the Alpine crust mantle boundary, *Geophysical Journal International*, 135:264–278, 1998.

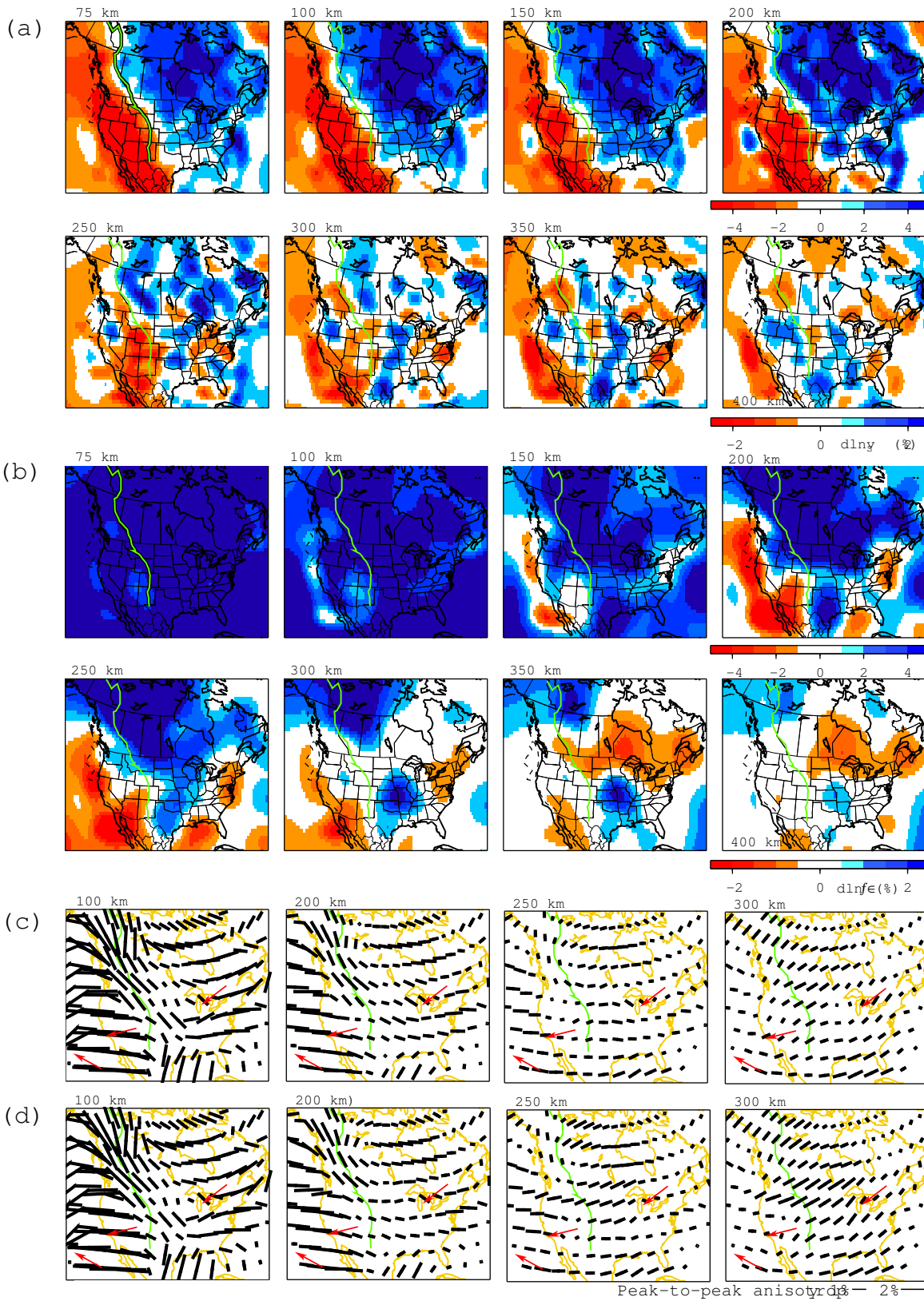


Figure 2.36: Updated isotropic S velocity (a), radial anisotropy (b) and azimuthal anisotropy (c and d) model of the North America upper mantle. Horizontal resolution is 200-km, 400-km, and 400-km for (a), (b) and (c), respectively. (c) and (d) show two azimuthal anisotropy models by surface waveforms only and by surface waveforms and SKS splits, respectively.

16. 3-D Isotropic and Anisotropic S-velocity Structure in North America

Huaiyu Yuan, Federica Marone (Paul Scherrer Institut, Switzerland), Kelly Liu (Univ. of Missouri-Rolla), Steve Gao (Univ. of Missouri-Rolla), and Barbara Romanowicz

16.1 Introduction

The tectonic diversity of the North American continent makes it an ideal region to investigate the structure and dynamics of the continental upper mantle. Investigations of timely geophysical questions, such as the relation to geological age of the variations in the lithospheric thickness, the relation of upper-mantle anisotropy to present day asthenospheric flow and past tectonic events, the nature and strength of the lithosphere/asthenosphere coupling and the driving mechanisms of plate motions, are contingent upon obtaining high-resolution 3-D tomographic models of the isotropic and anisotropic mantle structure of the continent.

In the framework of non-linear asymptotic coupling theory (NACT; *Li and Romanowicz, 1995*), we had developed a regional 3-D tomographic model of the upper mantle beneath North America that includes both isotropic S velocity structure as well as radial and azimuthal anisotropy (*Marone et al., 2007; Marone and Romanowicz, 2007*). This model was constructed from a joint inversion of fundamental and higher mode surface waveforms together with constraints on azimuthal anisotropy derived from SKS splitting measurements. The model showed evidence for the presence of two layers of anisotropy beneath the stable part of the North American continent: a deeper layer with the fast axis direction aligned with the absolute plate motion, and a shallower lithospheric layer with north pointing fast axis likely showing records of past tectonic events. Under the tectonically active western US, where the lithosphere is thin, the direction of tomographically inferred anisotropy is stable with depth and compatible with the absolute plate motion direction.

16.2 Updated 3-D regional tomographic model of North America

Our published regional 3-D tomographic model (*Marone et al., 2007; Marone and Romanowicz, 2007*), however, is based on pre-EarthScope data (before 2003). And since it was our first regional tomographic attempt using NACT, the model has large horizontal resolution, i.e., 400- and 800-km for the isotropic (S) and anisotropic (X) models, respectively. Therefore, during last year, we concentrated mostly on improving the model horizontal resolution by filling the station and event distribution gaps, i.e., adding newly deployed permanent and temporary stations and selectively collecting data from the NE and South back-azimuthal quadrants. Our first set of

updated models, with horizontal resolution of 200- and 400-km for S and X respectively, has been presented at 2007 Fall AGU meeting and 2008 IRIS workshop (Figure 2.36).

Our isotropic and anisotropic shear-wave images are consistent with our published model, but show greater details beneath the cratonic upper mantle, benefitting from the augmented waveform datasets from the US array and newly deployed IRIS PASSCAL and Canadian arrays. For example, our isotropic shear-wave velocity model sees a high velocity curtain at 250-400 km depth range beneath central North America. This feature is also seen by higher resolution P-wave tomography studies (e.g., *Li et al., 2007; Ren et al., 2007; Sigloch et al., 2008*). Our updated radial anisotropy and azimuthal anisotropy images confirm the distinct upper mantle anisotropic domain beneath North America. This continent-wide multiple-layer upper mantle anisotropic domain has also been reported from many studies, e.g., in Rayleigh wave imaging (*Deschamps et al., 2008; Chen et al., 2007; Snyder and Bruneton, 2007*), in multiple-layer anisotropy modeling (*Snyder et al., 2003; Currie et al., 2004; Fox and Sheehan, 2005; Frederiksen et al., 2007; Yuan et al., 2008*), and in receiver functions (*Levin and Park, 1999*). *Deschamps et al. (2008)* speculates that the north trending lithospheric LPO was frozen into the lithosphere during northward drift of the North American plate during Mesozoic times. Some new but minor features appear in the shallow upper mantle in our anisotropic models, correlating well with the surface expression of some past and ongoing NA tectonic events.

16.3 Ongoing research

Currently we are working on improving our 3-D velocity model from the following aspects. First, we are collecting all the EarthScope data and broadband data from the Canadian National Data Center, which will greatly improve our data coverage and hence tomographic resolution, especially beneath the western US. To account for the irregular ray density brought in by the new datasets, we will densify our model spacing in the relevant regions (e.g., beneath western U.S.), which means that higher horizontal resolution (100 km) will be reached in those regions. Second, we are introducing a new 1-D reference model in our inversion. Our previous 1-D reference model, the Preliminary Reference Earth Model (PREM), has a 220-km velocity jump, which is, however, not a ubiquitous feature of the Earth (e.g., *Nettles and*

Dziewonski, 2008; Kustowski et al., 2008). We are switching from the PREM model to a new 1-D reference model developed at UC, Berkeley (Lekic and Cammarano, pers. Comm.) that does not preserve the 220-km discontinuity. Lastly, we are incorporating into our tomographic model the upper mantle discontinuities. These upper mantle discontinuities, serving as either boundaries separating distinct upper mantle anisotropy domains (e.g., the LAB) or isotropic velocity gradients, are better constrained by other techniques, such as teleseismic receiver functions. We are currently exchanging data with research groups at Brown and Rice Universities: the LAB from those groups will be incorporated into our tomographic inversion as a priori constraints; in return, our new 3-D tomographic results will provide a better velocity model for the receiver function depth migration.

16.4 Acknowledgements

We thank the IRIS DMC and Canadian National Data Center for providing the waveform data. Figures are prepared using GMT (Wessel and Smith, 1998). This project is supported by NSF EAR-0643060.

16.5 References

- Chen, C. W., S. Rondenay, D. S. Weeraratne, and D. B. Snyder, New constraints on the upper mantle structure of the Slave craton from Rayleigh wave inversion, *Geophys. Res. Lett.*, *34*, L10301, doi:10.1029/2007GL029535, 2007.
- Currie, C., J. F. Cassidy, R. D. Hyndman, and M. G. Bostock, Shear wave anisotropy beneath the Cascadia subduction zone and western North American craton, *Geophys. J. Int.*, *157*, 341-353, 2004.
- Deschamps, F., S. Lebedev, T. Meier, and J. Trampert, Azimuthal anisotropy of Rayleigh-wave phase velocities in the east-central United States, *Geophys. J. Int.*, *173*, 3, 827-843, 2008.
- Fox, O., and A. F. Sheehan, Shear wave splitting beneath the CDROM transects, in *The Rocky Mountain region—an evolving lithosphere: tectonics, geochemistry, and geophysics*, edited by G. Randy and K. E. Karlstrom, American Geophysical Union, Washington DC, 2005.
- Frederiksen, A. W. et al., Mantle fabric at multiple scales across an Archean-Proterozoic boundary, Grenville Front, Canada, *Phys. Earth and Plan. Int.*, *158*, 2-4, 240-263, 2006.
- Kustowski, B., G. Ekstrom, and A. M. Dziewonski, Anisotropic shear-wave velocity structure of the Earth's mantle: A global model, *J. Geophys. Res.*, *113*, B06306, doi:10.1029/2007JB005169, 2008.
- Li, C., R. D. van der Hilst, E. R. Engdahl, and S. Burdick, A new global model for P wave speed variations in Earth's mantle *Geochem. Geophys. Geosyst.*, *9*, doi:10.1029/2007GC001806, 2008.
- Li, X., and B. Romanowicz, Comparison of global waveform inversions with and without considering cross branch coupling, *Geophys. J. Int.*, *121*, 695-709, 1995.
- Marone, F., Y. Gung, and B. Romanowicz, 3D radial anisotropic structure of the North American upper mantle from inversion of surface waveform data, *Geophys. J. Int.*, doi: 10.1111/j.1365-246X.2007.03456, 2007.
- Marone, F., and B. Romanowicz, The depth distribution of azimuthal anisotropy in the continental upper mantle, *Nature*, *447*, 7141, 198-201, 2007.
- Nettles, M., and A. M. Dziewonski, Radially anisotropic shear-velocity structure of the upper mantle globally and beneath North America, *J. Geophys. Res.*, *113*, B02303, doi:10.1029/2006JB004819, 2008.
- Ren, Y., E. Stutzmann, R. van der Hilst, D., and J. Besse, Understanding seismic heterogeneities in the lower mantle beneath the Americas from seismic tomography and plate tectonic history, *J. Geophys. Res.*, *112*, B01302, doi:10.1029/2005JB004154, 2007.
- Sigloch, K., N. McQuarrie, and G. Nolet, Two-stage subduction history under North America inferred from multiple-frequency tomography, *Nature*, *1*, 7, 458-462, 2008.
- Snyder, D. B., M. G. Bostock, and G. D. Lockhart, Two anisotropic layers in the Slave craton, *Lithos*, *71*, 529-539, 2003.
- Snyder, D. B., and M. Bruneton, Seismic anisotropy of the Slave craton, NW Canada, from joint interpretation of SKS and Rayleigh waves, *Geophys. J. Int.*, *169*, 170-188, 2007.
- Wessel, P., and W. H. F. Smith, New, improved version of the Generic Mapping Tools released, *Eos Trans. AGU*, *79*, 49, 579, 1998.
- Yuan, H. Y., K. Dueker, and D. L. Schutt, Testing five of the simplest upper mantle anisotropic velocity parameterizations using teleseismic S and SKS data from the Billings, Montana PASSCAL array, *J. Geophys. Res.*, *113*, B03304, doi:10.1029/2007JB0050922008.

17. Towards Regional tomography using the Spectral Element Method

Barbara Romanowicz, Aimin Cao, Federica Marone, Mark Panning, Paul Cupillard

17.1 Introduction

We are developing an approach which relies on a cascade of increasingly accurate theoretical approximations for the computation of the seismic wavefield, with the goal to develop a model of regional structure for a sub-region of Southeast Asia (longitude 75 to 150 degrees and latitude 0 to 45 degrees). The selected area is highly heterogeneous, but is well surrounded by earthquake sources and includes high quality broadband digital stations. In previous years, we developed preliminary models based on time domain inversion of long period seismograms, in the framework of normal mode theory: 1) a 3D model based on the Nonlinear Asymptotic Coupling Theory (NACT, *Li and Romanowicz*, 1995), which includes the consideration of 2D kernels in the vertical plane containing source and receiver. This model was developed for a larger region (longitude 30-150 degrees and latitude -10 to 60 degrees), starting from a global 3D model (*Panning and Romanowicz*, 2006); 2) a 3D model based on the NBorn approximation (*Panning et al.*, 2008). This approach combines the 3D Born approximation with the path average approximation (PAVA) and allows us to accurately account for large accumulated phase delays on paths that sample large scale smooth anomalies. The resulting model has a horizontal resolution of about 200 km.

In parallel, a regional version of the Spectral Element Method (SEM) code, in spherical geometry, RegSEM, was completed (*Cupillard*, 2008). This code accepts a non-conformal grid, uses PML (Perfectly-Matched Layers) at the borders of the region, and includes general 3D anisotropy, Moho and surface topography, ocean bathymetry, attenuation, and ellipticity. Because each SEM run (i.e. for one event) is time consuming, we proposed to implement an approach in which the wavefields for several events are computed simultaneously. This approach was introduced by *Capdeville et al.* (2005) and tested on synthetic data at the global scale, but never applied to real data or at a regional scale.

17.2 Towards regional tomography using summed waveforms

In the past year, in collaboration with researchers at the Institut de Physique du Globe in Paris, we completed the codes and procedures that allow us to invert a collection of summed seismograms over the sub-region of Eurasia already considered for the NBORN inversion.

The computation of the forward wavefield using SEM is very accurate, but heavy computationally. It takes 2

hours to compute the wavefield of a single seismic event down to 60 sec (i.e., at long periods) on a modest computer cluster (32 cpu's). To speed up computations and develop the capability of performing many iterations and reaching higher frequencies, we have implemented the approach of *Capdeville et al.* (2005), in which the wavefield corresponding to many events is computed simultaneously. To do so, all the seismic sources considered are shifted in time to a common origin time, and the wavefield generated by this composite source is calculated once. The observed waveforms, at each station, thus consist of the summed observed seismograms for all events, each of them appropriately shifted in time, and are compared to the predicted synthetic wavefield. While these "summed" waveforms do not have a physical meaning, i.e. there are no identifiable seismic phases, they retain sufficient information to allow retrieval of 3D structure, even in the presence of realistic background noise, at least at long wavelengths. This approach can reduce computation time by one to several orders of magnitude, depending on the implementation. *Capdeville et al.* (2005) tested this approach in the framework of global tomography and a synthetic dataset. They showed that, even with realistic noise added to the synthetics, they can retrieve 3D upper mantle structure accurately from a single forward computation involving 50 events observed simultaneously at 150 stations worldwide.

In the adaptation of this method to our regional case, we have proceeded with the RegSEM code (rather than C-SEM) and have relaxed the restriction of all events observed by all stations, replacing the single summation over all events by a series of runs, each of which considers the sum of all events observed at a given station. The number of RegSEM runs is then equal to the number of stations considered in the region, which, in general, is significantly smaller than the number of events. Contrary to the NACT and NBorn cases, for which we collected teleseismic data, RegSEM, as currently implemented, requires sources and receivers to be included in the region of study. We thus collected an entirely new dataset, consisting of 96 events with $6.0 < M_w < 7.0$ observed simultaneously at 6 broadband GSN stations during the time period 1995 to 2007, with an epicentral distance between 5° and 45° .

Figure 2.37 shows the region of study and the ray coverage for our initial summed event experiment. Here, we have relaxed the restriction of teleseismic observations. The epicentral distances range from 5° to 40° . In this case, we cannot perform any comparisons with the NACT or N-Born inversions, for which the theory breaks

down at short distances; however, we can still perform comparisons with inversions obtained using the simpler Path Average (PAVA) approximation.

Figure 2.38 shows an example of comparison between “observed” versus RegSEM computed summed waveforms at station XAN, showing that, at these long periods, the starting model predicts the observed waveforms already quite well.

In order to reduce the computational time in the inverse step of the procedure, we also have opted, at least at this early stage, to compute partial derivatives approximately, using PAVA, in the inversion step of our procedure. We are assuming that, if our starting 3D model (the model derived using N-Born) is sufficiently accurate, these approximate partial derivatives will point us in the right direction and we will at the worst, need to compute a few more iterations to converge to the final model. Eventually, we can implement accurate numerical partial derivatives, whose calculation will also be faster, compared to conventional inversions, due to summation over events.

In order to test the summed event approach, we have first compared the results of an inversion obtained using, on the one hand side, the “summed event” seismograms at the 6 stations considered, and on the other, a “standard” approach, in which we have separately calculated the wavefield using RegSEM for all the events considered, and inverted the corresponding perturbations to the time domain waveforms, as we would do conventionally, using any of our previous inversion methods (PAVA, NACT, N-Born). The only difference in the latter is that now, the forward part of the modelling is computed using RegSEM, rather than mode perturbation theory. The synthetics have been computed down to 60s period, and the observed seismograms have been filtered accordingly. Figure 2.39 shows a comparison of the isotropic models obtained using the conventional approach (single event-station paths) versus the summed approach. The two RegSEM models are very similar indicating that the summed event approach holds promise. A striking feature of the RegSEM models is the fast velocity anomaly south of Korea shallow depth (30 km), which is not present in any of the models developed with asymptotic mode perturbation theory, which shows low velocities throughout the ocean basins at this depth. The fast velocity seen in the RegSEM models is likely an artifact, due to the inaccurate crustal model, which does not incorporate the thick sediments present in that region. Since RegSEM models the crust much more accurately than our usual inversions based on mode perturbation theory, these kind of details start to matter, even at periods as long as this test case.

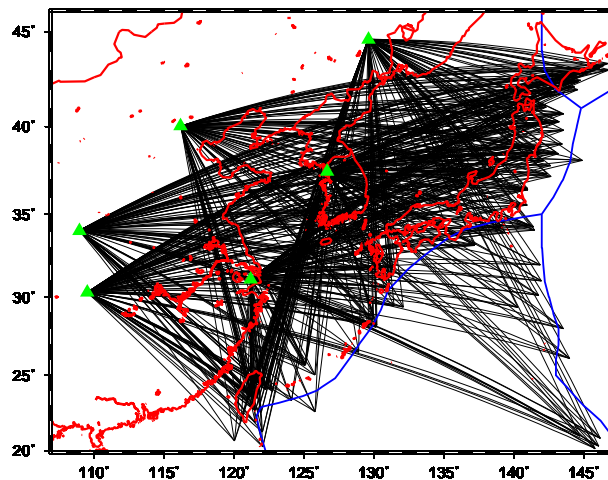


Figure 2.37: Raypath coverage achieved in the “summed seismogram” experiment. The stations are indicated by triangles.

17.3 Acknowledgements

This research was supported by NNSA contract No. DE-FC52-04NA25543 (BAA).

17.4 References

Capdeville, Y., E. Chaljub, J. P. Vilotte, and J. P. Montagner, Coupling the spectral element method with a modal solution for elastic wave propagation in global earth models, *Geophys. J. Int.*, 152, 34-66, 2002.

Capdeville, Y., B. Romanowicz, and Y. Gung, Towards global earth tomography using the spectral element method: a technique based on source stacking, *Geophys. J. Int.*, 162, 541-544, 2005.

Cupillard, P., Simulation par la méthode des éléments spectraux des formes d’onde obtenues par corrélation de bruit sismique, These de Doctorat, Institut de Physique du Globe de Paris, 2008.

Li, X. D. and B. Romanowicz, Comparison of global waveform inversions with and without considering cross branch coupling, *Geophys. J. Int.*, 121, 695-709, 1995.

Panning, M. and B. Romanowicz, A three dimensional radially anisotropic model of shear velocity in the whole mantle, *Geophys. J. Int.*, 167, 361-379, 2006.

Panning, M., Y. Capdeville and B. Romanowicz, Do first order 3D Born finite-frequency kernels improve modeling of surface waveforms?, *Geophys. J. Int.*, in press, 2008.

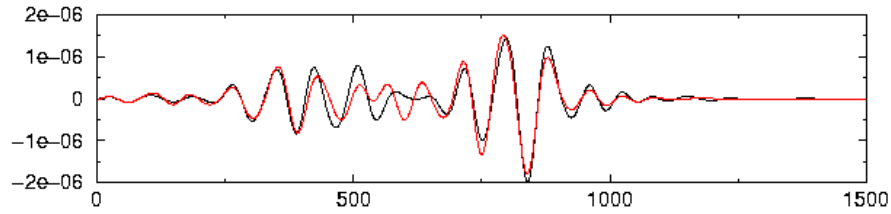


Figure 2.38: Summed seismogram on the vertical component at station XAN. Black: observed trace, red: synthetic trace computed using RegSEM for the starting 3D model (NBORN) shown in Figure 2.37. Both observed and synthetic traces have been filtered with a cut-off period of 60 s.

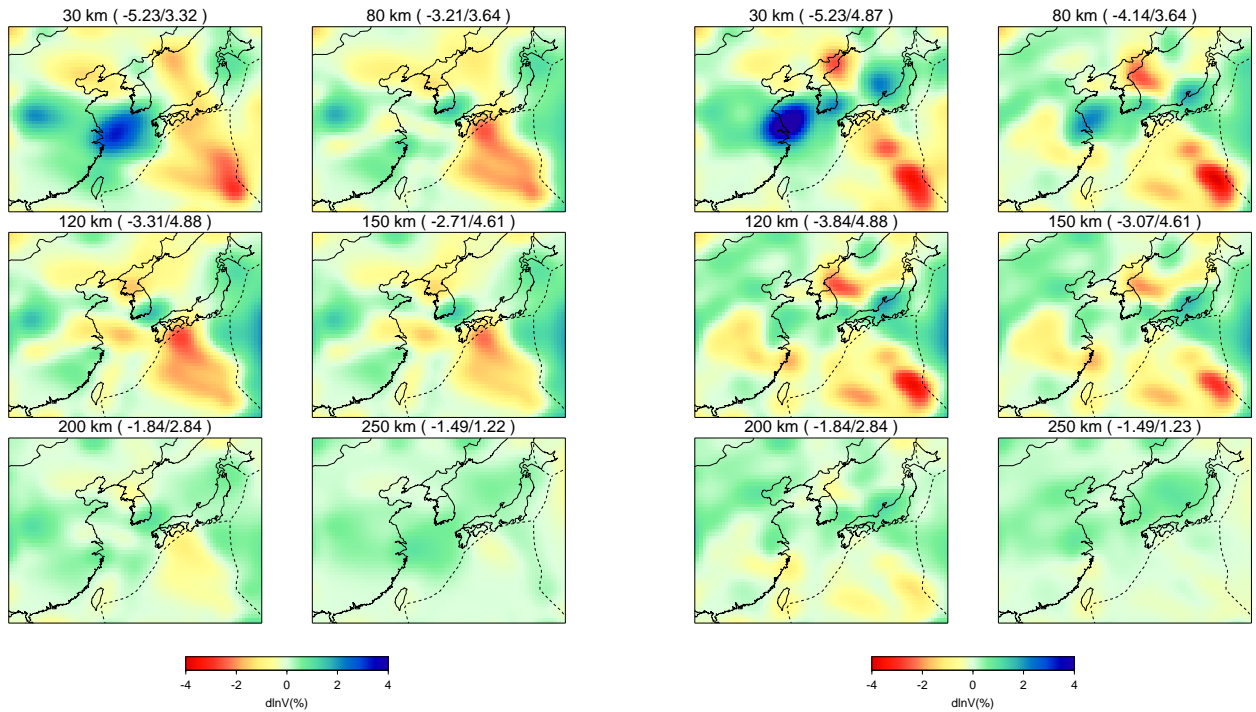


Figure 2.39: Comparison of upper mantle models obtained after one iteration from the starting NBORN model, using waveform data on the path collection shown in Figure 2.38, RegSEM for the forward part of the computation, and PAVA for the calculation of partial derivatives. Left: conventional computation using individual source-station paths. Right: summed-event computation. The models differ in some details, which is not surprising given that only 6 stations have been used.

18. A Brief Review of Observation of the Slichter Mode

Shan Dou, Robert Uhrhammer, Barbara Romanowicz

18.1 Introduction

Slichter mode ${}_1S_1$, which is caused by the translational oscillations of the solid inner core about its equilibrium position at the center of the Earth, was named after the seismologist Louis Slichter when he first claimed the detection of this mode from the data of the Chile Earthquake in 1960. The preliminary estimation of its period made by Louis Slichter proved to be too short (around 86 min). Up to now, the generally-accepted interpretation was that the frequency of the Slichter mode is principally controlled by the density jump between the inner and outer core, and the Archimedean force produced by the fluid outer core. According to theoretical calculations based on perturbation theory, its period is thought to be in the range of 4~8 hours, and it splits into 3 singlets because of the Earth's rotation. As this translational mode can offer important information about the density jump at the ICB (Inner Core Boundary), much effort has been made to detect it. However, there are large uncertainties on its attenuation.

18.2 Review on the Detection of the Slichter Mode

Although the Slichter mode is crucial in determining the density difference across ICB, its detection is very challenging. The difficulties mainly come from the following aspects: (1)The largest displacement of the Slichter mode occurs at great depth (at ICB, see Figure 2.40), and its displacement is strongly attenuated as it goes through the liquid outer core. When the motion finally propagates to the surface of the Earth, it is too weak to be easily observed. For example, for an event as big as the 1960 Chile Earthquake (M_w 9.5), the theoretical estimation of its amplitude on the Earth's surface is only on the order of a nanogal; (2) As the period of the Slichter mode is very long (4~8 hours), it sits in the "subseismic band" (i.e. frequency lower than 0.03mHz) that has very strong background noise; (3)The period of the Slichter mode is also very similar to that of Earth tides, which means that a precise tide model is needed to do the tidal correction. However, as tidal phenomena are quite complicated, it is very difficult to perform this correction with adequate confidence; (4) Q estimates vary by up to several order of magnitude.

Although the exact excitation mechanism of the Slichter mode is still unclear, many detection efforts were undertaken with the assumption that the Slichter mode is continuously excited. Therefore, very long time series can be used to analyze this ultra low frequency signal,

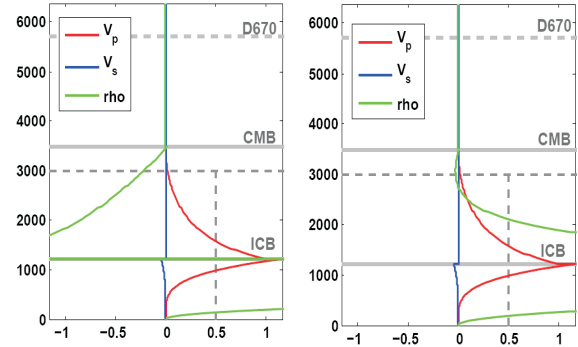


Figure 2.40: normalized theoretical sensitivity kernel of the displacement of ${}_1S_1$. Left: c_{00} ; right: c_{20} (c_{00} and c_{20} are splitting coefficients). We use PREM model here.

but a flat instrumental response (in the frequency domain) is then required to avoid amplifying low frequency noise. Superconducting Gravimeters (SGs) can therefore facilitate the observation, as their response in subseismic bands is very flat and stable. Over 20 SGs are installed around the world, which make it possible to extract of global signals by stacking.

The first claim of the detection of the Slichter mode after L. Slichter was made by *Smylie et al* (1992, Science). They used 4 long records from SGs in Europe: Brussels (1982~1986), Brussels (1987~1989), Bad Homburg (1986~1988), Strasbourg (1987~1991). They found out three singlets with periods of 3.5820 ± 0.0008 , 3.7677 ± 0.0006 , and 4.015 ± 0.001 hours, as well as Q values of 116, 141 and 115, respectively. These frequency values are very close to the theoretical calculation based on 2nd order perturbation theory (*Dahlen and Sailor*, 1979). However, this promising observation was put into doubt when *Hinderer et al.* (1995) failed to reproduce *Smylie's* (1992) results. They used 2 simultaneous records at SG stations in Canada and France, and analyzed both the product spectra and cross-spectra. The whole process was optimal, as the phase information could be kept in this way, but the results were disappointing, as they could not detect the triplet in their spectra. They argued that cross-spectra should enhance coherent signals and interpreted the null observation as indicating that the triplet of *Smylie* was not the Slichter mode. Later, *Ochi et al.* (2000) designed a method to utilize the spatial dependency of the 3 singlets to obtain a better spectral estimate for each of them. They used 6 records from different observatories but covering the same time period. They

then confirmed the presence of the triplet using an analysis based on product spectra. The mode showed up in the data from both Europe and outside of Europe, but with slightly different periods for both groups of stations. Again, *Rosat et al.* (2006) failed to reproduce *Ochi's* result. *Rosat et al.* developed a detection method based on predictions from theoretical models, which were similar to those used by *Ochi et al.* (2000), and applied it to one-year datasets of SG gravity using product spectra, but they were unable to observe the triplet. Many other attempts to observe the Slichter mode through SG data are not listed above, but they all have negative answers. Detection of this special mode is still a challenge.

18.3 Motivation and Future Work

SG data has played a key role in the study of the Slichter mode, but the disadvantages of these instruments are also apparent: (1) Since SGs are very expensive and have strict site condition requirements, they are still sparsely distributed globally; (2) Only a small part of SG data are directly shared on-line, and these data always have a delay of 6 months; (3) the SG data format is not used by seismologists, and the transfer function is not always known. Compared with SGs, STS-1 seismometers also have good performance at ultra low frequency (Figure 2.40), and the wide distribution of the STS-1 makes it an optimal instrument for global stacking. Also, the transfer functions are well known. For these reasons, we are trying to develop a standard procedure to search for the Slichter mode using STS-1 data.

18.4 Acknowledgements

We thank David Dolenc, David Crossley, and Ichiro Kawasaki for their help on tidal corrections.

18.5 References

Dahlen, F.A. and Sailor, R.V., Rotational and elliptical splitting of the free oscillations of the Earth, *Geophys. J. R. Astron. Soc.* 58, 609-623, 1979.

Hinderer, J., Crossley, D., and Jensen, O., A search for the Slichter triplet in superconducting gravimeter data, *Phys. Earth Plan. Int.*, 90, 183-195, 1995.

Ochi Y., K. Fujita, I. Niki, H. Nishimura, N. Izumi, A. Sunahara, S. Naruo, T. Kawamura, M. Fukao, H. Shiraga, H. Takabe, K. Mima, S. Nakai, I. Uschmann, R. Butzbach, E. Forster, N. Courtier, B. Ducarme J. Goodkind, J. Hinderer, Y. Imanishi, N. Seama, H. Sun, J. Merriam, B. Bengert, D.E. Smylie D.E, Global superconducting gravimeter observations and the search for the translational modes of the inner core, *Phys. Earth and Plan. Int.*, 117, 3-20, 2000.

Rosat, S., Y. Rogister, D. Crossley, J. Hinderer, A search for the Slichter triplet with superconducting

gravimeters: impact of the density jump at the inner core boundary, *J. Geodynam.*, 41, 296-306, 2006.

Slichter, L.B., The fundamental free mode of the Earth's inner core, *Science*, 47, 186-190, 1961.

Smylie, D.E., The inner core translational triplet and the density near Earth's center, *Science*, 255, 1678-1682, 1992.

Smylie, D.E., J. Hinderer, B. Richter and B. Ducarme, The product spectra of gravity and barometric pressure in Europe, *Phys. Earth and Plan. Int.*, 80, 135-157, 1993.

19. What Does a Waveform Obtained by Correlation of a Diffuse Anisotropic Wavefield Contain?

Paul Cupillard and Yann Capdeville (IPG Paris)

19.1 Introduction

Recent developments have shown that the Green's function between two distant seismometers can emerge from the cross-correlation of several days of seismic noise recorded at the seismometers (*Shapiro and Campillo, 2004*). This provides new data that are greatly interesting for seismologists because they enable us to get information about the Earth structure in aseismic regions. Group-speeds on inter-station paths are now widely measured, and numerous high-resolution tomographic images appeared in the last three years.

Many theoretical developments tried to explain the phenomenon. All the theories only take into account the case of uniformly distributed noise sources. Now, an anisotropic flux as well as the absence of equipartition has to be considered to fully understand the limitations of the method. Indeed, noise consistently observed in seismic records mainly comes from the oceans (*Longuet-Higgins, 1950*), so that its distribution at the surface of the Earth clearly is nonhomogeneous. Here we study the effect of such a distribution by computing correlations of numerically generated seismic noise in an attenuating sphere.

19.2 Uniform Noise Sources Distribution

First, we compute synthetic noise to mimick the continuous oscillations that are consistently observed in seismic records. To create that noise, we randomly position three hundred sources on the Earth's surface. For each spatial component of each source, we generate a 24-hour time signal with random phase and flat spectrum filtered between 2 and 13 mHz. Using normal-modes summation in the Preliminary Reference Earth Model (*Dziewon-ski and Anderson, 1981*), the effect of all the sources is computed at three stations A, B and C located on the equator at longitude 0° , 20° and 70° respectively (Figure 2.41). Correlations between vertical components of displacement received at the stations are then calculated. That is the result of what we call a "realization". We perform 12,640 realizations (the total number of sources is then 3,792,000) and we stack all of them. Three different cases are studied, corresponding to different processes applied to the noise records : we distinguish raw noise (nothing is done), 1-bit noise (meaning that we completely disregard the amplitude) and whitened noise (meaning that the spectral amplitudes of each record are set to 1 in the chosen frequency band).

With the normal-modes summation method, the

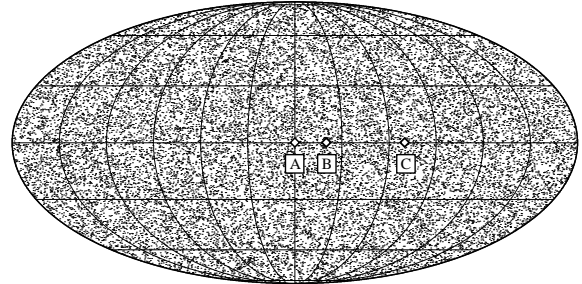


Figure 2.41: Location of receivers A, B and C (top). Station B (resp. C) is 20° (resp. 70°) away from A. Tiny dot pixels indicate location of 24,000 noise sources coming from 80 realizations of our numerical experiment.

Green's tensors between A and B and between A and C can be easily calculated. Figure 2.42 shows the comparison between Green's functions and the derivatives of our synthetic correlations with and without power spectral density correction. We note that the waveform and relative amplitudes between the signal from A and B and the signal from A and C are conserved for each kind of noise processing. This means that information about geometrical as well as intrinsic attenuation is contained in correlations whatever the technique we use to process the noise recordings. Travel times have been preferentially considered so far on seismic noise correlations, but the use of amplitude is now more and more questioned, and the result we present here is essential in this perspective. Nevertheless, it is in disagreement with the experimental result from *Larose et al (2007)* who recover the geometrical spreading with raw data but lose it with 1-bit or whitened noise. We don't have an explanation for this difference yet.

19.3 Non-Uniform Noise Sources Distribution

Here we perform the same experiment, except that noise sources are now confined in a 50° -radius disk at the surface of the sphere. We study cross-correlations from different azimuths by using records from 24 stations located in two circles around a central station A (Figure 2.43).

As in the previous section, we compare Green's functions and the derivatives of our correlations. Two azimuths are studied : 90° (i.e. stations 12 and 24, see Figure 2.44) and 30° (i.e. stations 2 and 14, see Figure 2.45). For the first azimuth, results are very similar to

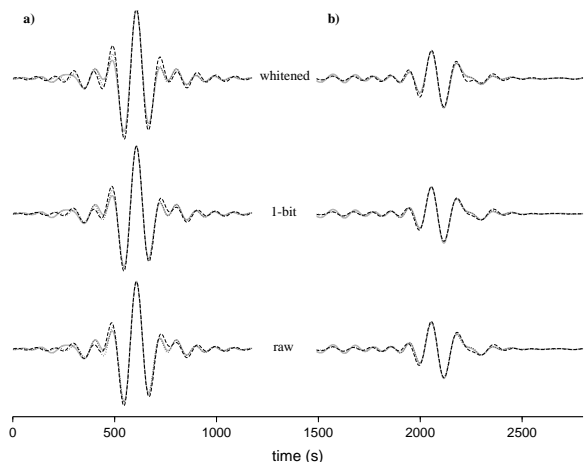


Figure 2.42: **a)** Comparison, for each kind of process applied to the noise records (raw, 1-bit normalization and whitening), between the A-B Green's function (gray lines) and the derivatives of our synthetic cross-correlations with (dotted lines) and without (dashed lines) power spectral density (PSD) correction. **b)** Same as a) for stations A and C. The PSD correction improves the waveform fits.

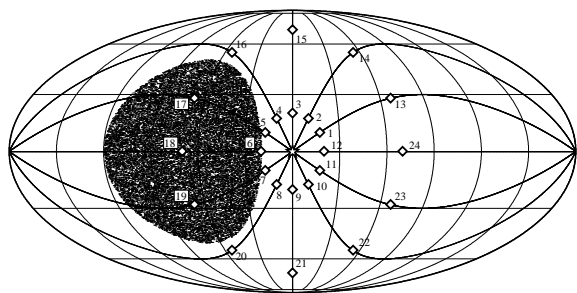


Figure 2.43: Location of the central station A (star) and the other receivers (numbered from 1 to 24). Stations 1 to 12 (resp. 13 to 24) are 20° (resp. 70°) far from A and spaced by an angle of 30° , defining twelve azimuths. Great circles that link the stations to the centre A are plotted to highlight the different azimuths. In addition, tiny dots indicate location of 24,000 noise sources coming from 80 realizations of our numerical experiment.

those observed in the uniformly distributed noise sources case: the power spectral density correction improves the waveforms' fit, overtones are not well excited, and attenuation is retrieved for the three different noise-processing procedures. Results from azimuth 30° are very different. An important phase shift between the Green's functions and the correlations is observed, both for station 2 and station 14. This is because the emergence of the signal is only due to sources far from the vicinity of the great circle, and contribution of such sources provides incorrect travel times.

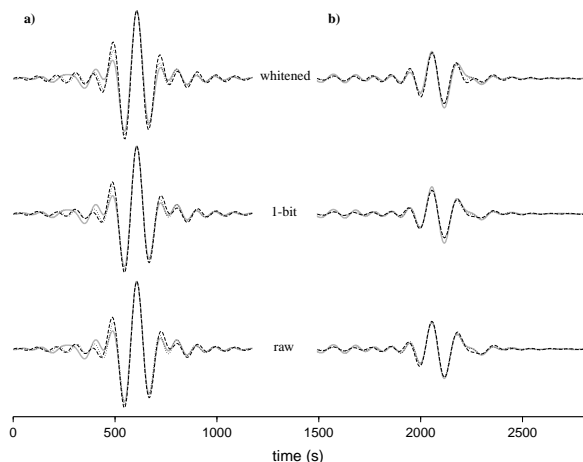


Figure 2.44: **a)** Comparison between the derivative of the correlation of station 12 by A and the corresponding Green's function. Gray lines correspond to the Green's function, whereas dotted and dashed lines are correlations respectively with and without power spectral density correction. **b)** Same as a) for station 24.

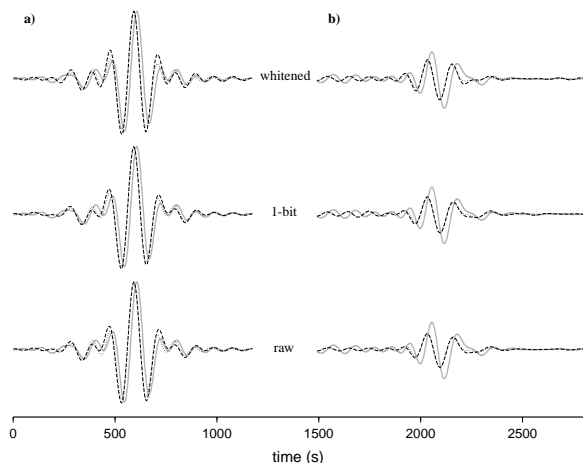


Figure 2.45: Same as Figure 2.44 for stations 2 and 14.

19.4 References

- Dziewonski, A.M. and D.L. Anderson, Preliminary Reference Earth model, *Phys. Earth Planet. Inter.*, 25, 297-356, 1981.
- Longuet-Higgins, M.S., A theory on the origin of microseisms, *Philo Trans. R. Soc. Lond. A.*, 243, 1-35, 1950.
- Shapiro, N.M. and M. Campillo, Emergence of broadband Rayleigh waves from correlation of the ambient seismic noise, *Geophys. Res. Lett.*, 31, L07614, 2004.

20. Measurement and implications of frequency dependence of attenuation

Vedran Lekic, Jan Matas, Mark Panning (Princeton University), and Barbara Romanowicz

20.1 Introduction

As they propagate through the Earth, seismic waves experience energy loss, which is summarized by $q = -\Delta E/2\pi E_{max}$, where ΔE is the internal energy lost by a seismic wave in one cycle. Attenuation is high and nearly constant within a certain frequency band and rapidly falls off with frequency away from this band. The frequency dependence of q can be described using a power law, $q \propto \omega^\alpha$, with a model-dependent α that is usually thought to be smaller than 0.5 within the absorption band.

Though seismological efforts at constraining globally-averaged α within the absorption band have benefited from numerous measurements of surface wave or normal mode attenuation (see <http://mahi.ucsd.edu/Gabi/rem.html>), the determination of α has been confounded by the fact that oscillations at different frequencies can have very different depth sensitivities to elastic and anelastic properties of the earth. As a result of this trade-off between frequency and depth effects, radial variations of attenuation can obscure the α signal. The only studies attempting to obtain α within the absorption band have found α ranging from 0.1 to 0.3 while emphasizing the lack of resolution on the deduced values. More recent studies have relied upon analysis of body waves to argue for values of α in the 0.1-0.4 range (see *Romanowicz and Mitchell, 2007*). However, these studies were restricted to frequencies higher than 40mHz and were of regional extent, leaving unanswered the question of the average mantle α .

In light of these difficulties, seismic studies routinely assume that, within the seismic band, α cannot be resolved and thus implicitly rely on the frequency-independent attenuation model of *Kanamori and Anderson (1977)*. We re-examine the model’s applicability to the mantle using a new method based on the standard analysis of *Backus and Gilbert (1970)* that allows us to separate the effects of the radial q profile from those due to frequency dependence of q as described by α .

20.2 Method

We can relate a mode attenuation measurement q to material properties within the Earth via sensitivity (Fréchet) kernels K_μ and K_κ :

$$q = \frac{2}{\omega} \int_0^R dr \kappa_0 q_\kappa K_\kappa + \mu_0 q_\mu K_\mu, \quad (2.11)$$

where R is the radius of the Earth, κ_0 and μ_0 are the reference radial profiles of bulk and shear moduli, and q_κ and q_μ are values of radial bulk and shear attenuation.

The sensitivity kernels of fundamental modes with similar frequencies are very similar, implying that the q datasets are highly redundant. We seek to exploit this redundancy and divide modes into a low and high frequency bin, denoted by superscript l and h , respectively. Each linear combination of Fréchet kernels of modes in each bin defines a new “hyperkernel”:

$$\mathbf{H}_{\mu,\kappa}^{\text{low}} = \sum_{l=1}^{N_l} \gamma^l \mathbf{K}_{\mu,\kappa}^l \quad \text{and} \quad \mathbf{H}_{\mu,\kappa}^{\text{high}} = \sum_{h=1}^{N_h} \gamma^h \mathbf{K}_{\mu,\kappa}^h, \quad (2.12)$$

where N_l and N_h are the number of modes in each bin, and the subscripts μ, κ denote that the kernels refer to either shear or bulk attenuation.

Each particular choice of γ^l and γ^h will yield hyperkernels with different depth sensitivities. Therefore, by requiring that γ^l and γ^h yield hyperkernels with identical sensitivities to the radial attenuation profile, it is possible to remove the trade-off between depth and frequency dependence of attenuation measurements. Since we focus on the effective α in the mantle, we require the hyperkernels to be zero outside the mantle while providing maximally uniform sensitivity in the mantle. In order to eliminate the contribution from poorly-constrained mantle bulk attenuation, we seek hyperkernels that are insensitive to q_κ .

To each hyperkernel corresponds a q value, which is a weighted average of the q measurements of its constituent normal modes:

$$q^{\text{low}} = \sum_{l=1}^{N_l} \gamma^l q^l \quad \text{and} \quad q^{\text{high}} = \sum_{h=1}^{N_h} \gamma^h q^h. \quad (2.13)$$

Since the two hyperkernels have identical sensitivity to radial attenuation structure but differing frequency content, differences in q^{low} and q^{high} can be attributed to frequency dependence of attenuation. These effects of frequency dependence can be accounted for by projecting the individual mode q ’s to a reference value q_0 using:

$$q_{0i} = q_i \left(\frac{\omega_i}{\omega_0} \right)^\alpha. \quad (2.14)$$

In the absence of systematic measurement error, q^{low} and q^{high} will be reconciled at the reference frequency for the value of α that corresponds to the effective α of the mantle.

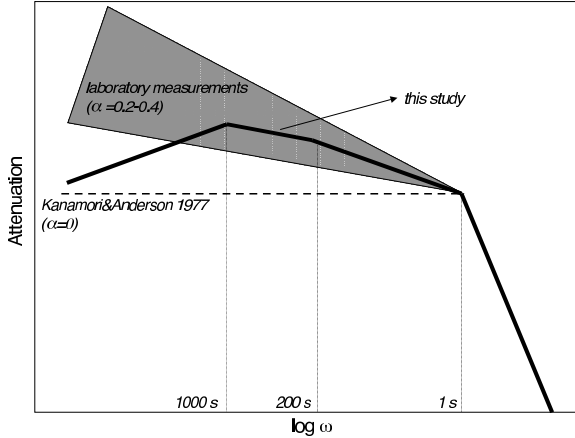


Figure 2.46: Preferred model of frequency dependence of attenuation within the absorption band. α is approximately 0.3 at periods shorter than 200 s, decreasing to 0.1 in the period range 300-800s, and becoming negative (-0.4) at periods longer than 1000s.

20.3 Results

After validating our method on a synthetic dataset, we apply it to existing attenuation measurements of free oscillations and surface waves spanning the period range 3200s-50s. We observe that effective α is likely to be frequency dependent. Specifically, α is negative at periods longer than 1000s and positive and increasing at shorter periods (see Figure 2.46). This conclusion runs against both the assumption of frequency-independent attenuation often used in seismology, and the constant, positive α model suggested by laboratory studies (*Jackson et al.*, 2005). A frequency-dependent effective α is nevertheless physically plausible. This is because the effective α that one would obtain by analyzing the normal-mode and surface-wave attenuation measurements is the result of an interplay of the *actual* α associated with the material at a given depth and the position of the absorption band. This interplay can give rise to a negative effective α as long as the actual α is negative at long periods at some depths. Furthermore, our preferred model of frequency dependence of attenuation is consistent with earlier studies that have relied upon body waves and have focused on higher frequencies (see Figure 2.46).

A non-zero value of α carries important implications for the construction of radial profiles of attenuation. Efforts at determining the radial profile of attenuation in the Earth have routinely assumed that attenuation is frequency independent. The resulting models have, therefore, mapped the signal of frequency-dependence of q into its depth profile.

Relating lateral variations of attenuation in terms of temperature requires knowing α , since when α is zero, $\delta q/\delta T$ is a constant, whereas when α is positive,

$\delta q/\delta T$ is exponentially dependent on temperature (*Minster and Anderson*, 1981). Recent studies of lateral attenuation variations rely on data with periods shorter than ~ 300 s (e.g. *Gung and Romanowicz*, 2004), at which periods our preferred model suggests that $\alpha \sim 0.3$. This value implies an exponential temperature dependence of attenuation, and justifies the interpretation of lateral attenuation variations in terms of temperature variations.

Intrinsic attenuation causes dispersion of seismic velocities, which must be corrected when datasets with different frequency content are used to simultaneously constrain Earth structure. Both the values of α and of q significantly affect the magnitude of the dispersion correction. For an α value of 0.3, the assumption of frequency-independent attenuation will result in 25% error for a frequency ratio of 10 and a 50% error for a frequency ratio of 100.

Finally, the precise knowledge of seismic velocity, its dispersion and associated attenuation is important for meaningful comparisons with other geophysical observables, such as the geoid. Future work should thus be aimed at improving the precision of q measurements and the development of radial q profiles that properly account for the frequency dependence of q .

20.4 Acknowledgements

This project was supported by NSF grants EAR-0336951 and EAR-0738284, NSF fellowship held by VL, and by the French CNRS-SEDIT program.

20.5 References

- Backus, G.E. and J.F. Gilbert, Uniqueness in the inversion of inaccurate gross earth data, *Phil. Trans. R. Soc. London*, 266, 123-192, 1970.
- Gung, Y. and B. Romanowicz, Q tomography of the upper mantle using three-component waveforms, *Geophys. J. Int.*, 157, 813-830, 2004.
- Jackson, I., S. Webb, L. Weston, and D. Boness, Frequency dependence of elastic wave speeds at high temperature: a direct experimental demonstration, *Phys. Earth Planet. Inter.*, 148, 85-96, 2005.
- Kanamori, H. and D.L. Anderson, Importance of physical dispersion in surface wave and free oscillation problems: Review, *Rev. Geophys. Space Phys.*, 15, 105-112, 1977.
- Minster, B. and D.L. Anderson, A model of dislocation-controlled rheology for the mantle, *Phil. Trans. R. Soc. Lond.*, 299, 319-356, 1981.
- Romanowicz, B. and B. Mitchell, Deep Earth structure: Q of the Earth from crust to core. In: Schubert, G. (Ed.), *Treatise on Geophysics*, 1, Elsevier, 731-774, 2007.

21. Nonvolcanic tremor activity modified by the 2003 M6.5 San Simeon and 2004 M6.5 Parkfield, California earthquakes

Aur lie Guilhem and Robert M. Nadeau

21.1 Introduction

The discovery of nonvolcanic tremors in the region of Parkfield-Cholame, California, along the major San Andreas Fault in 2005 (Nadeau and Dolenc, 2005) has given a new perspective on these deep long-duration, high-frequency (1 to 15 Hz) events, which previously were only observed along subduction zones. The California tremors show many of the characteristics of the subduction zone events in terms of depth, frequency range, waveform, and the absence of apparent P- and S- waves. However they are shorter in duration, up to tens of minutes versus hours to days. The presence in the area of five seismic networks, including the High Resolution Seismic Network (HRSN), gives the opportunity to detect and locate the tremor activity over a large region, even for distances approaching 200 km between stations. We performed a multi-year tremor analysis between August 2001 and 2008 and we studied the influence of the 2003 M6.5 San Simeon and 2004 M6.0 Parkfield earthquakes, the largest events to occur in the study region and time period, on the Parkfield-Cholame tremor activity.

21.2 Tremor activity history

Using a similar cross-correlation detection method described by Obara (2002), we searched nearly 7 years of tremor activity starting in August 2001 and found more than 1,700 nonvolcanic tremors with a cumulative duration of more than 9,700 minutes (Figure 2.47). The locations of the tremors based on envelope cross-correlation and station pair time delay indicate that the events are mainly distributed across the San Andreas Fault over a 10-15 km wide area offset to the west of the fault, beneath Cholame, California (Figure 2.48).

The tremor catalog was compared to the catalog of M0+ earthquakes of the same 40-by-40 km region centered on the town of Cholame, California. Analysis of the spatio-temporal evolution of the tremors during the seven years of the study (Figure 2.47) revealed a strong correlation between tremor rates and occurrences of the two largest earthquakes of the region: the 2003 M6.5 San Simeon and 2004 M6.0 Parkfield earthquakes. Following the two mainshocks, the tremor activity increased in a step-like pattern, which was persistent over several months. We noticed a step change of a factor of ~ 3 in the cumulative duration of tremor activity over 3 months before and after the San Simeon earthquake. Similar observations followed the Parkfield earthquake, when the cumulative duration of the events increased by a factor

of ~ 5 between 3 months before and 3 months after the mainshock. The tremor rate changes were not the consequence of the emergence of longer tremors but of a larger tremor frequency. On the other hand, no increase in the number of small earthquakes was observed above the tremors after San Simeon (70 km away from tremor zone). However, we noticed a very strong increase (34 times the background level) in the seismicity rate after Parkfield. The close proximity of the Parkfield earthquake rupture to the tremor region explains the large number of aftershocks following it (Figure 2.48).

Also, following the two events, an aftershock-like decay of the tremor activity was observed. Aftershock sequences are evidence of re-adjustments of the stress field in the seismogenic zone after a mainshock. The similar pattern in the tremor activity at Parkfield suggests that tremor activity is also related to stress change.

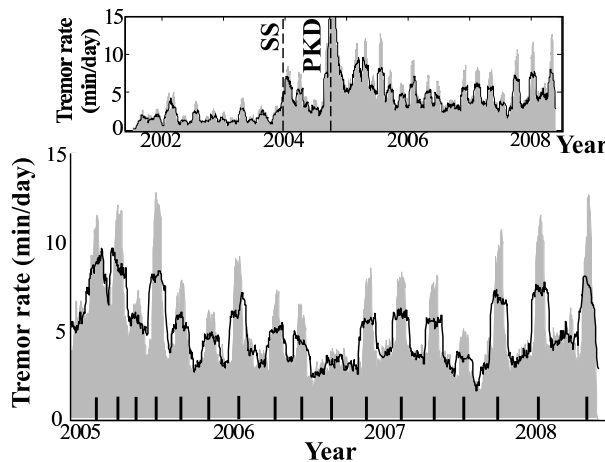


Figure 2.47: Tremor activity between August 2001 and May 2008. The gray filled areas show the tremor catalog smoothed over 20 days, and the black line shows the catalog smoothed over 40 days. The dashed lines (upper) indicate the time of the San Simeon (SS) and Parkfield (PKD) earthquakes. The tick marks (lower) show the episodes of tremors observed after Parkfield.

21.3 Tremors sensitive to small stress changes

We performed Coulomb stress changes maps (Figure 2.48) of the two strong earthquakes using the finite-source models computed by Rolandone *et al.* (2005) and Kim and Dreger (2008), respectively, to define the rupture

zone. The Coulomb failure stress changes were calculated for vertical planes parallel to the San Andreas Fault (140° strike, 90° dip and 180° rake) at the median depth of the tremors (i.e. 20 km) and at seismogenic depth (i.e. 8 km) in two 10-by-10 km boxes centered on the tremor and earthquake locations. Following the 2003 San Simeon earthquake, the static Coulomb stress increased up to 12.5 kPa (0.125 bars) at 20 km depth and to 14.4 kPa (0.144 bars) at the earthquake depth. Typical stress changes inducing triggered earthquakes are on the order of 1 to 10 bars (Stein, 2004). The small stress changes observed following San Simeon at 8 km depth explained the absence of earthquake activation. However, changes in the tremor rate for less than 12.5 kPa stress increase suggest that tremors can be stimulated by significant low static stress changes. Following Parkfield, up to a 5-bar increase was transmitted into the earthquake zone, in agreement with the change recorded in the seismicity. At 20 km depth, the static stress changes were also higher after Parkfield than after San Simeon, with a maximum of 22.9 kPa (0.229 bars). Evidences of correlation between higher tremor rate and higher stress changes suggest that tremors are sensitive to stress variations at depth and that the degree of tremor activation is related to the level of stress change experienced.

21.4 Episodes of tremors

Since the Parkfield earthquake (from 2005 to present), the tremor activity has remained elevated relative to before the San Simeon earthquake (Figure 2.47). We have also noticed the emergence of quasi-periodic bursts of tremor activity starting after the end of the Parkfield afterslip sequence in 2005. The episodes of tremors were not observed before the San Simeon earthquake or before the Parkfield earthquake. They consist of periods of higher frequency of the number of tremors and not of an increase in the duration (or amplitude) of individual tremors. The analysis of the episodes shows that the recurrence time between episodes is lengthening from ~ 50 days in 2005 to ~ 110 days in 2008, following a linear trend. The episodes of tremors may suggest very small stress variations in the deeper part of the crust generated after the Parkfield earthquake and possibly related to postseismic transients in depth.

21.5 Conclusions

The origin of the nonvolcanic tremors has yet to be determined; however several hypotheses have been proposed: fluid migration from subduction processes, shear coupling at depth, hydraulic fracturing, tidal stress variations, and small dynamic stress changes (less than 43 kPa) during the passage of teleseism surface waves. Our results suggest that tremors react to even smaller static stress change (less than 23 kPa) transmitted in their generating region. The degree of tremor activation also re-

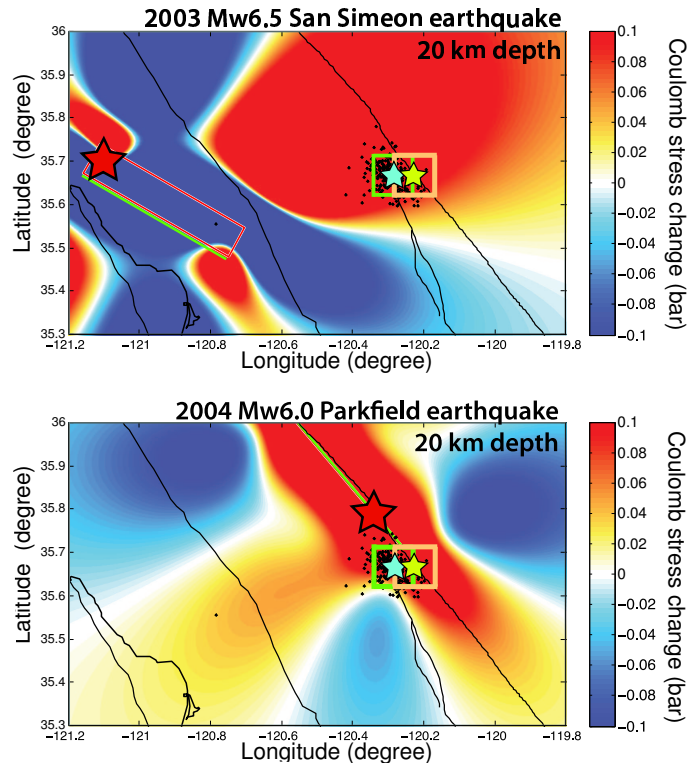


Figure 2.48: Coulomb stress maps for the San Simeon and Parkfield earthquakes at 20 km depth. The red star shows the mainshock location. The blue and yellow stars indicate the centroid of tremor and earthquake locations, respectively in their corresponding 10 km by 10 km boxes. The black dots show the tremor locations for 2006-2007.

flects the level of stress change at depth, and elevated activity persists well beyond the aftershock decay period following Parkfield.

21.6 References

- Kim, A., and D. S. Dreger (2008), Rupture Process of the 2004 Parkfield Earthquake from Near-Fault Seismic Waveform and Geodetic Records, *J. Geophys. Res.*, *113*, B07308, doi:10.1029/2007JB005115.
- Nadeau, R. M., and D. Dolenc (2005), Nonvolcanic Tremors Beneath the San Andreas Fault, *Science*, *307*, 389.
- Obara, K. (2002), Nonvolcanic Deep Tremor Associated with Subduction in Southwest Japan, *Science*, *296*, 1,679-1,681.
- Rolandone, F., D. Dreger, M. Murray, and R. Burgmann (2006), Coseismic Slip Distribution of the 2003 Mw6.6 San Simeon Earthquake, California, Determined from GPS Measurements and Seismic Waveform Data, *Geophys. Res. Lett.*, *33*, L16315.
- Stein, R. S. (2004), Tidal Triggering Caught in the Act, *Science*, *305*, 1,248-1,249.

22. Mapping the Rupture of the M_w 5.4 Alum Rock Earthquake

Margaret Hellweg, Angela Chung, Douglas Dreger, Ahyi Kim and Jack Boatwright (USGS Menlo Park)

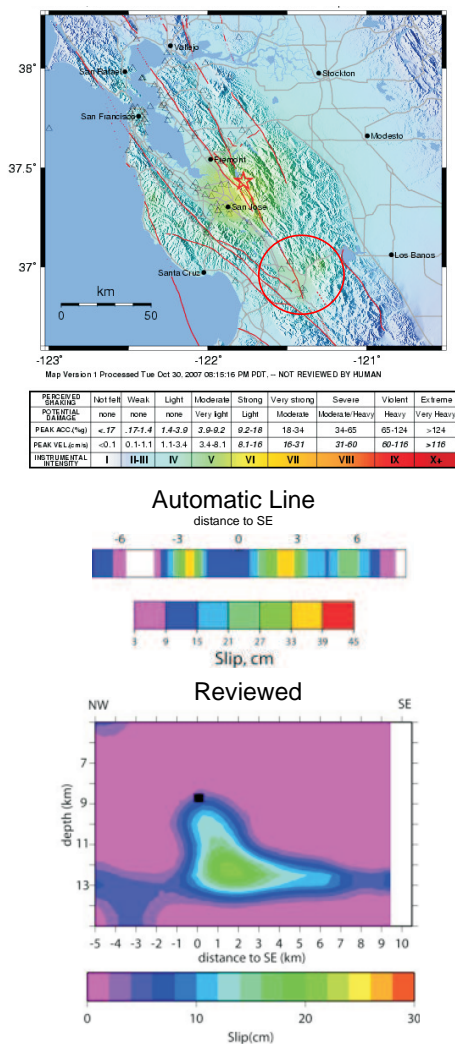


Figure 2.49: The Alum Rock earthquake occurred along the Calaveras Fault near San Jose. The ShakeMap (top) shows the epicenter and the levels of shaking experienced. Note the strong shaking (intensity VI) to the southeast of the epicenter (red circle). Both the finite fault line source and plane show rupture to the southeast from the epicenter (bottom).

22.1 Introduction

The largest earthquake since Loma Prieta shook the San Francisco Bay Area at 08:04 pm PDT on October 30, 2007 (03:04 UTC on October 31, 2007, Figure 2.49 (top)). It had M_w 5.4. Since the Loma Prieta earthquake, instrumentation in the region has improved, with many more digital stations, including short period, strong mo-

tion and broadband sensors. The Shakemap in Figure 2.49 (top) shows the epicenter (star), the level of shaking (colors) and the locations of stations which recorded the event (triangles). The automated finite-source solution (Figure 2.49 (upper part of bottom image)), based on the automated moment tensor, was available 9 minutes after the event. We present here finite fault results from the Alum Rock earthquake.

22.2 Moment Tensor Solution

The reviewed moment tensor solution (Figure 2.50) for the Alum Rock earthquake is 98 percent double couple, with strike, dip and rake of 323° , 87° and -180° . This motion is consistent with slip along the Calaveras Fault.

22.3 Finite Fault Solution

The automated finite-source line solution (Figure 2.49 (upper part of bottom image)) shows that slip was largely located southeast of the epicenter. Although the magnitude of this event is at the lower threshold for finite-source analysis given broadband waveforms and the simplified models used to compute Greens functions, the preliminary line-source as well as felt reports and peak ground motion maps indicate that the rupture had strong southeast directivity. One hour after the event, refined results in the plane source indicated that the fault ruptured southeast from the hypocenter.

Two line-source rupture models were produced by the automatic processing. For this event with small M_w 5.4, it was not possible to distinguish between the two conjugate line-source models. However, for the line-source parallel with the Calaveras fault (model shown in Figure 2.49 (upper part of bottom image)), most of the slip lies to the southeast of the epicenter.

We have prepared a finite-source inversion of the Alum Rock earthquake using the method of Dreger and Kaverina (2000). The model has a single fault plane and constant rake, rupture velocity, and rise time. The data and synthetics were bandpass filtered between 0.01 and 0.3 Hz. The lowpass filtering reduces the importance of high frequency arrivals and was performed because of concerns of the adequacy of the velocity model and Greens functions. Despite this restrictive filtering, southeast rupture is a dominant feature of the slip model (Figure 2.49, lower part of bottom image). Initially, the event ruptures downward and extends about 5 km to the southeast of the epicenter. This extent of rupture is echoed in the locations of the aftershocks, which occurred exclusively to the southeast of the epicenter, and within 5 km. The

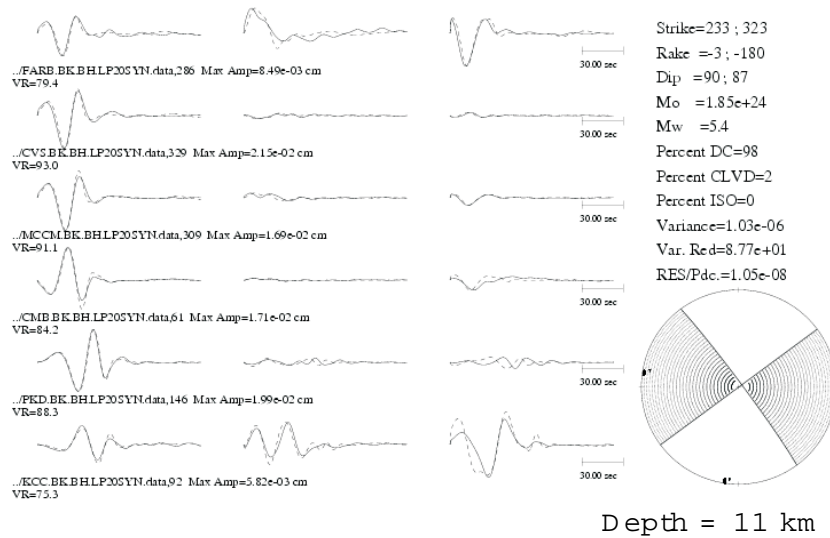


Figure 2.50: Moment tensor solution for the Alum Rock earthquake. The automatic solution used stations at short epicentral distances that were clipped or nonlinear. For this reviewed solution, the fits of the synthetics to the data are extremely good.

overall variance reduction is only 48 percent, and the vertical components, theoretically expected to be small given the focal mechanism, are not fit at all.

The details of the slip and the depth of the slip patch are not very well constrained, but are consistent with qualitative waveform analyses and with observed shaking (Figure 2.49 (top)). This model also argues for unilateral southeast rupture.

22.4 Perspectives

Future work is needed to more fully document the sensitivity of the finite-source model parameters. The peak slip in the model, assuming a rise time 0.3 seconds and rupture velocity of 80% of the shear wave velocity, is 17 cm. Like the moment tensor analysis, the finite source model produced an M_w 5.4.

22.5 Acknowledgements

Earthquake monitoring and reporting activities at the BSL are supported by the CISN funding of the California Governor's Office of Emergency Services under contract 6023-5 and the United States Geological Survey project 07HQAG0013.

22.6 References

Dreger, D. and A. Kaverina, Seismic remote sensing for the earthquake source process and near-source strong shaking: A case study of the October 16, 1999 Hector Mine earthquake, *Geophys. Res. Lett.*, 27, 1941-1944, 2000.

23. Moment Tensors for Very Long Period Signals at Etna Volcano, Italy

Margaret Hellweg, Andrea Cannata (Universita Catania), Stefano Gresta (Universita Catania), Sean Ford, Guiseppi Di Grazia (INGV Sezione di Catania)

23.1 Introduction

Very long period signals (VLP, 10 s - 30 s) associated with long period events (0.5 Hz - 5 Hz) were observed at Etna Volcano, Italy, during June-November 2005 (Figure 2.51). They are only recorded at the broadband stations nearest to Etna's craters, ECPN, EBEL, EPDN and EPLC. These stations are part of the permanent seismic network run by the Catania Section of the Istituto Nazionale di Geofisica e Vulcanologia (INGV). Although the signal-to-noise (S/N) ratio for these VLPs is in general only poor to fair, they seem to recur, and can be classified into two families. We attempt to improve the S/N by stacking and to determine moment tensors for the VLP events.

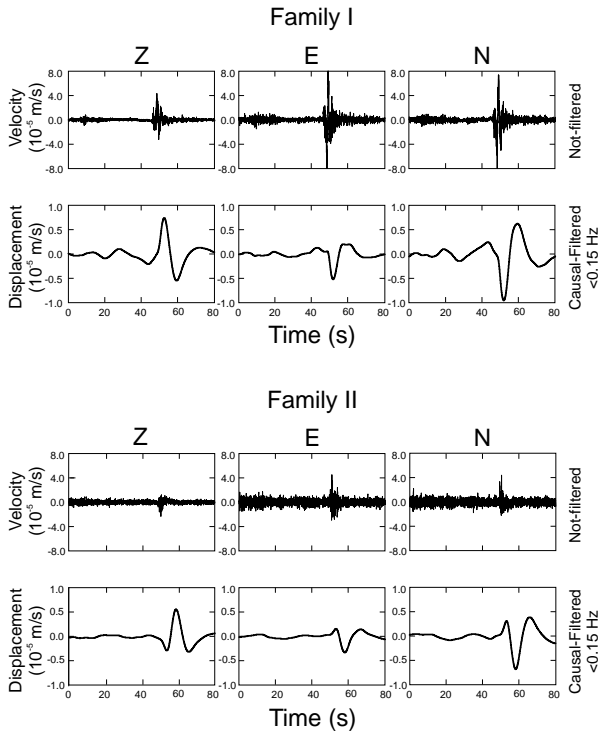


Figure 2.51: Example of long period (LP) associated very long period (VLP) events of Families I (top) and II (bottom). In each case, the upper rows show the broadband seismogram of the LP, while in the lower rows, the VLP signals are extracted by causal filtering.

23.2 Clustering and Stacking

The VLP events were clustered following *Green and Neuberg (2006)*. For all events, (i) the vertical component of ECPN station (highest S/N) was lowpass filtered at 0.15 Hz to exclude the ocean microseisms; (ii) the correlation matrix was calculated for all events using 30 s of data; (iii) the cross correlation threshold was chosen to be 0.95 so that fairly dissimilar events would be classified as a single family, while members of one family would not be grouped with another; (iv) a master event was selected (the event with the most correlation values above the threshold); (v) the average family waveform was created as the stack of all events correlated with the master event; (vi) the stack waveform was then cross-correlated with the original seismic records, and all events with greater correlation than the threshold were grouped into a waveform family; (vii) the steps iv-vi were repeated until all events were classified into distinct groups; (viii) finally, a new correlation matrix was constructed with events sorted into families. In this procedure, no overlap was allowed between clusters; in fact, once an event was assigned to a group, it was removed from further correlation. We found that 85% of the events could be grouped into two main families of VLP events. Families I and II had 194 and 87 members, respectively.

For further analysis, we used stacked seismograms for the two VLP families from the four summit station. The stacks were created using signals filtered with a 4-pole, causal Butterworth bandpass filter (0.033 Hz - 0.167 Hz). Using waveforms from all stations from two members of the family (12 waveforms for each event), we tried different time lags between the two sets of signals. For each time lag value, we evaluated the similarity between the events by averaging the cross correlation coefficients calculated for each pair of corresponding waveforms (for example “ECPNz of event 1” and “ECPNz of event 2”). The time lag was chosen which gave the maximum average cross correlation coefficient and the signals for each component at each station were stacked. New events were compared with and then added to the stack event. Thus, all the events contributed to the stacked signals representing the two families (Figure 2.52). Although the stacking was performed on the Z, N and E components, we show the traces for Z, R and T with the optimum rotation determined using polarization analysis (*Plesinger et al., 1986*). The S/N is clearly improved in the stacks, where several important characteristics are apparent. (1) For Family I, the first motion on the Z component is pos-

itive at all stations. (2) For Family II, the first motion on the Z component is negative at all stations. (3) For both families, the amplitudes on all components are considerably larger at ECPN and EPDN, the stations to the SW and NE of the active craters, than at EBEL and EPLC, which lie to the SE and NW.

23.3 Waveform Polarization

Note that there is little energy on the T-component at any of the stations (Figures 2.52 and 2.84). In addition, the vertical and radial components are “in phase”, with both Z and R being negative or positive at the same time. This is generally an indication for P-waves. The directions of particle motion of Family I and Family II stacks are very similar, differing at each station by only a few degrees.

In the horizontal plane, the motion at ECPN and EPDN is polarized more or less toward the active craters. The motion at EPLC and EBEL is comparatively small and has both an element pointing toward the crater and a later segment of the motion oriented transversely. However, the S/N ratio at these two stations is poor.

In the vertical plane, both ECPN and EPDN (SW and NE of the craters, respectively) both point slightly downward toward the crater. On the plots of vertical motion, the particle motion diagrams are shown at the altitudes of the stations. Again, the motion for EBEL and EPLC are small, with a hint of “downward toward the crater”.

23.4 Perspectives

The particle motion for these VLP signals is highly suggestive of either an initially opening (Family I) or initially closing (Family II) crack of fairly limited extent (little to no signal at EBEL and EPLC). There is a hint that the source is finite, as the directions of the horizontal particle motion change at ECPN and EPDN.

We have calculated Greens functions for full moment tensors using a simple half space velocity model. Initial inversions using *Minson and Dreger (2008)* indicate that a volume change explains a large portion of the waveforms. We will perform further analysis using a grid of sources to determine both the best source mechanism and its location.

23.5 References

Green, D., and J. Neuberg, Waveform classification of volcanic low-frequency earthquake swarms and its implication at Soufriere Hills Volcano, Monserrat, *J. Volcanol. Geotherm. Res.*, 153, 51-63, 2006.

Minson, S. and D. Dreger, Stable Inversions for Complete Moment Tensors, In press *Geophys. Journ. Int.*, 2008.

Plesinger, A., M. Hellweg and D. Seidl, Interactive high-resolution polarization analysis of broad-band seismograms. *J. Geophysics*, 59, 129-139, 1986.

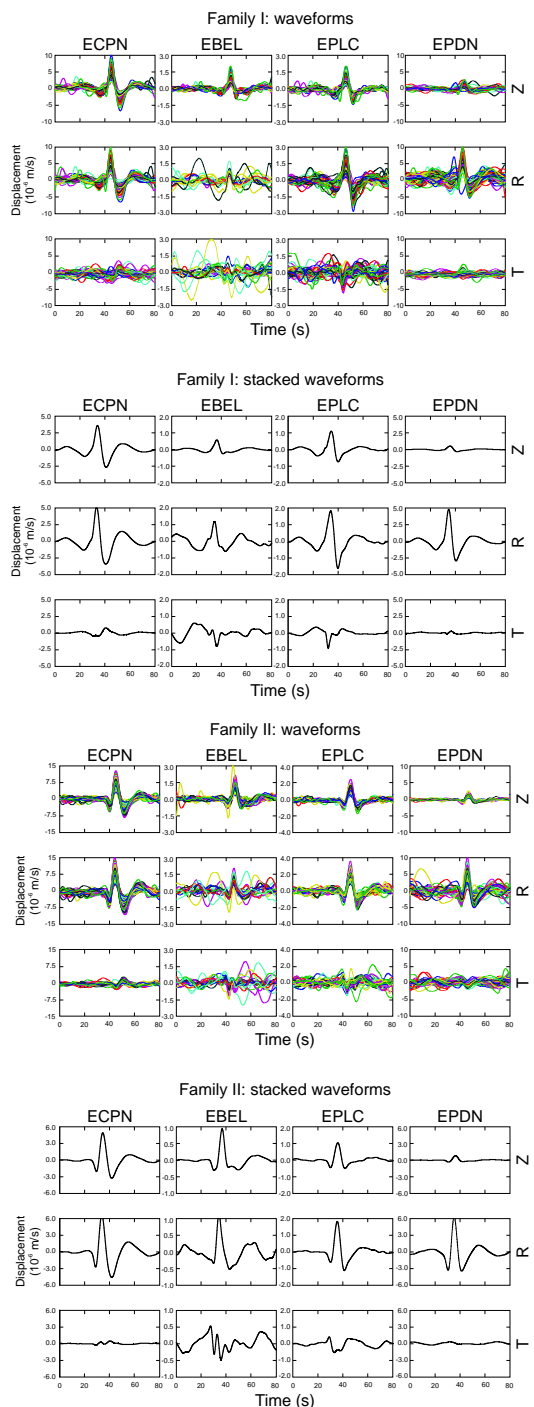


Figure 2.52: Stacked very long period (VLP) events of Family I (top) and Family II (bottom). The upper three traces show superimposed Z, R and T seismograms for all members at the 4 stations. Best azimuths were determined using polarization analysis. The lower traces show the stack seismograms.

24. Source Analysis of the February 24, 2008 M6 Wells, Nevada Earthquake

Douglas Dreger and Sean Ford

24.1 Introduction

On February 21, 2008 at 14:16:02 UTC, a M_w 6.0 earthquake occurred at 41.153 N, 114.867W, 10 km ENE of Wells, Nevada. This event caused significant damage in the historical section of the town. Unfortunately, there are no near-source strong motion recordings; however, at the time of the earthquake the EarthScope transportable array (TA) stations provided excellent records of the mainshock and aftershocks.

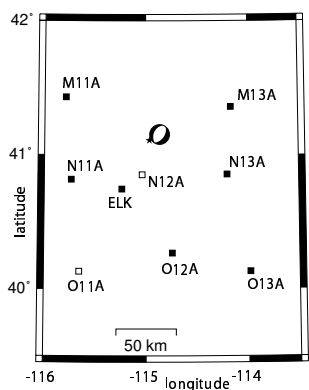


Figure 2.53: Locations of the transportable array and ANSS (ELK) stations. Solid symbols identify stations used in the finite-source inversion. Station N12A was omitted since it experienced a non-linear response, and O11A was omitted since ELK provided information from the same azimuth.

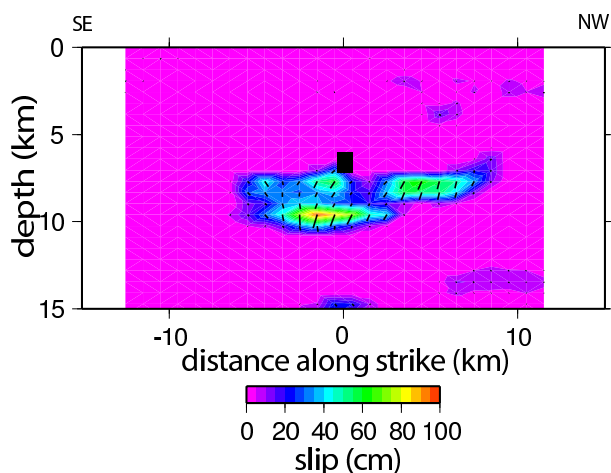


Figure 2.54: Slip model for SE-dipping fault plane. The color scale shows slip and the bars show the slip direction.

24.2 Seismic Moment Tensor

We determined a moment tensor solution using three-component, low frequency (0.02 to 0.05 Hz) displacement waves recorded by 47 stations of the NSF TA, and ANSS broadband seismic stations. Using the BSL seismic moment tensor code and the *Song et al.* (1996) velocity model, we obtained a normal faulting mechanism with the focal parameters strike=205, 35; rake=-96, -82; dip=40, 50. The source depth was constrained at 7 km as determined by the University of Nevada Reno Seismological Laboratory. The scalar seismic moment was determined to be 7.82×10^{24} dyne cm, corresponding to a M_w 5.9. The normal mechanism is consistent with the trend of basin and range faulting in the region; however, there is some question about whether west-dipping or east-dipping faults are active in the region.

24.3 Finite-Source Model

To determine the finite-source parameters we have inverted the three-component, broadband ($f > 0.02$ Hz) displacement waveform data recorded at the 7 closest, on-scale, US and TA network stations (Figure 2.53) using the method of *Kaverina et al* (2002). We tested both nodal planes of the moment tensor double-couple solution over a range of rupture velocities, and found that the east-dipping nodal plane consistently provided the best fit to the data. Although the maximum in the goodness of fit parameter (variance reduction) is relatively broad, the best rupture velocity was found to be 2.8 km/s, or 78% of the shear wave velocity at the hypocenter depth. These initial inversions considered a constant rake (slip angle) obtained from the double-couple solution. We also performed an inversion allowing the rake to vary over the rupture plane, which resulted in a slightly more compact slip distribution. As Figure 2.54 shows the rupture is bilateral and slightly down-dip, but the largest slip is located to the southwest of the hypocenter in the direction of the town of Wells, Nevada. The slip in the variable rake model shows some variation but is predominantly normal, with the east-block down relative to the west-block. The peak slip in this model is 85 cm, with an average of 13 cm. The scalar seismic moment obtained by integrating the fault slip is 1.09×10^{25} dyne cm, corresponding to M_w 6.0. A rise time of 0.3 seconds was assumed. As Figure 2.55 shows, the fit to the regional data is very good.

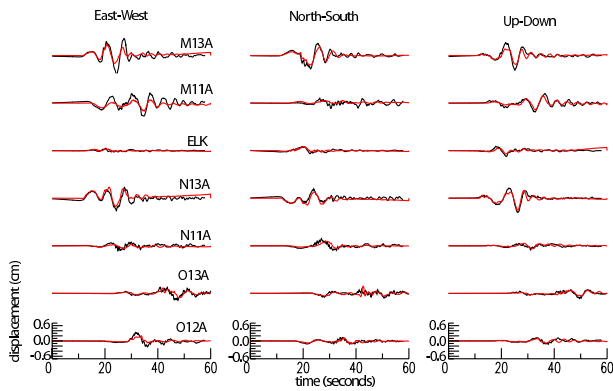


Figure 2.55: Observed three-component displacement records (black) are compared to synthetics (red). The data and synthetics are broadband with no filtering other than the polezero instrument response removal for the data.

24.4 ShakeMap

There are no strong motion stations located within 200 km of the Wells, NV earthquake, and, therefore, the ShakeMap (Wald *et al.*, 1999a) is based solely on empirical ground motion relations and scaling from reported Community Internet Intensity Map values (Wald *et al.*, 1999b). Using the slip distribution in Figure 2.54, and assuming a NEHRP class C site (555 m/s), we have simulated the near-fault strong shaking to produce a ShakeMap using the method proposed by Dreger and Kaverin (2000), and as discussed in Dreger *et al.* (2005) and Rolandone *et al.* (2006). Figure 2.56 compares the simulated peak ground velocity (shaded map) with the USGS ShakeMap (contours) and PGV at the regional TA stations. The simulated values are consistent with the observations, whereas the USGS ShakeMap over predicts values by more than a factor of 10. In Wells, NV we simulate a PGV of 10 cm/s, which is large enough to account for the considerable damage to the historic, unmaintained, unreinforced masonry buildings. The simulated sense of motion in Wells is down and to the east, which is consistent with reported westward chimney toppling, and sliding of heavy objects. This event occurred in a poorly instrumented region and demonstrates the difficulty in obtaining a ShakeMap under such conditions. This analysis shows, as in Dreger and Kaverina (2000), that in such poorly instrumented regions a regional data derived finite-source model from regional waveform modeling can be used to accurately simulate near-fault strong ground motions when no such recordings exist.

24.5 References

Dreger, D., and A. Kaverina, Seismic remote sensing for the earthquake source process and near-source strong shaking: A case study of the October 16, 1999 Hector Mine earthquake, *Geophys. Res. Lett.*, *27*, 1941-1944, 2000.

Dreger, D. S., L. Gee, P. Lombard, M. H. Murray, and

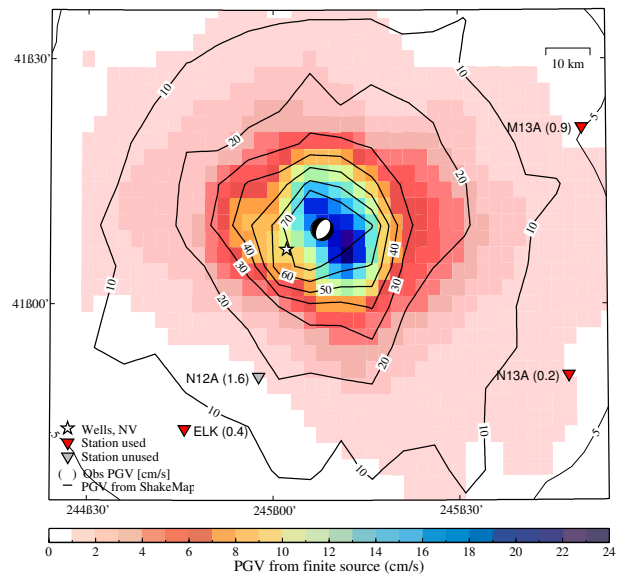


Figure 2.56: Simulated PGV (color shading) is compared to the USGS ShakeMap (contours) and PGV from TA stations (numbers in parentheses). There is good correlation between the finite-source simulated PGV and observations; however, the USGS ShakeMap shows values an order of magnitude larger. There were no near-fault strong motion data available for use in the USGS ShakeMap.

B. Romanowicz, Rapid finite-source analysis and near-fault strong ground motions: Application to the 2003 M_w 6.5 San Simeon and 2004 M_w 6.0 Parkfield earthquakes, *Seism. Res. Lett.*, *76*(1), 40-48, 2005.

Kaverina, A., D. Dreger, and E. Price, The combined inversion of seismic and geodetic data for the source process of the 16 October 1999 M_w 7.1 Hector Mine, California, Earthquake, *Bull. Seism. Soc. Am.*, *92*(4), 1266-1280, 2002.

Rolandone, F., D. Dreger, M. Murray, and R. Bürgmann, Coseismic slip distribution of the 2003 M_w 6.6 San Simeon earthquake, California, determined from GPS measurements and seismic waveform data, *Geophys. Res. Lett.*, *33*, L16315, doi:10.1029/2006GL027079, 2006.

Song, X. J., D. V. Helmberger and L. Zhao, Broadband modelling of regional seismograms; the basin and range crustal structure, *Geophys. J. Int.*, *125*(1), 15-29, 1996

Wald, D. J., V. Quitoriano, T. H. Heaton, H. Kanamori, C. W. Scrivner, and C. B. Worden, TriNet ShakeMaps: Rapid Generation of Instrumental Ground Motion and Intensity Maps for Earthquakes in Southern California, *Earthquake Spectra*, *15*, 537-556, 1999a.

Wald, D. J. V. Quitoriano, L. A. Dengler, and J. W. Dewey, Utilization of the Internet for Rapid Community Intensity Maps, *Seismological Research Letters*, *70*(6), 680-697, 1999b.

25. Triggering effect of $M > 4$ earthquakes on the observed occurrence of repeating events at Parkfield

Kate Huihsuan Chen, Roland B3rgermann, and Robert M. Nadeau

25.1 Introduction

A characteristic repeating earthquake sequence (RES) is defined as a group of events with nearly identical waveforms, locations, and magnitudes and thus represents a repeated rupture of the same patch of fault. The recurrence intervals of repeating earthquake ruptures are found to be highly variable, where the irregular recurrence of observed repeating events may reflect a response to nearby earthquakes, change in the strain rate, time-dependent or spatial variation in the frictional strength of the fault, or other effects such as fluid pressure variations (e.g., *Lay and Kanamori, 1980; Sleep and Blanpied, 1994; Vidale et al., 1994; Nadeau et al., 1994; Ellsworth, 1995*). The questions of interest regarding the recurrence properties of natural earthquake sequences are: How do the RESs respond to stress perturbation associated with larger earthquakes and to what range (both in space and time) are the triggering effects effective? To answer these questions, we need a statistically sufficient observational documentation of recurrence properties in natural earthquake populations.

25.2 Data and results

The detailed record of micro-earthquake data from the borehole High Resolution Seismic Network (HRSN) sites at Parkfield provides a unique opportunity to examine how larger events act on the observed occurrence of the repeating events. With the high level of detection of micro-earthquakes, the HRSN has revealed a larger number of repeating earthquakes ranging in magnitude from -0.4 to $+1.7$ (*Nadeau et al., 1995; Nadeau and McEvilly, 1997*). During the period 1987-1998, 187 repeating sequences were identified, with a total of 1123 events. Using these data, we seek to illustrate how the larger earthquakes influence RESs' timing. We are interested in any potential variation of recurrence interval associated with the time of major events. The analysis has the following recurrence elements (Figure 2.57a): (1) "dt+" : the time difference between a major earthquake and the recurrence of a repeating event subsequent to the major event; (2) "dt-" : the time difference between a major earthquake and the repeating event prior to the major event; (3) "Tr-post" : the duration of the first full recurrence interval following the major event; and (4) "Tr-cos" : the recurrence interval spanning the major event, that is, the sum of dt- and dt+. These elements are later divided by the average recurrence interval of a given RES (\bar{Tr}). The percentage of normalized interval estimates at

a distance of less and greater than 5 km from the major events are shown in Figure 2.57b. Extremely short times between the main event and subsequent RES events ($dt+/\bar{Tr} < 0.1$) reflect triggering by the major events. In Figure 2.57b, the peak at $dt+/\bar{Tr} < 0.1$ only appears in the near-field (e.g., in the plot for distances less than 5 km from the major event). This may suggest triggering by static stress as a cause of the short recurrence intervals immediately after the larger event.

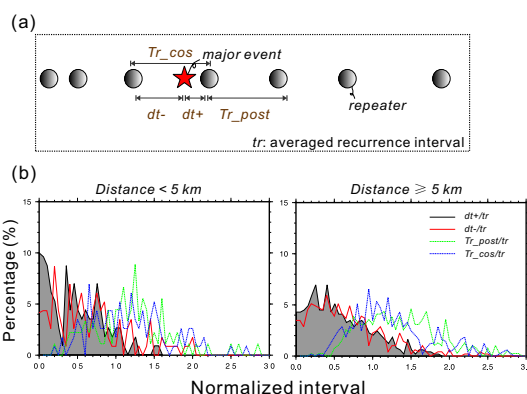


Figure 2.57: (a) Illustration of the four recurrence elements in time window. Star is the time of major event. Circles are the repeating events in a RES. (b) Percentage of normalized interval measurements (recurrence element divided by average recurrence interval) at a distance of less (left panel) and greater (right panel) than 5 km from $M 4$ hypocenters.

To further explore the region (both in space and time) where interaction between RESs and larger events is most evident, we have selected the 1993 $M 4.5$ earthquake, with a large number of RESs in the vicinity, for the following analysis. In Figure 2.58a the event chronologies of the RESs adjacent to the 1993 event reveal coherently reduced recurrence times over years (1993 to 1998) following the $M > 4$ event. To quantify the enduring acceleration of recurrence, we determine the ratio of averaged post-1993 to pre-1993 recurrence intervals as a function of distance from the 1993 $M 4.5$ hypocenter in Figure 2.58b. Within a distance of 5 km from the $M 4.5$ event, most of the RESs (84%) have shorter post-1993 recurrence intervals compared to the pre-1993 intervals. We find that the enduring recurrence acceleration, defined by 'post-1993- Tr /pre-1993- Tr ' of less than 1 in Figure 2.58b, can be documented 5 km from the major event.

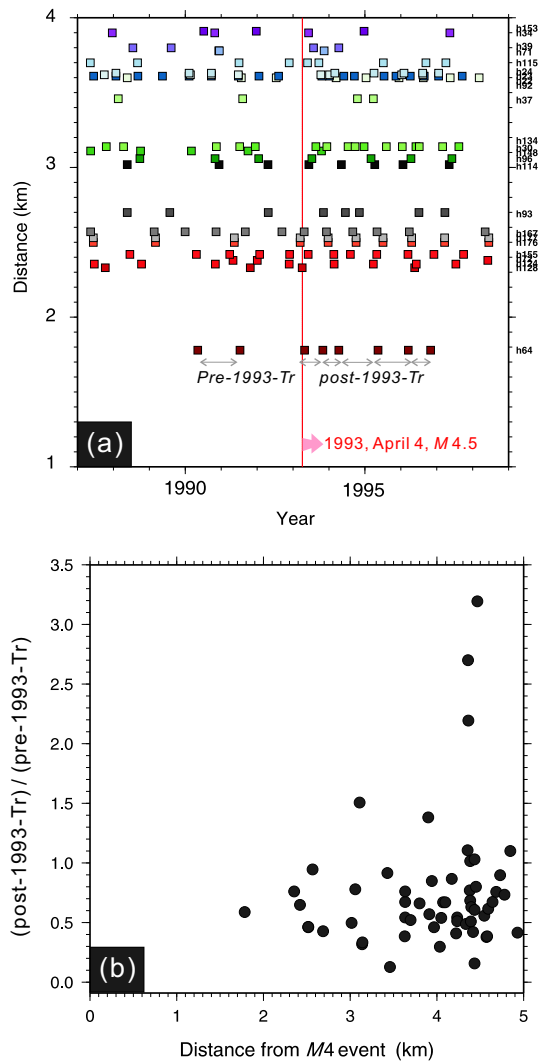


Figure 2.58: (a) Event chronologies of RESs as a function of distance from the 1993 M 4.5 hypocenter. Note that the distance is confined to be less than 4 km due to abundant RESs beyond 4 km. Red and blue arrows indicate the post-1993 and pre-1993 recurrence interval, respectively. (b) Ratio of the averaged post-1993 recurrence intervals and the average values of the pre-1993 recurrence intervals as a function of distance from 1993 M 4.5 event.

25.3 Discussion

The triggering effect of moderate events ($M 4\sim 5$) is observable in the temporal variation of recurrences from repeating earthquake data as shown by the unusually short $dt+/tr$ in Figure 2.57b. The immediate acceleration of recurrence following the $M 4\sim 5$ events is only found to occur in the near field, which is possibly explained by static stress triggering. Different from the decaying recurrence rate that reflects afterslip following a large event, many

of the Parkfield RESs exhibit a steady, accelerated recurrence since 1993. We argue that the long-lasting, reduced recurrence interval is not likely explained by the afterslip process. This acceleration may be part of a more broadly distributed increase in creep rates along this fault segment that is associated with a remarkable aseismic transient following several $M > 4$ events during the early 1990s (Nadeau and McEvelly, 1999; Niu et al., 2003; Murray and Segall, 2005).

25.4 References

Ellsworth, W. L. (1995), Characteristic earthquakes and long-term earthquake forecasts; implications of central California seismicity, in *Urban Disaster Mitigation: the Role of Science and Technology*, Eds. Cheng, F.Y., and M.S. Sheu, *Elsevier Science Ltd.* 1-14.

Lay, T. and Kanamori, H. (1980), Earthquake doublets in the Solomon Islands, *Phys. Earth and Planet. Inter.*, 21, 283-304.

Murray, J., and P. Segall (2005), Spatiotemporal evolution of a transient slip event on the San Andreas fault near Parkfield, California, *J. Geophys. Res.*, 110, doi:10.1029/2005JB003651.

Sleep, N. H., and M. L. Blanpied (1994), Ductile creep and compaction: a mechanism for transiently increasing fluid pressure in mostly sealed fault zones. *Pure App. Geophys.*, v. 143, pp. 9-40.

Vidale, J. E., W. L. Ellsworth, A. Cole, and C. Marone (1994), Variations in rupture process with recurrence interval in a repeated small earthquake, *Nature*, 368, 624-626.

Nadeau, R., M. Antolik, P. A. Johnson, W. Foxall, and T. V. McEvelly (1994), Seismological studies at Parkfield III: Microearthquake clusters in the study of fault-zone dynamics, *Bull. Seismol. Soc. Am.*, 84, 247-263.

Nadeau, R. M., W. Foxall, and T. V. McEvelly (1995), Clustering and periodic recurrence of microearthquakes on the San Andreas fault at Parkfield, California, *Science*, 267, 503-507.

Nadeau, R. M. and T. V. McEvelly (1997), Seismological studies at Parkfield V: Characteristic microearthquake sequences as fault-zone drilling targets, *Bull. Seism. Soc. Am.*, 87, 1463-1472.

Nadeau, R. M. and T. V. McEvelly (1999), Fault slip rates at depth from recurrence intervals of repeating microearthquakes, *Science*, 285, 718-721.

Niu, F., P. G. Silver, R. M. Nadeau, T. V. McEvelly (2003), Stress-induced migration of seismic scatterers associated with the 1993 Parkfield aseismic transient event, *Nature*, 426, 544-548.

26. Realtime Test of the ElarmS Earthquake Early Warning Methodology

Richard M Allen, Holly Brown, Margaret Hellweg, Alexei Kireev, Douglas Neuhauser

26.1 Introduction

Modern seismic networks and telemetry systems make it possible to rapidly detect the beginnings of earthquakes. Combining these technical capabilities with recently developed methodologies to estimate earthquake magnitude using just a few seconds of P-wave data (e.g. *Allen and Kanamori, 2003*) makes it possible to provide a few seconds warning prior to damaging ground shaking. ElarmS is the methodology under development and testing at the Berkeley Seismological Laboratory. It is designed to provide earthquake early warnings by compiling data from multiple seismic stations, and updating those warnings every second as additional data becomes available (*Wurman et al., 2007*).

26.2 Realtime state-wide testing

The Berkeley Seismological Laboratory is a partner in the state-wide effort to test algorithms for the purpose of earthquake early warning. This is an effort by CISEN partners (UC Berkeley, Caltech, USC/SCEC, USGS and ETH Zurich) and funded by the USGS. The goal of the project is to implement early warning algorithms within the realtime processing system of the CISEN to evaluate algorithm performance in terms of warning accuracy and timeliness.

The ElarmS algorithms have now been ported to continuous realtime processing in California. The system, referred to as ElarmS-RT, provides automated detection, location, magnitude estimation, and ground shaking prediction. As with the previous non-realtime implementations of ElarmS, the output can be displayed as an "AlertMap" which maps the predicted peak ground motion starting one second after the first seismic station to trigger and updates every second. In addition to these early warning products, ElarmS-RT also provides very rapid post-event information. One such product is the ElarmS-ShakeMap. It is available immediately after peak ground shaking has been observed within 100 km of the epicenter (the usual frame size of a ShakeMap) and is the same as the CISEN ShakeMap except that the ElarmS magnitude estimate is used and the map is therefore available more rapidly.

26.3 Earthquake detections

ElarmS-RT was operational at the time of the October 30th, 2007, M_w 5.4 Alum Rock earthquake near San Jose, the largest earthquake to strike the San Francisco

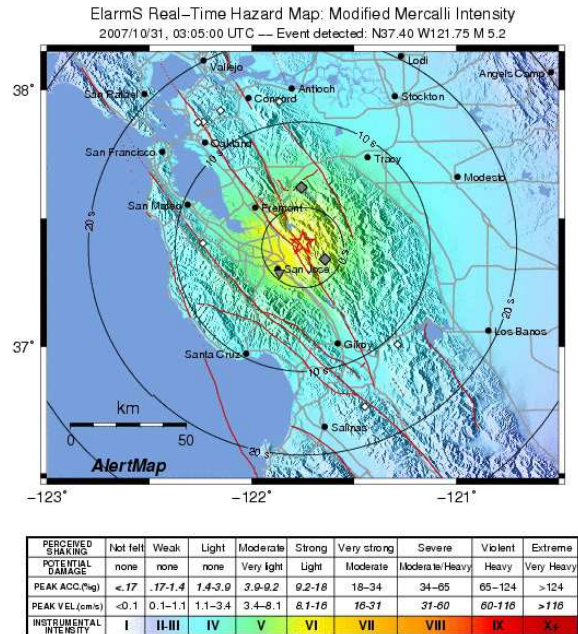
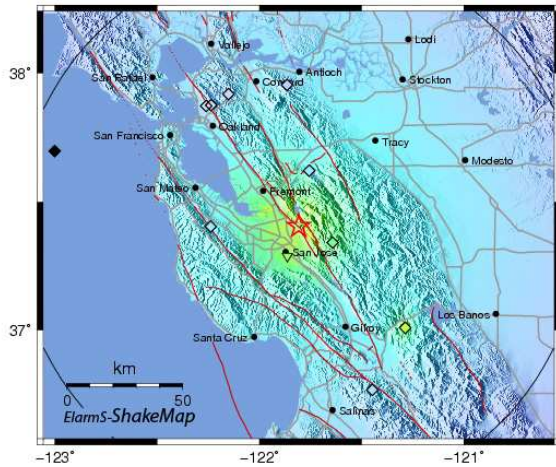


Figure 2.59: AlertMap: Ground motion prediction generated by ElarmS-RT using the data available 1 sec after the Alum Rock earthquake was detected.

Bay Area since the 1989 Loma Prieta earthquake. The system first detected the earthquake when two seismic stations triggered simultaneously in the epicentral region. One second later, the first magnitude estimate of 5.2 was available and the first AlertMap (Figure 2.59) was calculated. The error in the MMI predictions at this time was 0.1 ± 0.6 (in MMI units). These are small errors, as can be seen by comparing Figure 2.59 with Figure 2.60 which shows the ElarmS-ShakeMap for the event. As time proceeded, additional data was incorporated and the errors in the ground motion prediction decreased further.

ElarmS-RT currently processes data 15 sec behind realtime. The current telemetry system in Northern California provides most data with 5 to 10 sec delay. By waiting 15 sec ~90% of seismic stations have reported before a particular time increment is processed. Even with this 15 sec delay, ElarmS-RT computers had assessed the hazard posed by the Alum Rock earthquake before ground shaking was felt in San Francisco.

The ElarmS-ShakeMap is generated using the data



PERCEIVED SHAKING	Not felt	Weak	Light	Moderate	Strong	Very strong	Severe	Violent	Extreme
POTENTIAL DAMAGE	none	none	none	Very light	Light	Moderate	Moderate/Heavy	Heavy	Very Heavy
PEAK ACC.(mg)	<.17	.17-1.4	1.4-3.9	3.9-9.2	9.2-18	18-34	34-65	65-124	>124
PEAK VEL.(cms)	<0.1	0.1-1.1	1.1-3.4	3.4-8.1	8.1-16	16-31	31-60	60-116	>116
INSTRUMENTAL INTENSITY	I	II-III	IV	V	VI	VII	VIII	IX	X+

Figure 2.60: ElarmS-ShakeMap using observations of peak ground motion and ElarmS magnitude for the Alum Rock earthquake and typically available within 1.5 minutes. This is nearly identical to the CISN-ShakeMap.

available 30 sec after the origin time of all detected earthquakes. This time interval allows peak ground shaking to be observed within ~ 100 km of the event. The ElarmS-ShakeMaps are usually available within 1.5 minutes of the origin time. The ElarmS-ShakeMap for the Alum Rock earthquake is shown in Figure 2.60 and is nearly identical to the CISN ShakeMap. CISN ShakeMaps are typically available in 7 to 10 minutes.

26.4 Conclusions

The Alum Rock earthquake was a successful illustration of ElarmS-RT performance. While the realtime testing of early warning in California has only just begun, some of the requirements for a fully implemented system are becoming clear. ElarmS performs well for all events $M > 3$ in the greater Bay Area where instrumentation is dense and typical station spacing is ~ 20 km. To the north and south of the Bay Area along the San Andreas Fault System, instrument density drops and typical stations spacing is ~ 100 km. In these regions, the system works, but is slower, as it takes longer for the radiating seismic waves to be sampled. East of the Mendocino Triple Junction, in the Sierras, and in the Central Valley of Northern California, current instrumentation is not sufficient for ElarmS operation.

26.5 Acknowledgements

Support for this project is provided by the USGS NEHRP program (06HQAG0147).

26.6 References

- Allen, R. M., and H. Kanamori, The potential for earthquake early warning in southern California, *Science*, 300, 786-789, 2003.
- Wurman, G., R. M. Allen, and P. Lombard, Toward earthquake early warning in northern California, *J. Geophys. Res.*, 112 (B08311), 2007.

27. Testing the ElarmS Methodology on Japanese Earthquakes

Holly Brown and Richard Allen

27.1 Introduction

Earthquake early warning systems are algorithms designed to detect the initial P-waves from an earthquake, rapidly estimate the magnitude of the event, and predict subsequent ground shaking in the surrounding regions. Earthquake Alarm Systems, or ElarmS, is one early warning algorithm that uses a network of seismic stations to hone in on the size and location of the earthquake. Averaging the magnitude estimates from multiple stations improves the accuracy of the estimate. ElarmS has been tested on multiple Northern and Southern California datasets, and now automatically processes streaming seismic data across California. In order to improve the robustness of the methodology, we test it on a dataset of large-magnitude events from Japan's Kyoshin Net (K-NET) strong-motion seismic network.

27.2 Dataset

K-NET consists of 1,000 digital strong-motion seismometers spaced at approximately 25km intervals throughout Japan. Each station is capable of recording acceleration up to 2000 cm/s^2 . Our K-NET dataset contains 84 earthquakes occurring within 100km of K-Net stations between September 1996 and June 2008 (Figure 2.61). The local magnitudes range from 4.0 to 8.0, the largest being the 26 September 2003 Tokachi-Oki event. Forty-three of the events are of magnitude 6.0 or greater.

27.3 Method

ElarmS estimates magnitude from the frequency content and peak displacement of the first several seconds of the P-wave arrival at each station. *Allen and Kanamori (2003)* and *Olson and Allen (2005)* documented an empirical relationship between the magnitude and the maximum frequency parameter τ_p^{max} of the P-wave. *Wurman et al (2007)* further showed a relationship between magnitude and peak displacement, P_d , in the initial seconds of the P-wave arrival. ElarmS utilizes both relationships to calculate two magnitude estimates, which it then averages together to improve accuracy in the final event estimate. As more stations report P-wave arrivals, ElarmS incorporates their τ_p^{max} and P_d measurements into the average for an overall estimate of event magnitude.

ElarmS in California assumes a fixed depth of 8km and estimates the epicentral distance with a two-dimensional grid search. In the Japanese subduction zone this is inappropriate. For the Japanese dataset we create a three-dimensional grid and calculate the IASP91 P-S travel

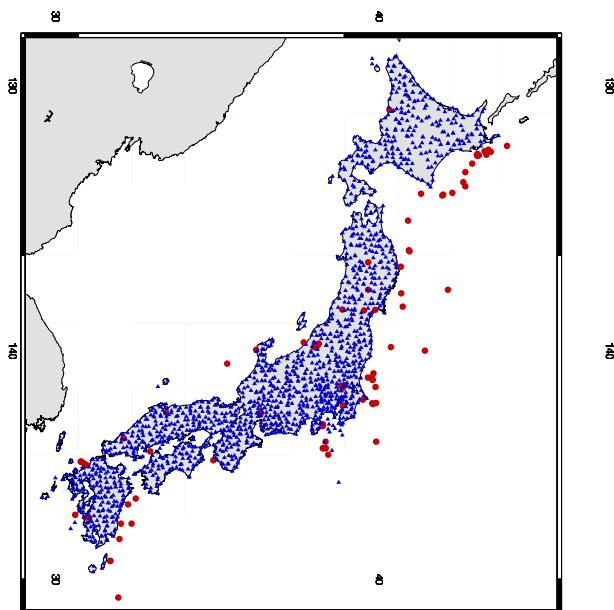


Figure 2.61: Map of events and K-NET stations: Large circles are events used in this study. Small triangles are K-NET stations.

time for seismic waves originating at each point of the grid. We then compare the calculated travel times to the observed P-S travel times at each station to find the best estimate of hypocentral location. Data is used only from stations within 100km of the hypocenter.

27.4 Results

We use a least-squares fit to calculate a local relationship between magnitude and τ_p^{max} of $\log_{10}(\tau_p^{max}) = -1.22 + 0.21 * M$, compared to $\log_{10}(\tau_p^{max}) = -0.78 + 0.15 * M$ for Northern California (*Wurman et al, 2007*) (Figure 2.62a). The observed τ_p^{max} values from Japan are similar to those of Northern California, with a slightly steeper slope for Japan.

We also use a least squares fit to calculate a local relationship between magnitude and peak displacement of $\log_{10}(P_d) = -4.02 + 0.66 * M$, corrected for epicentral distance, compared to $\log_{10}(P_d) = -3.77 + 0.73 * M$ for California (*Wurman et al, 2007*) (Figure 2.62b). The P_d relations have comparable slopes for Japan and Northern California, but Japan displays lower observed P_d values, implying greater attenuation in the region.

We further consider the effect of different quantities of data by limiting the number of stations used for magni-

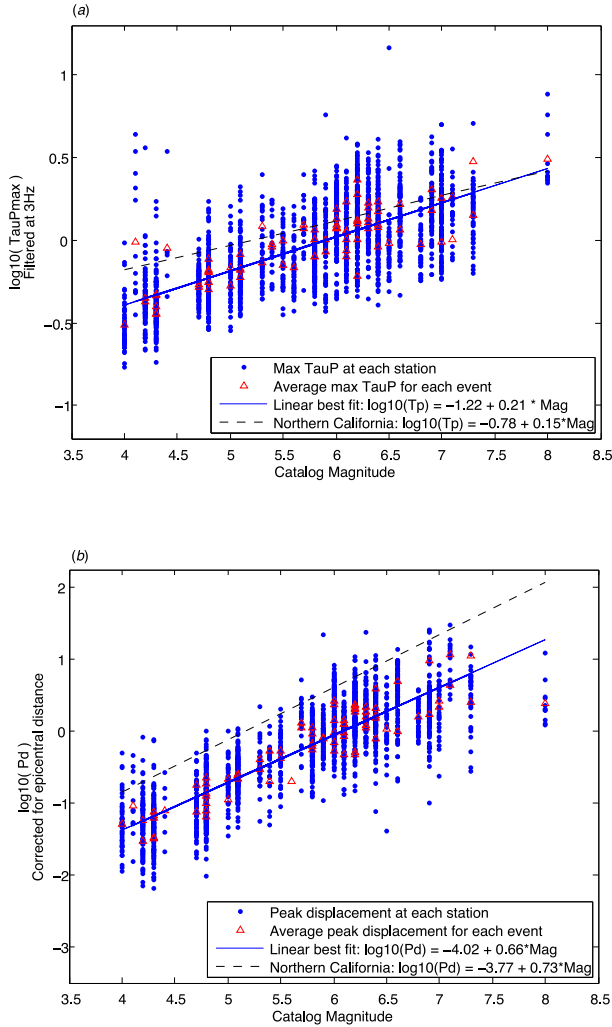


Figure 2.62: Observations from first 4 seconds of P-wave arrival at each station. (a) Observed $\log(\tau_p^{max})$ versus Catalog Magnitude. τ_p^{max} is peak frequency filtered at 3Hz. (b) Observed $\log(P_d)$ versus Catalog Magnitude. P_d is peak displacement corrected for epicentral distance.

tude estimates. Figure 2.63 shows the average error in the ElarmS estimated magnitude using only the single closest station to the epicenter, the two closest stations, three closest, etc. The dashed lines show the error in the magnitude estimate using only τ_p^{max} or P_d . The solid line is the error using both τ_p^{max} and P_d .

The combined τ_p^{max} and P_d estimate has an average error of less than 0.6 magnitude units using only one station for each event, and that error drops lower with the addition of more stations. P_d by itself produces an average error of less than 0.5 magnitude units for all numbers of stations. τ_p^{max} by itself produces an error that is higher than that of P_d , but still less than one magnitude unit when using more than one station. Previous studies have shown that the ElarmS magnitude estimates

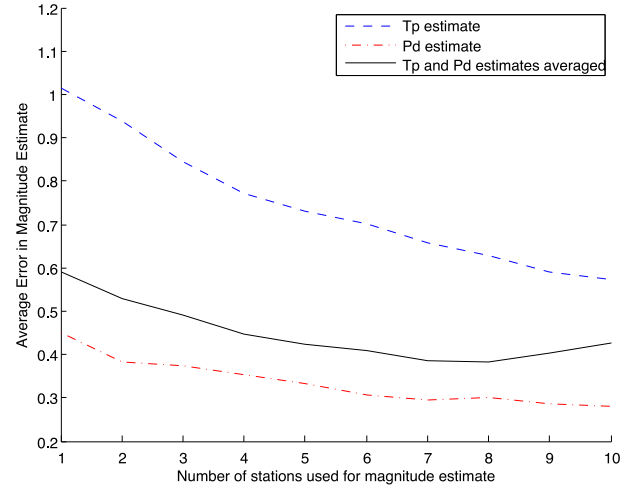


Figure 2.63: Magnitude error by number of stations

are more robust for large events when τ_p^{max} and P_d estimates are combined (Wurman *et al.*, 2007), although we have not yet verified this for the Japanese dataset.

27.5 Conclusion

The scaling relations between τ_p^{max} and magnitude and between P_d and magnitude are clearly evident for this Japanese dataset. This is a particularly valuable result given the large number of large ($M > 6$) earthquakes, implying that the ElarmS methodology remains robust and useful for large magnitude events. The hypocentral depth algorithm we added for this study extends ElarmS' range of geologic settings to subduction zones, in addition to the strike-slip faults of California.

27.6 Acknowledgements

Support for this project is provided by the USGS NEHRP program (06HQAG0147).

27.7 References

- Allen, R.M., and H. Kanamori, The potential for earthquake early warning in southern California, *Science*, 300, 786-789, 2003.
- Olson, E.L., and R.M. Allen, The deterministic nature of earthquake rupture, *Nature*, 438, 212-215, 2005.
- Wurman, G., R.M. Allen and P. Lombard, Toward earthquake early warning in northern California, *J. Geophys. Res.*, 112 (B08311), 2007.

28. Detection of Low-Frequency Earthquakes in the non-volcanic tremor beneath the San Andreas Fault: a prospective tool for investigating deep fault dynamics?

Andrea Cannata (University of Catania), Margaret Hellweg, Robert M. Nadeau, Stefano Gresta (University of Catania)

28.1 Introduction

Non-volcanic tremor (NVT) has been observed in Cascadia, in southwest Japan and along the San Andreas Fault (*Schwartz and Rokosky, 2007*). In southwest Japan, the NVT is accompanied by relatively energetic and isolated pulses that have been identified as low-frequency earthquakes (LFEs; *Shelly et al., 2006*). Compared with nearby ordinary earthquakes with similar amplitudes, LFEs are enriched in low frequencies (1-5 Hz). These events occur almost exclusively as part of an extended tremor signal (*Shelly et al., 2006*). The analysis of such events allows the source of tremor to be tracked with good resolution in time and space, providing the capability of monitoring slow slip with good precision as it migrates along the subduction zone (*Shelly et al., 2007*). Episodes of NVT along the San Andreas Fault (*Nadeau and Dolenc, 2005*) occur less often, are shorter and release less energy than those in the subduction zones. The aim of this work is to develop a detection procedure for LFEs in the NVT recorded along the San Andreas Fault in 2006-2007. In fact, the study of these events could contribute to significantly improving our knowledge of the deep dynamics of the San Andreas fault.

28.2 Data and Detection Methods

In this work the seismic signals recorded by the High-Resolution Seismic Network (HRSN; Figure 2.64a; see Chapter 3, Section 4.) were used. The analysis was applied to seismic signals from 48 NVT tremor episodes. Data windows start about 10 minutes before the beginning of the NVT and stop about 10 minutes after they end, giving a total of approximately about 30 hours.

To verify that the channels work and to highlight the frequency band characterised by the highest energy during the NVT episodes, the seismic signal was analysed using a Fast Fourier Transform (FFT). The tremor time series was divided into windows about 16 s long. The spectrum was calculated for each window (overlapping by 8 s) with a frequency resolution of 0.06 Hz. Then, the time development of the spectrum and its average were calculated for each tremor episode. Amplitudes were highest in the frequency band from 2 to 8 Hz, if signals below 2 Hz are excluded, where the signal to noise ratio is low and the sensor response drops off. Based on this result we decided to analyse this frequency band.

The detection method is divided into two steps, trigger detection and trigger selection.

Trigger detection

Trigger detection was based on three STA/LTA algorithms (short time average over long time average), each of which evaluates the ratio between short- and long-term energy density (squared data to facilitate combining multi-channel data in a Pythagorean sense) to find amplitude transients (*Withers et al., 1998*). The first, the standard STA/LTA, was applied to three narrow frequency bands 2-4, 4-6 and 6-8 Hz, producing three lists of triggers. Because the optimal lengths of the windows depend on the frequency content of the seismic signal, the lengths of the short and long windows were chosen to be 3 and 27 times the center period of the frequency band analysed, respectively. Moreover, in this first method the data window is rectangular. In the second algorithm, the adaptive standard STA/LTA, the entire 2-8 Hz band was analysed. As an estimator of the dominant peak frequency, needed to adaptively calculate the length of the short and long windows, the moving average of the instantaneous frequency over 1.5 s was used, and the data window was also rectangular. Finally, in the third algorithm, the adaptive recursive STA/LTA, the data were windowed using a decaying exponential. The frequency band analysed was 2-8 Hz and the window lengths were calculated adaptively, as in the second algorithm.

Using these three algorithms we obtained 5 lists of triggers for each station. Then, by sliding 10-second-long moving windows over the lists for all stations, groups of triggers common at more than two stations were formed. Thus, we obtained 5 lists of common triggers from 5 lists of triggers for each station.

Trigger Selection

Because the signals that we are looking for have small amplitudes, the STA/LTA thresholds were set to low values. Obviously, the lower this threshold is, the less “reliable” are the triggers obtained. Therefore, two selection criteria were used to retain only “reliable” triggers. The first was based on the number of stations: only the triggers common at least at “N” stations were taken into account. The second consisted of evaluating the consistency of the time distribution of the common triggers with the locations of the stations: we plotted longitude and latitude of the stations and trigger time in the x, y and z axes, respectively; then, we determined the best fit plane, the one minimizing the perpendicular distances

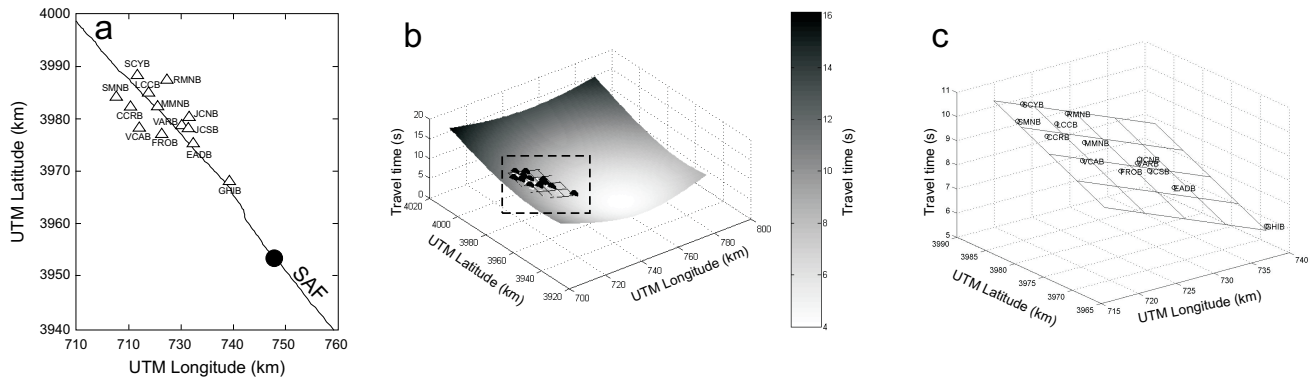


Figure 2.64: (a) Map showing the locations of the 13 stations belonging to the HRSN (triangles), a portion of the San Andreas Fault (SAF) and the epicentre of the theoretical source (black dot). (b) Distribution of the theoretical travel times (surface) and the fitting plane (grid plane) obtained taking into account only the 13 points corresponding to the stations (black dots); the dashed rectangle shows the portion of the plot highlighted in (c). (c) Theoretical travel times at the considered stations (black circles) and fitting plane (grid plane). See text for details.

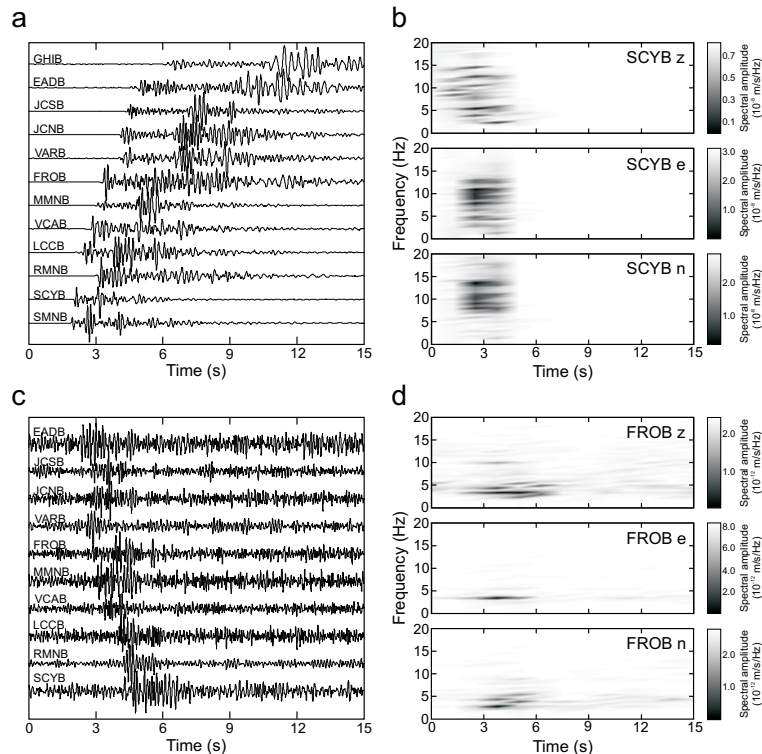


Figure 2.65: (a) Vertical component velocity recorded on January 30, 2006 (filter: 2-8 Hz) and (b) velocity spectrograms of the three components at SCYB. (c) Velocity signal of one of the horizontal component recorded on April 30, 2006 (filter: 2-8 Hz) and (d) velocity spectrograms of the three components at FROB.

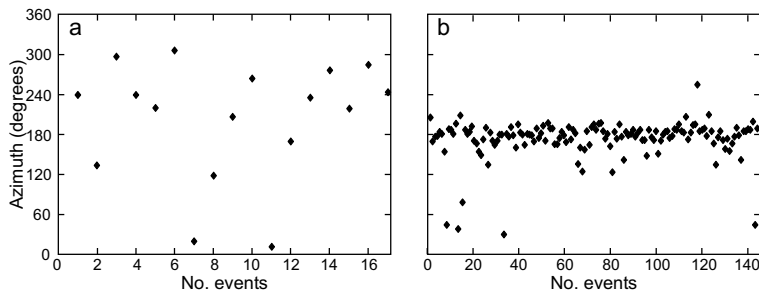


Figure 2.66: Azimuth values of the events of (a) group 1 and (b) group 2, obtained by using the plunge of the fitting plane.

from the stations, and calculated the residuals. Therefore, the triggers common at least at “N” stations were considered “reliable” if the sum of the rectified residuals was lower than a certain threshold, called “E”. Obviously, this method is valid only if the source is far away from the station network; the tremor source location reported in *Nadeau and Dolenc* (2005) supports this assumption. By this fitting plane we were also able to roughly calculate an azimuth value for each group of common triggers, corresponding to the plunge direction of the plane. Figure 2.64a shows the epicentre of a theoretical source, located at depth of 20 km, roughly corresponding to the epicentre and the depth of the tremor source reported in *Nadeau and Dolenc* (2005); the distribution of the theoretical travel times, calculated using this theoretical source, are shown as the surface in Figure 2.64b and black circles in Figure 2.64c. In these figures, the best fit plane obtained taking into account only the 13 points corresponding to the stations is shown as a grid.

The values for “N” and “E” were chosen to be 7 and 10, respectively, as representing a good trade-off between consistency of the time distribution of the common triggers with the distribution of the stations, and high number of remaining groups of common triggers.

28.3 Detection Results

By applying the detection procedure on the 5 lists of common triggers, we found 161 “events” that can be divided into two groups. The first consists of 17 events with impulsive onsets, clear P- and S-waves arrivals and a broad spectrum (5-15 Hz) (Figure 2.65a,b). Based on these features we consider them to be earthquakes (most of them are reported in the Northern California Earthquake catalog). The second group has 144 events. They have emergent onsets, low overall amplitudes, generally higher amplitudes on the horizontal components than on the vertical, and a narrow spectrum enriched in low frequencies (below 8 Hz; Figure 2.65c,d).

While the azimuths, from the plunges of the best fit planes, for the first group are scattered, those of the sec-

ond group are nearly constant (Figure 2.66a,b). Their direction is roughly consistent with the location of the tremor source reported in *Nadeau and Dolenc* (2005).

28.4 Conclusion

By developing an effective detection procedure, we were able to find two different groups of events in the seismic signal recorded during 48 episodes of NVT. The first family are earthquakes, most of which are reported in the NCSN catalog. The second was composed of tremor pulses, characterised by spectral content similar to the NVT and constant at all the stations, and by steady azimuth of seismic wave propagation, consistent with the location of the NVT source.

28.5 References

- Nadeau, R.M., and D. Dolenc, Nonvolcanic tremors deep beneath the San Andreas fault, *Science*, 307, doi:10.1126/science.1107142, 2005.
- Obara, K., Nonvolcanic deep tremor associated with subduction in southwest Japan, *Science*, 296, 1679-1681, 2002.
- Shelly, D.R., Beroza, G.C., Ide, S., and S. Nakamura, Low-frequency earthquakes in Shikoku, Japan, and their relationship to episodic tremor and slip, *Nature*, 442, 188-191, 2006.
- Shelly, D.R., Beroza, G.C., and S. Ide, Non-volcanic tremor and low-frequency earthquake swarms, *Nature*, 446, 305, 2007.
- Schwartz, S.Y., and J.M. Rokosky, Slow slip events and seismic tremor at circum-Pacific subduction zones, *Rev. Geophys.*, 45, RG3004, doi:10.1029/2006RG000208, 2007.
- Withers, M., Aster, R., Young, C., Beiriger, J., Harris, M., Moore, S., and J. Trujillo, A comparison of select trigger algorithms for automated global seismic phase and event detection. *Bull. Seism. Soc. Am.*, 88, 95-10, 1998.

29. Apparent Stress and Corner Frequency Variations in the 1999 Taiwan (Chi-Chi) Sequence

Kevin Mayeda and Luca Malagnini

29.1 Introduction

Apparent stress drop and corner frequency are measured for the Chi-Chi, Taiwan sequence beginning with the mainshock ($M_w 7.6$) on 20 September 1999. Using the recent coda source ratio methodology introduced by *Mayeda et al.* [2007], we have obtained stable source ratio estimates using broadband local and regional stations on Taiwan. We find the following: (1) For the mainshock and 7 of the larger aftershocks ($>M_w 5.5$), apparent stress is tightly clustered around 6 bars (± 2 bars); (2) In contrast, events below moment magnitude $\sim M_w 5.0$ exhibit lower average apparent stress as well as larger scatter, ranging between ~ 1.0 and 7.0 bars and are spatially variable; 3) For this dataset, the *Brune* [1970] omega-square source model fits the spectral shape for events $4.5 < M_w < 7.6$; however, a clear, step-wise break in self-similarity exists at around $M_w 5.0$. We hypothesize that the larger events are subject to the average state-of-stress over a broader region, whereas the smaller aftershocks are more sensitive to the local state-of-stress resulting from stress-field redistribution following the mainshock.

29.2 Earthquake Source Scaling

Aside from long-period regional and teleseismic waveform modeling estimates for M_w , broadband studies that extrapolate back to the source have always been hampered by inadequate knowledge of scale-dependent path and site effects. Radiated energy and corner frequency estimation over a broad range of event sizes requires significant frequency-dependent corrections, resulting in significant error that makes interpretation of the results highly questionable. There are, however, a number of local and regional methods that circumvent the problem of path and site corrections, namely the empirical Greens function deconvolution method [e.g., *Hough*, 1997] and amplitude ratio techniques [e.g., *Izutani*, 2005]. These approaches have gained popularity because adjacent or co-located events recorded at common stations have shared path and site effects, which therefore cancel. In this study we use a variant of the direct wave amplitude ratio, the coda ratio methodology of *Mayeda et al.* [2007], which has been shown to be roughly 3 times more stable than direct wave ratios and can be used with event pairs that are separated by several tens of kilometers, with little ill effects on data scatter. More recently, the method has been extended to datasets in Italy such as the San Giuliano di Puglia sequence in October 2001 [*Malagnini and Mayeda*, 2008] and the Colfiorito sequence of 1997 and

1998 [*Malagnini et al.*, 2008]. Over the past decade, a number of studies have suggested that earthquake scaling is either constant with high scatter or increases with increasing magnitude. Due to large errors and regional variations, it has been difficult to definitively tell which of these two ideas is correct. Knowledge of scaling, whether self-similar or not, is fundamental to earthquake rupture simulations and seismic hazard prediction, especially if there exist region-dependent variations in apparent stress.

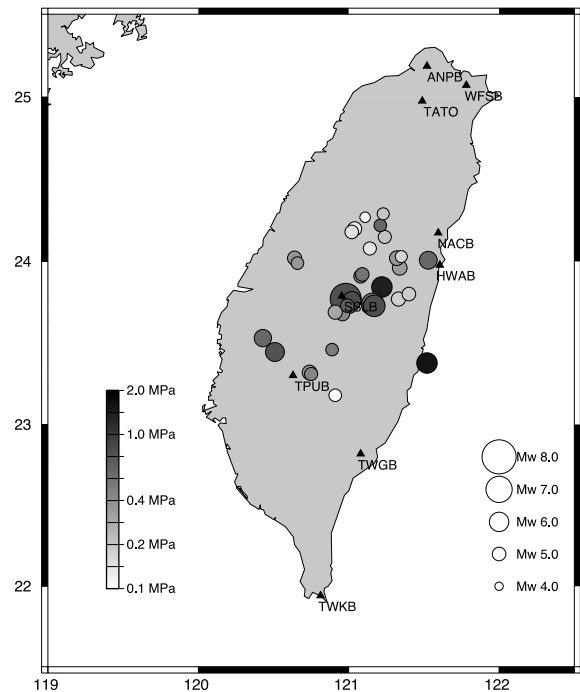


Figure 2.67: Map showing epicenters of events used in this study (circles) and broadband stations (triangles). Shading of events corresponds to the average apparent stress that was computed from the coda envelope ratios for each event.

29.3 Application to Chi-Chi, Taiwan Sequence

For this study, we selected 43 events ranging between $M_w 4.4$ and 7.6 recorded by 9 stations of the Broadband Array in Taiwan (BATS) (Figure 2.67). Stable M_w s for all the events were obtained from a previous coda calibration. The coda ratio methodology is outlined in *Mayeda*

et al. [2007], so we only give a brief processing description here. First, narrowband time-domain envelopes ranging between 0.03 and 8.0-Hz were made using the two horizontal components and log-averaged for additional stability and smoothed. Coda synthetic envelopes were then fit to the data for each station so that relative amplitudes could be measured using an L-1 fitting routine for each narrowband envelope. Then ratios were formed for all possible event pairs by subtracting the log10 amplitudes for each station that recorded the event pair. Observed ratios were then fit by theoretical ratios derived from a modified *Brune* source spectra outlined in *Walter and Taylor*, [2001]. Figure 2.68 shows corner frequency estimates along with ± 1 standard deviation, and their corresponding apparent stress drops are shown in Figure 2.67. As found in other studies, the coda-derived source ratios exhibited little scatter, and thus source parameters, such as corner frequency, are well constrained when we fit the observed data with theoretical source models. The averaging nature of coda waves has been shown to provide significantly lower amplitude variance than any traditional direct phase method. We have obtained stable source ratio estimates using broadband local and regional stations on Taiwan. We find the following: (1) For the mainshock and 7 of the larger aftershocks ($> M_w$ 5.5), apparent stress is tightly clustered around 6 bars (± 2 bars); (2) In contrast, events below moment magnitude $\sim M_w$ 5.0 exhibit lower average apparent stress as well as larger scatter, ranging between ~ 1.0 and 7.0 bars, and are spatially variable; 3) For this dataset, the *Brune* [1970] omega-square source model fits the spectral shape for events $4.5 < M_w < 7.6$; however, a clear, step-wise break in self-similarity exists at around M_w 5.0. We hypothesize that the larger events are subject to the average state-of-stress over a broader region, whereas the smaller aftershocks are more sensitive to the local state-of-stress resulting from stress-field redistribution following the mainshock.

29.4 Acknowledgements

K. Mayeda was supported under Weston Geophysical subcontract No. GC19762NGD and AFRL contract No. FA8718-06-C-0024. Work by L. Malagnini was performed under the auspices of the Dipartimento della Protezione Civile, under contract S4, ProCiv-INGV (2004-06), project: "Stima dello scuotimento in tempo reale e quasi-reale per terremoti significativi in territorio nazionale".

29.5 References

Brune, J. N., Tectonic stress and spectra of seismic shear waves from earthquakes, *J. Geophys. Res.* 75, 4997-5009, 1970.

Hough, S.E., Empirical Greens function analysis: Taking the next step, *J. Geophys. Res.* 102, 5369-5384, 1997.

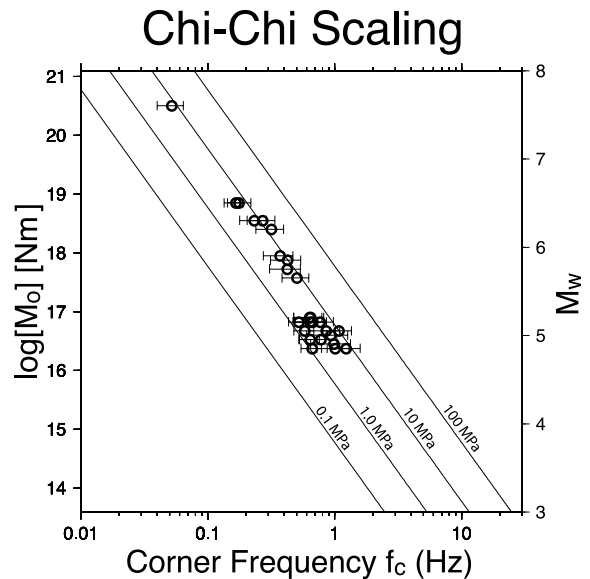


Figure 2.68: Moment versus corner frequency is plotted for the Chi-Chi sequence with lines of constant apparent stress. In general, the mainshock and larger aftershocks above M_w 5.5 have roughly the same scaling and apparent stress values, whereas for smaller events there is a clear shift and more scatter.

Izutani, Y., Radiated energy from the mid Niigata, Japan, earthquake of October 23, 2004 and its aftershocks, *Geophys. Res. Lett.* 32, L21313, doi:10.1029/2005GL024116, 2005.

Malagnini, L. and K. Mayeda, High-stress strike-slip faults in the Apennines: An example from the 2002 San Giuliano earthquakes (Southern Italy), *Geophys. Res. Lett.*, doi:10.1029/2008GL034024, 2008.

Malagnini, L., L. Scognamiglio, A. Mercuri, A. Akinci, K. Mayeda, Source scaling for ground motion prediction in central Italy: Evidence for strong non-self-similar behavior, accepted *Geophys. Res. Lett.*, 2008.

Mayeda, K., L. Malagnini, W.R. Walter, A new spectral ratio method using narrow band coda envelopes: Evidence for non-self-similarity in the Hector Mine sequence, *Geophys. Res. Lett.*, doi:10.1029/2007GL030041, 2007.

Walter, W. R. and S. R. Taylor (2001). A revised magnitude and distance amplitude correction (MDAC2) procedure for regional seismic discriminants: theory and testing at NTS, Lawrence Livermore National Laboratory Report, UCRL-ID-146882, <http://www.llnl.gov/tid/lof/documents/pdf/240563.pdf>

30. Source Analysis of the Crandall Canyon, Utah, Mine Collapse

Sean R. Ford, Douglas S. Dreger, William R. Walter (Lawrence Livermore National Laboratory)

30.1 Introduction

On 6 August 2007 a magnitude 3.9 seismic event was associated with the tragic collapse of a Utah coal mine, which ultimately killed six miners and three rescue workers. The event was recorded on the local network of the University of Utah Seismic Stations (UUSS) and the Advanced National Seismic System (ANSS) operated by the USGS. In addition, the NSF Earthscope USAarray stations had recently been installed in the region (www.earthscope.org). These stations provided good coverage (Figure 2.69a) enabling seismic source analysis of the recorded signals, which revealed an unusually shallow depth and anomalous radiation pattern, both contrary to the expectation for a tectonic earthquake.

30.2 Results

First motion polarities from vertical-component records of the seismic event are down, or dilatational, indicative of an implosional source (*Pechmann et al.*, 2008). Consistent with this observation, the moment tensor inversion of complete, three-component, low-frequency (0.02 to 0.10 Hz) ground displacement recovered a mechanism that also satisfies the observed first motions, and is most consistent with the gravity driven vertical collapse of a horizontally oriented underground cavity at a shallow depth consistent with the mine workings (Figure 2.69b). The total seismic moment of this mechanism was 1.91×10^{15} N-m ($M_W 4.2$). However, a closing horizontal crack theoretically has no Love wave excitation and in order to explain the large amplitude Love waves observed on the tangential component (Figure 2.69c) the mechanism must contain a secondary non-crack component that is 24% of the dominant vertical collapse moment (1.71×10^{15} N-m). The secondary source excitation of the moment tensor can be represented in multiple ways, as the moment tensor decomposition is non-unique (*Jost et al.*, 1989). Plausible interpretations of the secondary source include additional vertical dip-slip faulting, horizontal shear, non-uniform crack closure, and elastic relaxation in response to the mine collapse.

The source-type diagram (*Hudson et al.*, 1989) in Figure 2.69b illustrates the deviation from a pure earthquake double-couple (DC) source at the center in terms of a volumetric component (explosion or implosion) on the ordinate, and deviatoric component in terms of a volume compensated linear vector dipole (CLVD) on the abscissa. The moment tensor solution for the 6 August 2007 event plots in the region of a negative or closing crack. The diagram shows that despite the secondary

source component the seismic waveforms are best fit by a model that is primarily comprised of a closing horizontal crack, or underground collapse, and is similar to solutions obtained for other mine and Nevada Test Site (NTS) cavity collapses (*Ford et al.*, 2008). In contrast, NTS nuclear explosions modeled with the same method (*Ford et al.*, 2008) plot squarely in the explosion region of the diagram. Both the explosions and collapses are significantly separated from the population of earthquakes, which locate in the center of the diagram. Deviation from pure DC mechanisms in the earthquake population can be a result of several factors including complex faulting, noise, and the effect of approximate Earth structure models on the basis Greens functions for the inversion. Despite the scatter within the three source populations, there is clear separation between each, indicating that regional distance seismic moment tensor methods are capable of source-type discrimination.

30.3 Conclusions

Our findings show that the seismic waveforms associated with the mine collapse primarily reflect the collapse; however, the seismic source process was more complex than observed in other collapse events (*Pechmann et al.*, 1995) with a large secondary source generating strong Love waves. This application of seismic moment tensor analysis demonstrates the feasibility of continuous monitoring of regional distance seismic wavefields for source-type identification including nuclear explosion monitoring and given rapid access to the seismic waveform data, for emergency response applications.

30.4 Acknowledgements

Sponsored by National Nuclear Security Administration, Office of Nonproliferation Research and Development, Office of Defense, Nuclear Nonproliferation. Contract No. DE FC52-06NA27324. We thank Bruce Julian for the code to make the source-type plots.

30.5 References

- Ford, S., D. Dreger and W. Walter (2008). Identifying isotropic events using a regional moment tensor inversion, accepted by *J. Geophys. Res.*
- Jost, M. L. and R. B. Herrmann (1989). A student's guide to and review of moment tensors, *Seismol. Res. Lett.*, 60 2, 37-57.

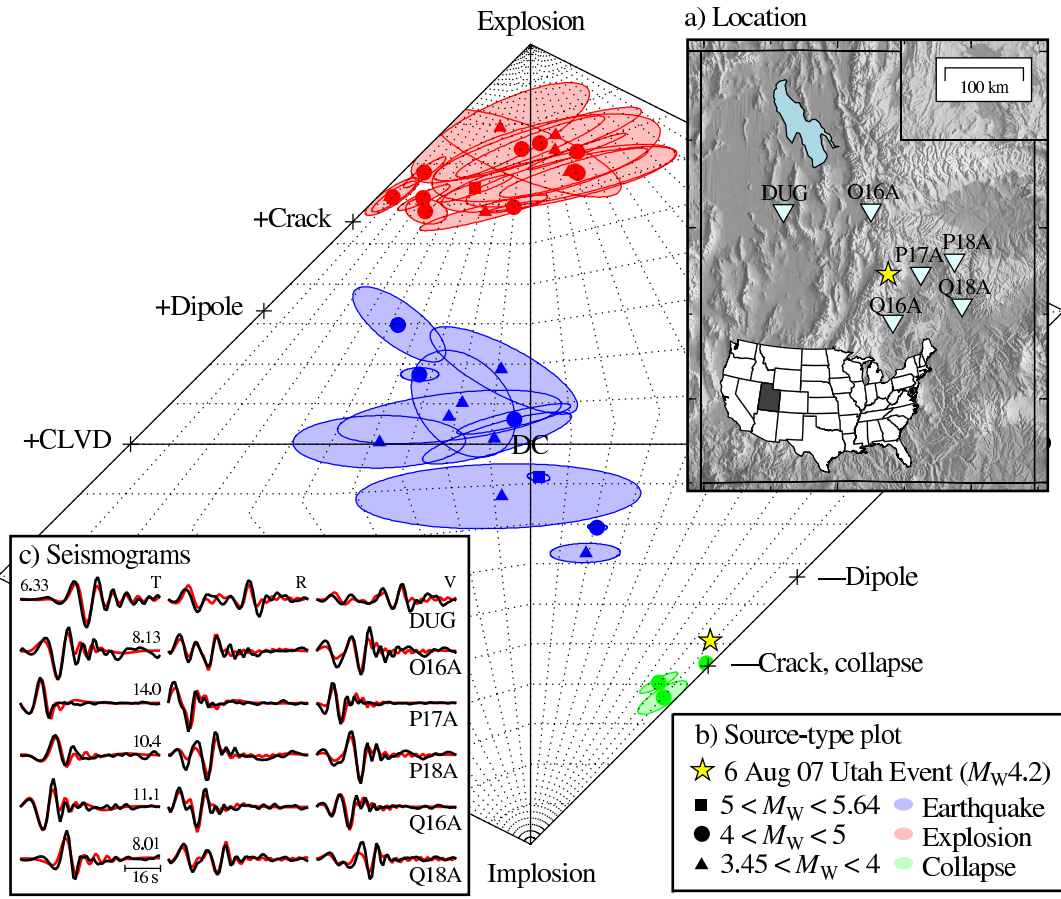


Figure 2.69: a) Locations of the August 6, 2007 event and 6 of the closest USArray and ANSS stations. b) Source type plot from the method of Hudson *et al* (1989) shows clear separation of populations of earthquakes, explosions and collapses. The yellow star shows the solution for the August 6, 2007 seismic event. c) Observed seismograms (black) are compared to synthetics (red) for the non-double-couple solution, which is dominated by a horizontal closing crack (b). The maximum displacement (10^{-7} m) of each set of tangential (T), radial (R), and vertical (V) observations is given. (See color version of this figure at the front of the research chapter.)

Hudson, J. A., R. G. Pearce, R. G., and R. M. Rogers (1989). Source type plot for inversion of the moment tensor, *J. Geophys. Res.*, 9 (B1), 765-774.

Pechmann, J. C., W. J. Arabasz, K. L. Pankow, R. Burlacu, and M. K. McCarter (2008), Seismological report on the 6 Aug 2007 Crandall Canyon Mine collapse in Utah, *Seism Res. Lett.*, 79 5, 10-12.

Pechmann, J. C., W. R. Walter, S. J. Nava, and W. J. Arabasz (1995). The February 3, 1995, ML 5.1 seismic event in the trona mining district of southwestern Wyoming, *Seism. Res. Lett.*, 66 3, 25-34.

31. Interactions Between Early Earthquake Slip History and Final Magnitude

Gilead Wurman, Richard M. Allen and David D. Oglesby (University of California, Riverside)

31.1 Introduction

One commonly accepted model for the behavior of fault ruptures is the cascading rupture model [Bak and Tang, 1989; Steacy and McCloskey, 1998; Ide and Aochi, 2005; Otsuki and Dilov, 2005; Sato and Mori, 2006], which describes a cascading failure of successive fault patches as a result of loading by the rupture of preceding patches. Because the rupture of a given patch is unaffected by those patches ahead of the rupture front, this model predicts that earthquakes should be non-deterministic for the duration of their rupture. That is, there should be no discernible information about the extent of the final rupture until it has completely finished propagating.

Recent observations of the spectral character of P-waves [Olson and Allen, 2005; Lockman and Allen, 2005, 2007; Wurman et al., 2007; Lewis and Ben-Zion, 2007] suggest that there is some information in the early seismic arrivals that may be correlated to the final magnitude of the event, and that in many cases this information is available before the rupture has completed. These data suggest that there may be an additional effect which is not accounted for by the cascading rupture model, which lends the rupture at least a degree of determinism.

Olson and Allen [2005] hypothesized that this determinism is provided by the intensity of the early rupture history of the earthquake. A higher stress concentration at the focus of the earthquake generates a stronger early rupture phase, which imparts sufficient energy to the rupture to overcome barriers on the fault surface and produce a large earthquake. Conversely, an area of lower stress around the focus generates a comparatively weak early rupture, and the rupture may not gain enough energy to overcome the same barriers, and stops before becoming a large earthquake. Henceforth we use the term “nucleation” to describe the early dynamic (radiative) rupture history of the event, rather than a long-term (quasistatic) aseismic nucleation.

31.2 Model setup

We test this concept by modeling the dynamics of a planar fault with stochastic initial stress conditions, with systematically varying stress in the nucleation region. We use the Support Operators Rupture Dynamics (SORD) dynamic fault code [Ely et al., 2008]. The initial shear stress field is generated randomly using the method of Ripperger et al. [2007]. One realization of an initial stress field is shown in Figure 2.70a.

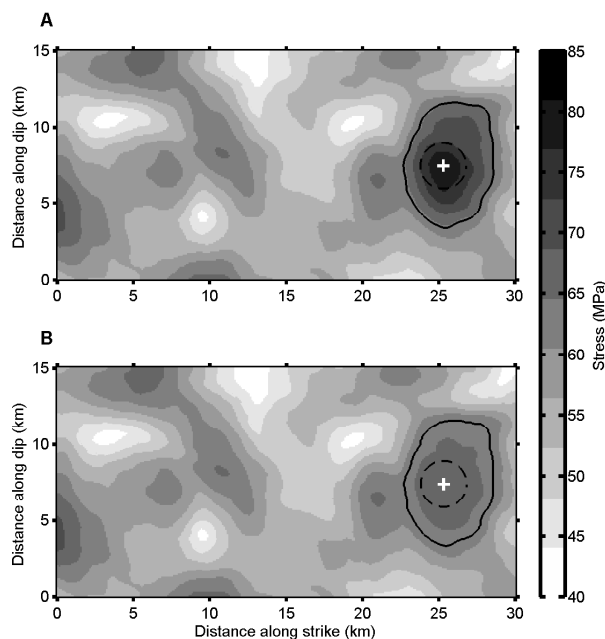


Figure 2.70: Initial distribution of shear stress on the fault plane, with high nucleation stress (a) and reduced nucleation stress (b). Dashed black circle represents region of forced nucleation, with black + marking nucleation point. Black solid contour shows region of nucleation stress scaling, and white dashed contours show regions where initial shear stress is less than dynamic yield stress.

We select an appropriate nucleation point by examining the asperities in our stress realization and selecting the highest-stress asperity on the fault that is broad enough to accommodate the 3 km diameter of the nucleation zone. To simulate varying nucleation stresses, we take a contour around the nucleation point at 64 MPa, approximately halfway between static and dynamic yield stress. Within that contour, we scale the stresses up or down such that the maximum stress is between 64 MPa and 80 MPa as desired. This process provides strong differences in the strength of nucleation, while largely preserving the spatial characteristics of the stress field. Outside the 64 MPa contour, the stress field remains identical between model runs. Figure 2.70b shows the stress field for the same realization as in Figure 2.70a, but with a weak nucleation.

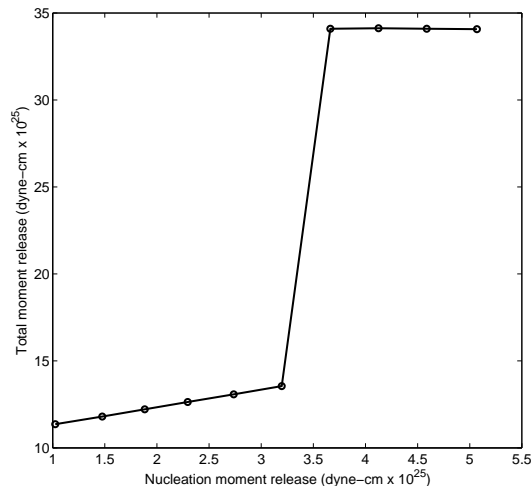


Figure 2.71: Total moment release vs. moment released in the first 2 seconds of rupture.

31.3 Results

We vary the peak nucleation stress between 64 and 80 MPa in increments of 1.6 MPa and allow the rupture to propagate to completion. We consider the moment release of the nucleation phase to be all moment released within the first 2 seconds of the rupture. This allows time for the effects of artificial nucleation to end, as well as for the rupture to propagate across the region of scaled nucleation stress. Figure 2.71 shows the total moment release in each run as a function of the nucleation moment release. Seismic moment is calculated at each element as $M_0 = \mu SD$, where D is the slip in cm at the element, S is the area of each element, 10^8 cm^2 , and $\mu = 3 \times 10^{11} \text{ dynes/cm}^2$. The total moment release is the sum of the moment at all nodes on the fault plane.

Figure 2.72 shows the final stress distribution and final slip on the fault for a high-stress nucleation case (80 MPa peak stress, 2.72a and 2.72c) and a low-stress case (65.6 MPa peak stress, 2.72b and 2.72d). A comparison of these figures to Figures 2.70a and b and the plot in Figure 2.71 shows that there is a point at which the initial nucleation is strong enough to overcome the low-stress barrier in the middle of the fault, and the rupture propagates through to the asperity on the other side. The behavior exhibited in this example is highly sensitive to the parameterization of the initial stress distribution. A distribution with slightly higher minimum shear stress will rupture through the entire fault for all initial conditions, while a distribution with lower minimum shear stress will never proceed past the nucleation asperity. This entire range is observed over a variation of less than 0.5 MPa in minimum initial shear stress.

31.4 Discussion and Conclusions

Because the moment release after 2 seconds of rupture can be correlated to the moment release at the end of the rupture, this model supports the concept of determinism in the rupture resulting from the strength of the nucleation phase. However, the rupture area in this realization has only two asperities and one barrier, which does not demonstrate that this behavior can extend to more heterogeneous faults. Because barriers require additional crack energy to propagate through, they reduce the available energy for the continuation of the rupture on the other side of the barrier.

The behavior presented here is only stable for a narrow range of stress parameters. It is particularly sensitive to the degree to which stresses on the fault plane are allowed to be less than the dynamic yield stress. Thus, only finely-tuned stress parameters create faults whose modeled behavior explains the observations of determinism in real earthquakes. If we regard the observations of earthquake scaling as reliable, and the mechanism shown in this study is responsible for the observed scaling behavior, our results may serve to constrain the possible state of in situ stress in real faults. However, this result is dependent on the methodology we use with regard to how we vary the intensity of nucleation. A different choice in terms of frictional parameterization, such as rate-and-state weakening, or spatially varying friction coefficients, may also have an effect on the range of possible initial shear stresses. Even within the bounds of the method used in this study, other realizations of initial stress conditions will also produce slightly varying results. Indeed, given the dearth of observations of stress on real faults, it is difficult to know what a reasonable state of initial shear stress is to begin with. A suite of models and stress patterns will provide a greater understanding of the state of stress on real faults.

31.5 Acknowledgements

The authors thank Luis Dalguer and Geoff Ely for assistance with dynamic rupture codes. This work was partially supported by USGS NEHRP Grant 06HQAG0147.

31.6 References

Bak, P. and C. Tang, Earthquakes as a Self-Organized Critical Phenomenon, *J. Geophys. Res. B*, *94*, 15635-15637, 1989.

Ely, G.P., S.M. Day, and J.B. Minster, A support-operator method for viscoelastic wave modeling in 3-D heterogeneous media, *Geophys. J. Int.* *172*, 331-344, 2008.

Ide, S. and H. Aochi, Earthquakes as multiscale dynamic ruptures with heterogeneous fracture surface energy, *J. Geophys. Res. B*, *110*, B11303, doi:10.1029/2004JB003591, 2005.

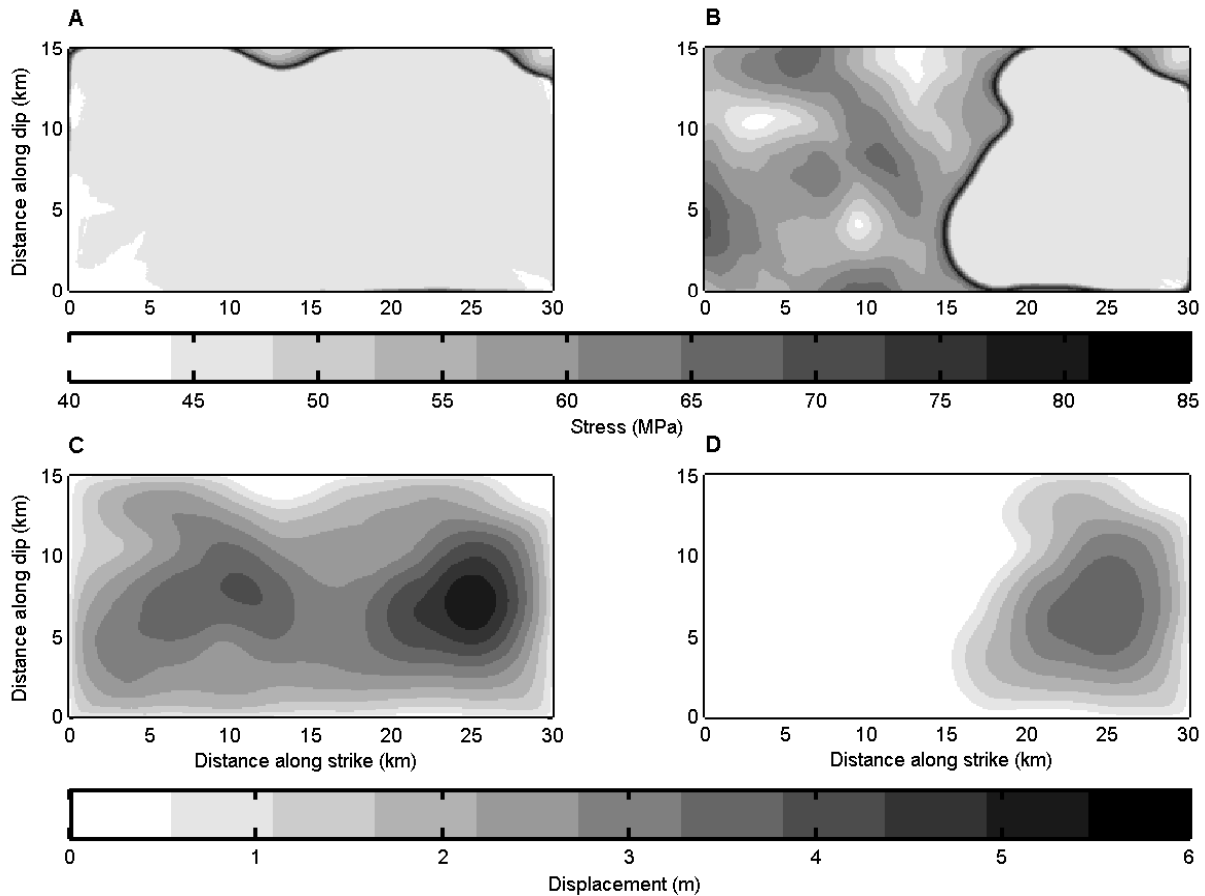


Figure 2.72: Final shear stress and final slip for the low-stress nucleation case (a,c) and the high-stress nucleation case (b,d). In the high-stress case, the rupture propagated through the barrier in the middle of the model, and in the low-stress case it was arrested at that barrier.

Lewis, M.A. and Y. Ben-Zion, Examination of scaling between proposed early signals in P waveforms and earthquake magnitudes, *Geophys. J. Int.*, 171, 1258-1268, 2007.

Lockman, A.B. and R.M. Allen, Single-station earthquake characterization for early warning, *Bull. Seism. Soc. Am.*, 95, 2029-2039, 2005.

Lockman, A.B. and R.M. Allen, Magnitude-period scaling relations for Japan and the Pacific Northwest: Implications for earthquake early warning, *Bull. Seism. Soc. Am.*, 97, 140-150, 2007.

Olson, E.L. and R.M. Allen, The deterministic nature of earthquake rupture, *Nature*, 438, 212-215, doi:10.1038/nature04214, 2005.

Otsuki, K and T. Dilov, Evolution of hierarchical self-similar geometry of experimental fault zones: Implications for seismic nucleation and earthquake size, *J. Geophys. Res. B.*, 110, B03303, doi:10.1029/2004JB003359, 2005.

Ripperger, J, J.-P. Ampuero, P.M. Mai, and D. Giardini, Earthquake Source Characteristics from Dy-

namic Rupture with Constrained Stochastic Fault Stress, *J. Geophys. Res. B.*, 112, B04311, doi:10.1029/2006JB004515, 2007.

Sato, K. and J. Mori, Scaling relationship of initiations for moderate to large earthquakes, *J. Geophys. Res. B.*, 111, B05306, doi:10.1029/2005JB003613, 2006.

Steady, S.J. and J. McCloskey, What controls an earthquake's size? Results from a heterogeneous cellular automaton, *Geophys. J. Int.*, 133, F11-F14, 1998.

Wurman, G., R.M. Allen, and P. Lombard, Toward Earthquake Early Warning in Northern California, *J. Geophys. Res. B.*, 112, B08311, doi:10.1029/2006JB004830, 2007.

32. Correlated Changes in Nonvolcanic Tremor, Seismic Velocity and Fault Displacement Associated with the 2003 San Simeon and 2004 Parkfield Earthquakes.

R.M. Nadeau, F. Brenguier^{1,2} M. Campillo² C. Hadziioannou² N.M. Shapiro,¹ E. Larose²

¹ (Sismologie, Institut de Physique du Globe de Paris & CNRS, Paris, France)

² (Laboratoire de Geophysique Interne et Tectonophysique & CNRS, Grenoble, France)

32.1 Introduction

Since their discovery in 2002 (*Obara, 2002*), deep (\sim 15-40 km) nonvolcanic tremors (long-duration seismic signals with no clear P or S waves) have generally been found in transition zones between freely slipping and locked fault (*Rogers and Dragert, 2003; Nadeau and Dolenc, 2005; Brudzinski and Allen, 2007; Payero et al., 2008*). In most cases, the tremors occur in subduction zones; hence, fluids from dehydration processes are believed to play an important role in tremor generation. Changes in the rate of tremor activity also often correlate with transient fault deformation (slow-slip events) and with dynamic stress changes from tides and surface waves of teleseismic (distant) earthquakes (*Gomberg et al., 2007, Rubinstein et al., 2008*).

These associations suggest that a better understanding of the mechanisms responsible for tremors may provide important clues to the rheology of deep fault zones and processes responsible for generating large earthquakes. Reported here is a recently discovered correlation between changes in nonvolcanic tremor activity and changes in seismic velocity and fault deformation along the central San Andreas fault occurring conjunctively with the 22 December 2003, M6.5 San Simeon and 28 September 2004, M6.0 Parkfield earthquakes (*Brenguier et al., 2008b*).

32.2 Continuous Borehole Seismic Data

To monitor variations in seismic velocities and nonvolcanic tremor, we analyzed more than 5 years (January, 2002 to October, 2007) of continuous seismic data from the 13 borehole seismic stations of the Berkeley High Resolution Seismic Network (HRSN). The analyses also spanned the two strongest earthquakes occurring within 100 km of Parkfield, CA: the $M_w = 6.5$ San Simeon Earthquake of 22 December 2003, whose epicenter was located 60 km west of Parkfield, and the $M_w = 6.0$ Parkfield Earthquake of 28 September 2004. Sensor depths of the HRSN stations range between 60 and 300 m, thus reducing locally generated noise and effects of temperature variations and precipitation.

32.3 Data Sets

Seismic Velocity Change

For every possible pair combination of stations we computed the daily cross-correlation of seismic noise using

the procedure of (*Brenguier et al., 2007*), yielding 91 x 2140 days = 194,740 cross-correlation and autocorrelation time functions. A Reference Green Function (RGF) was computed for each station pair by stacking the daily cross-correlations for the entire 2140 day period (*Brenguier et al., 2008b*). The velocity changes were then determined by measuring time delays between the RGF and 30 day stacks of cross-correlation functions in the frequency range 0.1 to 0.9 Hz (*Brenguier et al., 2008a, 2008b*). By measuring the slope of the travel time shifts, dt , as function of time, t , we then estimated the relative time perturbation (dt/t), which is the opposite value of the medium's relative velocity change (dv/v). Finally, following *Brenguier et al. (2008a)*, we averaged the relative time delays over all station pairs to increase the measurement accuracy.

Tremor Activity

During the study period, 1577 tremor events ranging in duration from 3 to 21 minutes were detected using 3 to 8 Hz filtered continuous records from the HRSN and root-mean-square envelope techniques (*Obara, 2002; Brenguier et al., 2008b*). In total, 8962 minutes of tremor activity was detected. These tremors are estimated to have occurred between 20 and 40 km depth, indicating that they are related to deep processes along the fault zone (*Nadeau and Dolenc, 2005*). A 30 day averaged rate history of tremor activity was then generated from these data for comparison to the seismic velocity and deformation data (Figure 2.73).

Surface Deformation

Surface deformation measurements used in this study (primarily GPS) were obtained over the internet from the USGS web site and selected and processed as described in *Brenguier et al. (2008b)*. More detail concerning the USGS deformation and GPS networks and related surface deformation measurements can be found at, <http://earthquake.usgs.gov/research/parkfield/deform.php> and http://quake.usgs.gov/research/deformation/twocolor/pkf_continuous_gps.html.

32.4 Results

The correlated evolution of the nonvolcanic tremors, seismic velocities, and fault zone deformation suggests

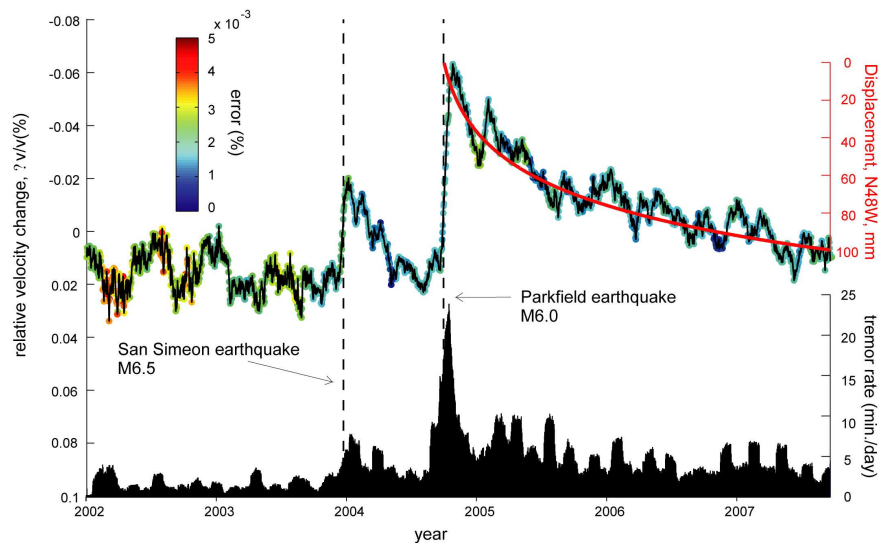


Figure 2.73: Seismic velocity changes (upper time history), surface displacements from GPS (upper, curve following Parkfield event) and tremor activity (lower time history) near Parkfield. The displacement curve represents the postseismic fault parallel displacements along the San Andreas fault as measured by GPS at station POMM. The tremor rates are averaged over a centered 30 day moving time window.

the presence of two physical mechanisms generating changes in crustal and fault zone properties: 1) shallow damage within the fault zone and near surface layers from strong ground shaking by the mainshocks and 2) coseismic stress change and postseismic relaxation extending down to nonvolcanic tremor depths (~ 30 km). The results also demonstrate that measurements of velocity change from seismic noise analysis can be useful for studying the continuous time evolution of stress in the vicinity of seismogenic faults and tremor zones.

32.5 Acknowledgements

The HRSN is funded by USGS grant 07HQAG0014. Research support was from ANR (France) under 05CATT01001, PRECORIS, ANR06-CEXC005, and COHERSIS, from NSF under EAR0537641 and EAR0544730 and from USGS grant 06HQGR0167.

This collaboration arose from discussions at the 2nd joint BSL/IPGP workshop on Seismology and Seismotectonics: BSL and IPGP research perspectives, held at Berkeley Seismological Laboratory (BSL) on December 16-17, 2007 and co-sponsored by BSL and the Project International de Cooperation Scientifique (PICS) awarded to the 'Departement de Sismologie' at the 'Institut de Physique du Globe de Paris' (IPGP).

32.6 References

Brenguier F., N.M. Shapiro, M. Campillo, A. Nercessian, V. Ferrazzini, 3-D surface wave tomography of the Piton de la Fournaise volcano using seismic noise correlations, *Geophys. Res. Lett.*, *34*, L02305, doi:10.1029/2006GL028586, 2007.

Brenguier F., N.M. Shapiro, M. Campillo, V. Ferrazzini, Z. Duputel, O. Coutant, A. Nercessian, Towards forecasting volcanic eruptions using seismic noise, *Nature Geoscience*, *1*, 126-130, 2008a.

Brenguier F., M. Campillo, C. Hadziioannou, N.M. Shapiro, R.M. Nadeau and E. Larose, Postseismic Relaxation Along the San Andreas Fault at Parkfield from Continuous Seismological Observations, *Science*, *in press*, 2008b.

Brudzinski, M. and R.M. Allen, Segmentation in Episodic Tremor and Slip All Along Cascadia, *Geology*, *35*, 907-910, 2007.

Gomberg, J., J.L. Rubinstein, Z. Peng, K.C. Creager and J.E. Vidale, P. Bodin, Widespread Triggering of Non-Volcanic Tremor in California, *Science*, *319*, 173, 2008.

Nadeau, R.M. and D. Dolenc, Nonvolcanic Tremors Deep Beneath the San Andreas Fault, *Science*, *307*, 389, 2005.

Obara, K., Nonvolcanic Deep Tremor Associated with Subduction in Southwest Japan, *Science*, *296*, 1679-1681, 2002.

Payero, J. S., V. Kostoglodov, N. Shapiro, T. Mikumo, A. Iglesias, X. Peres-Campos and R. W. Clayton (2008), Nonvolcanic Tremor Observed in the Mexican Subduction Zone, *Geophys. Res. Lett.*, *35*, L07305, doi:10.1029/2007GRL32877, 2008.

Rogers, G. and H. Dragert, Episodic Tremor and Slip on the Cascadia Subduction Zone: The Chatter of Silent Slip, *Science*, *300*, 1942-1943, 2003.

Rubinstein, J. L., M. La Rocca, J.E. Vidale, K.C. Creager and A.G. Wech (2007), Tidal Modulation of Non-Volcanic Tremor, *Science*, *319*, 186-189, 2008.

33. Moderate earthquake ground motion validation in the San Francisco Bay Area

Ahyi Kim, Douglas Dreger, and Shawn Larsen

33.1 Introduction

We performed 3D ground motion simulations for 10 recent moderate earthquakes in the San Francisco Bay Area to evaluate the two versions of the USGS 3D velocity models. Comparisons were made in terms of modeling phase arrival timing, peak ground motion amplitudes, and general seismic waveforms. One model, version 5.1.0 was released in 2005 (Brocher *et al.*, 2005; Jachens *et al.*, 2006) and it was used by Rodgers *et al.* (2007) to simulate waveforms of moderate earthquakes in the San Francisco Bay Area in the low frequency band ($f < 0.25\text{Hz}$). Rodgers found that version 5.1.0 predicted the peak amplitude well but that energy arrived earlier than observed. The other model, version 8.3.0, was released in May 2008 (Brocher 2008), was used to simulate the ground motions for the 1906 San Francisco earthquake (Aagaard *et al.*, 2008b), and was validated by modeling the 1989 Loma Prieta earthquake strong ground motions (Aagaard *et al.*, 2008a). This model reduced both P- and S-wave velocities in granite, Franciscan, gabbro, lower crust, and upper mantle to correct the earlier phase arrival timing mismatch reported by Rodgers *et al.* (2007). We directly compared the two models in each 200m grid layer and found that the mean velocity of each layer was reduced by approximately 5% in the depth range from 5 to 30km in model 8.3.0.

33.2 Computational set up and 3D model used in the simulations

For the 3D waveform modeling, we used the elastic finite-difference code, E3D developed by Larsen and Schultz (1995). With the BSL cluster we can simulate ground motions throughout the greater San Francisco Bay Region to a maximum frequency of 0.5 Hz for models with a minimum wave speed of 500m/s. We have performed simulations of 9 Mw4.1-5.0 events using source parameters obtained from the BSL Moment Tensor Catalog (Table 2.1). Broadband seismic data was obtained from the Berkeley Digital Seismic Network (BDSN), and strong motion data was obtained from the USGS strong Motion Instrumentation Program (SMIP) and the California Geologic Survey (CGS) California Strong Motion Instrumentation Program (CSMIP). The data was corrected to absolute ground velocity (cm/s). We compare synthetic and observed ground velocity in three passbands, namely 0.03-0.15Hz, 0.1-0.25Hz, and 0.1-0.5Hz.

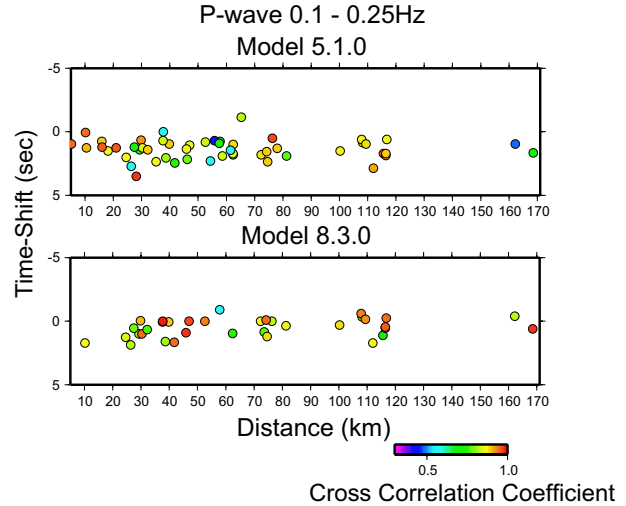


Figure 2.74: Top shows the relative time shift between synthetic and observed P-waves for model 5.1.0. Positive time shift means the synthetic is early and the model is fast. The color scale shows the level of cross-correlation of the synthetic and observed P waveforms. The bottom shows the same for model 8.3.0.

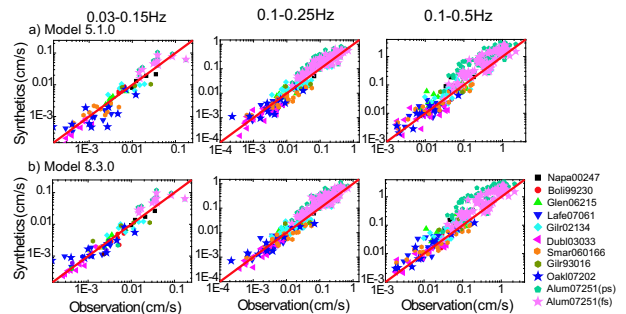


Figure 2.75: Top row shows the comparison between observed and synthetic PGV in three passbands, 0.03-0.15, 0.1-0.25, and 0.1-0.5 Hz for model 5.1.0. The bottom row shows the same for model 8.3.0. The symbols are for different simulated events. The corresponding legends are to the right.

33.3 Modeling results

We performed an analysis of P-wave arrival times by using cross-correlation to determine arrival time differences. For this analysis we low pass filtered the velocity records using an acausal Butterworth filter with corners of 0.1 and 0.5Hz, and then used waveform cross-

ID	Date	lon	lat	Strike	Dip	Rake	Depth	Moment	Mw
gilr93016	01/16/1993	-121.46	37.03	331	83	166	7	2.40E+23	4.9
boli99230	08/18/1999	-122.69	37.91	115	49	69	8	7.25E+22	4.5
napa00247	09/03/2000	-122.41	38.38	60	75	18	11	3.74E+23	5
gilr02134	05/14/2002	-121.6	36.97	212	87	-6	8	2.86E+23	4.9
dubl03033	02/02/2003	-121.94	37.74	67	88	-19	14	1.36E+22	4.1
smar06166	06/15/2006	-121.49	37.1	360	78	-152	5	4.18E+22	4.4
glen06215	08/03/2006	-122.59	38.36	256	86	19	5	5.64E+22	4.4
lafe07061	03/02/2007	-122.1	37.9	82	89	-1	14	2.77E+22	4.2
oakl07202	07/20/2007	-122.18	37.8	321	89	168	5	2.52E+22	4.2
alum07251	10/31/2007	-121.78	37.43	323	87	180	11	1.85E+24	5.4

Table 2.1: Earthquakes simulated in this study. Event ID and the source parameters are obtained from BSL Moment Tensor Catalog.

correlation to find the relative arrival times. We limited the synthetic to shift in time by plus or minus two seconds (for $f < 0.5\text{Hz}$) to avoid possible cycle skipping. As Figure 2.74 shows, consistent with *Rodgers et al.* (2007) for S-e arrival times, the P-wave arrival times for model 5.1.0 are systematically early. The arrival time difference increase with distance suggests it is a systematic error in the seismic wave speed, where P-wave velocity is too high. A recalculation using model 8.3.0 shows that the simulated arrivals are still a little early, but that most of the disagreement with the observations has been accounted for.

The comparison of Peak Ground Velocity (PGV) for both models 5.1.0 and 8.3.0 reveals that both 3D models predict the observed PGV well (Figure 2.75). The comparison shown is for over 4 orders of magnitude values exceeding 1 cm/s where damage begins to manifest in weak unreinforced structures. In the low frequency band (0.03 - 0.15Hz), all of the small events are essentially point-sources, and we see that there is very good one-to-one correspondence between observed and simulated PGV. Both models perform well, but model 8.3.0 seems to reduce the dispersion slightly. This is also true of the intermediate passband (0.1-0.25 Hz). At higher frequencies, the correlation remains good; however, unaccounted for source effects for the larger events, and 3D wave propagation and site conditions become more important, leading to higher dispersion in the predicted amplitudes. Since PGV seems to scale approximately linearly in large events (e.g. *Boore and Atkinson*, 2008; *Campbell and Bozorgnia*, 2008), and PGV in large events is carried by waves of 1 to several seconds period, well within the ranges of the passband of our simulations, the comparison strongly suggests that both 3D velocity models, and particularly model 8.3.0, are suitable for simulating strong ground motion scenarios for the region’s high risk faults. It is noted however that the comparison in Figure 2.75 is log-scale, and that the dispersion represents a factor of 2 to 4 in simulated motions. This fact should be considered in the interpretation of predictive

maps of scenario earthquake simulations (e.g. *Aagaard et al.*, 2008b). Finally, for the largest event that we considered, the 2007 Mw 5.4 Alum Rock earthquake, there can be significant differences in simulated PGV depending upon the assumed duration of the source. For this event, at most stations synthetic PGV is overestimated, which is due to the strong southwestward rupture directivity and the fact that most stations are located to the northwest of the epicenter. For this event, we also simulated the ground motions by including a uniform slip finite-source model with southeastward rupture. Using this simple finite-source model reduced the amplitude at stations located to the northwest of the epicenter and improved the overall PGV fit (Figure 2.75).

Although the PGV is relatively well explained, and in many cases the three component waveforms match that data well, there remain paths that could benefit from model refinement. In Figure 2.76a three component waveforms for the Bolinas earthquake are compared, and in all cases, except the paths to BDM and POTR, the fit is good. The paths to BDM and POTR are in the same general eastward direction, yet while the fit to the BDM record is much improved with the model 8.3.0, there remains significant misfit at POTR indicating unmodeled structure north of delta, and possibly in the San Pablo Bay. In Figure 2.76b for the 2002 Gilroy earthquake, the two closest stations have good agreement with the primary S waveform amplitudes, but the model fails to explain the large secondary surface wave train at station 1404 due to sediments in the Hollister and Salinas valleys. While the synthetics explain PGV at sites 1404 and 1854 within a factor of less than two (190% and 130%, respectively), they significantly under predict the duration of strong shaking.

33.4 References

Aagaard, B. T., T. M. Brocher, D. Dolenc, D. Dreger, R. W. Graves, S. Harmsen, S. Hartzell, S. Larsen, and M.L. Zoback, Ground-Motion Modeling of the 1906 San Francisco Earthquake, Part I: Validation Using the 1989

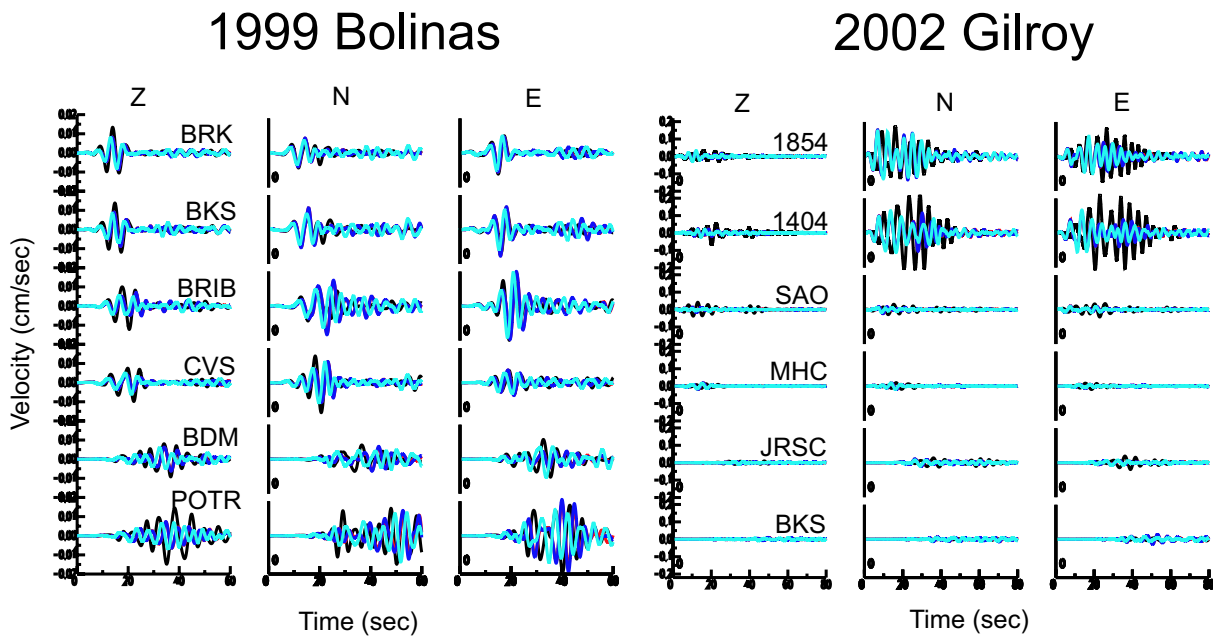


Figure 2.76: Three-component velocity waveforms (black) for 1999 Bolinas earthquake (a) and 2002 Gilroy earthquake (b) are compared to synthetics for models 5.1.0 (cyan) and 8.3.0 (blue). The data and synthetics have been bandpass filtered between 0.10 to 0.25Hz.

Loma Prieta Earthquake, *Bull. Seism. Soc. Am.*, 98, 989-1011, doi: 10.1785/0120060409,2008a.

Aagaard, B. T. M. Brocher, D. Dolenc, D. Dreger, R. W. Graves, S. Harmsen, S. Hartzell, S. Larsen, K. McCandless, S. Nilsson, N. A. Petersson, A. Rodgers, B. Sjogreen, and M. L. Zoback, Ground-Motion Modeling of the 1906 San Francisco Earthquake, Part II: Ground-Motion Estimates for the 1906 Earthquake and Scenario Events, *Bull. Seism. Soc. Am.*, 98, 1012-1046, doi: 10.1785/0120060410,2008b.

Boore, D. M. and G. M. Atkinson, Ground-motion prediction equations for the average horizontal component of PGA, PGV, and 5%-damped PSA at spectral periods between 0.01 s and 10.0 s, *Earthquake Spectra* 24, 99-138,2008.

Brocher, T. M., Empirical relations between elastic wave speeds and density in the Earth's crust, *Bull. Seism. Soc. Am.*, 95 No. 6, 2081-2092,2005.

Dreger D. and B. Romanowicz, Source Characteristics of Events in the San Francisco Bay Region, USGS open-file report, 94-176, 301-309, 1994.

Brocher, T., Compressional and Shear-wave velocity versus depth relations for common rock types in Northern California, *Bull. Seism. Soc. Am.*, 98 No. 2, 950 - 968, 2008.

Campbell, K. and Y. Bozorgnia, NGA Ground Motion Model for the Geometric Mean Horizontal Component of PGA, PGV, PGD and 5% Damped Linear Elastic Response Spectra for Periods Ranging from 0.01 to 10 s, *Earthquake Spectra* 24, 139-171,2008.

Jachens, R., R. Simpson, R. Graymer, C. Wentworth, T. Brocher, Three-dimensional geologic map of northern and central California: A basic model for supporting ground motion simulation and other predictive modeling, 2006 SSA meeting abstract, *Seism. Res. Lett.*, 77, No.2, p 270, 2006.

Larsen, S. and C. A. Shultz, ELAS3D: 2D/3D elastic finite-difference wave propagation code, Technical Report No. UCRL-MA-121792, 1995.

Rodgers A., N., A. Petersson, S. Nilsson, B. Sjogreen, and K. McCandless, Broadband waveform modeling of moderate earthquakes in the San Francisco Bay Area and preliminary assessment of the USGS 3D Seismic velocity model, *Bull. Seism. Soc. Am.*, 98 no. 2, 969-988, 2008.

34. Recalibrating M_L for CISN

Robert Uhrhammer, Margaret Hellweg, Pete Lombard, Kate Hutton (Caltech), Egill Hauksson (Caltech), Allan Walter (USGS Pasadena), Dave Oppenheimer (USGS Menlo Park)

34.1 Research Objectives

Richter (1935) and *Gutenberg and Richter* (1942) developed the local magnitude scale using Wood-Anderson seismographs. *Richter* (1935) defined “local” magnitude measured at a certain station as: $M_L = \log A - \log A_o(\Delta) + dM_L$. Here M_L is the local magnitude estimate; $\log A$ is the logarithm of the maximum trace amplitude A (in mm) recorded by a standard Wood-Anderson torsion seismograph; $\log A_o(\Delta)$ is the logarithm of a standard event of magnitude zero at the same epicentral distance Δ in km; and dM_L is the adjustment for that station. The M_L estimate for an event is then the arithmetic average of the individual estimates from the Wood-Anderson seismographs that recorded the event.

In the past thirty years, the instrumentation with which we measure earthquakes has changed, and we can now process the data digitally. Nonetheless, we would like to continue to assign events with local magnitudes which are consistent with those that have been calculated in Northern and Southern California in the past.

In 2006-2007, we reported the development of a new $\log A_o(\Delta)$, valid in all of California for hypocentral distances from 1 km to 500 km. In this year, agreement was reached on a set of station corrections, and the CISN M_L parameters were validated by comparing M_L values determined using the “new” and “old” systems.

34.2 Data Set

A set of approximately 100,000 waveforms from 255 candidate earthquakes recorded by 1160 horizontal channels (Station-Network-Channel-Location, or SNCL labels are used to describe each) from the AZ, BK, CI and NC networks was selected. The candidate events were selected from the CISN 2000-2006 seismicity by gridding the state into 50 km square bins. Two events were selected for each bin: the largest M_L 3+ event, and the largest M_L 3+ event in 2006 (or second largest if the largest 2000-2006 event in the bin occurred in 2006) to obtain adequate data USArray stations. The SNCL channels included both broadband and strong motion instruments. The data set was culled to remove events and SNCLs with fewer than 7 data each and to also remove data with event-SNCL distances greater than 500 km. Local magnitude (M_L) was calculated from each channel’s trace by deconvolving the instrument response and convolving the response of a Wood-Anderson seismograph (*Uhrhammer et al*, 1996). For each event, differences for all SNCL pairs were calculated, giving a dataset with more than 10 million differential observations. The

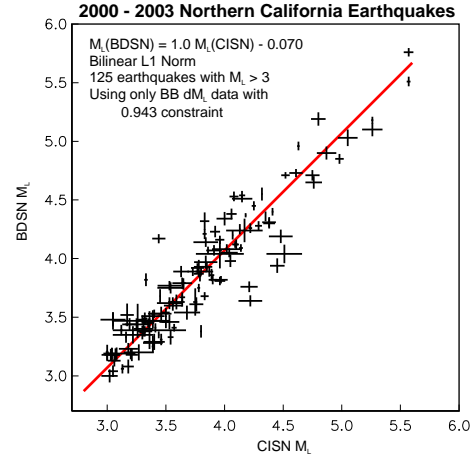


Figure 2.77: Comparison of M_L for Northern California (NC) earthquakes recorded in 2000-2003 determined using the new CISN function and with parameters currently used in NC. Uncertainties exist for both measurements and depend mainly on the number of SNCLs used in the calculation. The slope is close to 1 and the intercept close to 0, indicating good agreement.

differential data were inverted, via constrained linear least-squares with two constraints: (1) $\log A_o(100km) = -3$; and (2) the sum of the dM_L s for selected SNCLs with historical dM_L values = the sum of their historical dM_L values. This approach was taken to ensure consistency with past magnitudes determined in Northern and Southern California.

34.3 $\log A_o$ and SNCL dM_L s

The constrained linear least-squares perturbations to the $\log A_o$ function were found to be very stable and well represented by a sixth order Chebyshev polynomial at hypocentral distances from 8 km to 500 km hypocentral distance. At shorter distances, it is approximated by a line with a slope close to 2. This $\log A_o$ form was adopted and an algorithm was developed and used in the subsequent inversions for the dM_L SNCL adjustments. The dM_L s for the broadband SNCLs were then determined and found to be acceptable for the colocated strong motion sensors as well.

To assess the consistency of the CISN M_L with existing M_L s, we performed three comparisons. In Figure 2.77, M_L values taken from the Northern California database are compared against CISN M_L determined for

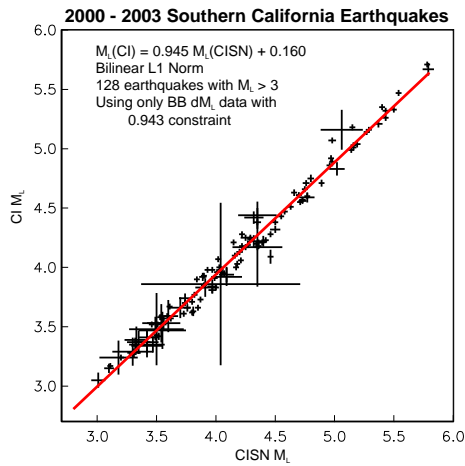


Figure 2.78: Comparison of M_L for Southern California (SC) earthquakes recorded in 2000-2003 determined using the new CISM function and with parameters currently used in SC. Uncertainties exist for both measurements and depend mainly on the number of SNCLs used in the calculation. The slope is close to 1 and the intercept close to 0, indicating good agreement.

the same events using the same Wood-Anderson amplitudes. In the figure, the uncertainties for both magnitudes are shown; they depend primarily on the number of SNCLs contributing to the determination. As both M_L values have uncertainties, the best fit line is calculated using a bilinear L1 norm. Reassuringly, the slope of the line is close to one and the intercept close to zero, indicating agreement between the two M_L systems. Figure 2.78 makes a similar comparison for Southern California earthquakes. Here again, the slope is one, to within the uncertainty, and the intercept is zero.

In a final validation step, we selected a set of 96 earthquakes recorded by both Northern and Southern California stations during the interval 2000-2006 (Figure 2.79). CISM M_L values determined only using Northern (horizontal axis) or Southern (vertical axis) SNCLs also agree well (slope=1, intercept=0).

Significance of Findings

The new state-wide log A_0 and station corrections for determining magnitudes will improve reporting for earthquakes in all of California on several counts. First, M_L was being calculated using only a subset of the currently existing broadband stations in both Northern and Southern California, as only they had been calibrated. In the past 10 years, many broadband stations and strong motion stations have been added to the networks. With the additional stations, M_L determination should become much more reliable. Second, until now Northern (Uhrhammer *et al*, 1996) and Southern California

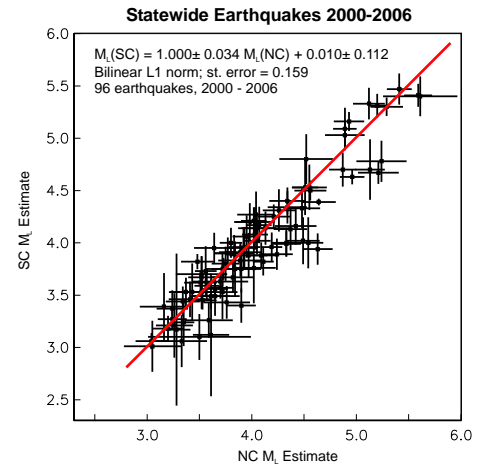


Figure 2.79: CISM M_L for events from 2000-2006 recorded in both Northern and Southern California. The horizontal axis gives M_L for an event calculated using only Northern California SNCLs while the vertical axis gives the M_L from Southern California SNCLs. The greater uncertainty for Northern California M_L results from the lower density of seismic stations.

(Kanamori *et al*, 1999) have been using different log A_0 functions, with their attendant dM_L values for each SNCL. Thus different magnitudes were often determined by Northern or Southern California for an earthquake if it was near the boundary of the reporting regions, or for very large earthquakes in the other region. Figure 2.79 shows that this will no longer be the case. The CISM M_L system is being used in Southern California since February 2008. It will be implemented in Northern California with the transition to the new event processing software.

34.4 Acknowledgements

Work on this project has been supported by the CISM funding of the California Governor's Office of Emergency Services under contract 6023-5 and the United States Geological Survey project 07HQAG0013.

34.5 References

- Richter, C.F., An instrumental earthquake magnitude scale, *Bull. Seismol. Soc. Am.*, 25, 1-32, 1935.
- Gutenberg, B. and Richter, C. F, Earthquake magnitude, intensity, energy and acceleration, *Bull. Seismol. Soc. Am.*, 32, 163-192, 1942.
- Uhrhammer, R., Loper. S. J., Romanowicz, B., Determination of local magnitude using BDSN broadband records *Bull. Seismol. Soc. Am.*, 86, 1314-1330, 1996.
- Kanamori, H., Maechling, P., Hauksson, E., Continuous Monitoring of Ground-Motion Parameters *Bull. Seismol. Soc. Am.*, 89, 311-316, 1999.

35. Seismic Deployments across the Pacific Northwest

Rob Porritt, Richard Allen, Devin Boyarko (Miami University, Ohio), Mike Brudzinski (Miami University, Ohio), Hector Hinojosa (Miami University, Ohio), Gene Humphreys (University of Oregon), Alan Levander (Rice University), Leland O'Driscall (University of Oregon), Yungo Zhal (Rice University)

35.1 Introduction

The Flexible Array (FA) component of the USArray densifies the station coverage already provided by the Transportable Array (TA) and permanent networks. FA experiments are PI driven, supported by the PASSCAL instrument center at New Mexico Tech, and usually last 1-3 years. UC Berkeley is currently involved in two such experiments. The Flexible Array Mendocino Experiment (FAME) with the University of Oregon and Rice University is a dense 79 station network in Northern California and the FlexArray along Cascadia Experiment for Segmentation (FACES) is a 23 station array throughout Oregon and Washington in collaboration with Miami University of Ohio. Both experiments employ Guralp CMG-3T broadband seismometers continuously sampling at 40 samples per second with a flat response to approximately 120 seconds period. The figure displays the station coverage along the US West Coast from just north of San Francisco to Seattle.

35.2 Flexible Array Mendocino Experiment (FAME)

The Mendocino Experiment is designed to image the crust and upper mantle in Northern California around the Mendocino Triple Junction (MTJ). The 79 stations with a 25km average spacing constitute one fifth of all broadband instruments available from the PASSCAL instrument center. This array consists of three main parts: a dense line along the coast from Cape Mendocino to Healdsburg, CA, an evenly spaced distribution throughout inland Northern California, and 14 stations inherited from the Sierra Nevada Earthscope Project (SNEP) in the southeast region of the array. The instruments were primarily installed in two surges: the first in July 2007 and the second in October 2007. The experiment will run through the fall of 2009.

The primary goal of FAME is to investigate and further understand the complex processes and structures involved at the intersection of the North America, Gorda, and Pacific plates where a subduction zone and two transform boundaries meet. This triple junction is migrating to the north relative to a fixed North America plate and thus provides a rare opportunity to study an unstable triple junction. FAME will improve the understanding of how and why the tectonics change from a transform fault to a subduction zone along the west coast.

Gorda crust and overlying sediment subduct and become incorporated in accretionary terranes from the Cas-

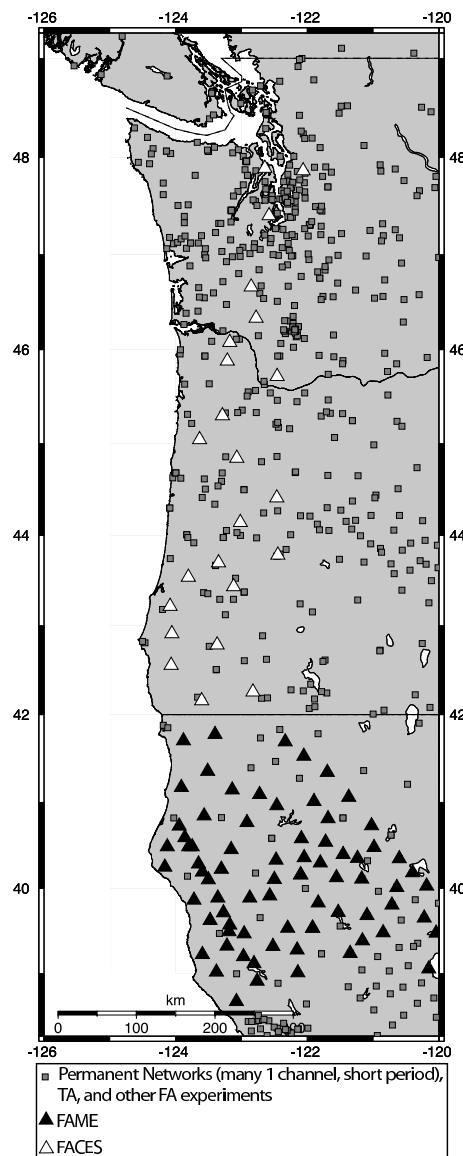


Figure 2.80: Map of current stations available through the IRIS DMC.

cadia subduction zone. This mass flows into the emerging transform margin and becomes structured into the San Andreas strike-slip system. Simultaneously, slab gap opening south of the Gorda slab causes asthenospheric ascent and decompression melting, which magmatically underplates North America near the San Andreas fault. The reprocessed and inflated lithosphere thickens to cre-

ate a small Cape Mendocino orogenic plateau. Meanwhile, erosion moves large fractions of the upper crust back to the subduction zone along tectonically controlled north-trending rivers. Nearby, Gorda-Juan de Fuca subduction results in the Cascade volcanoes, which also contribute to continental crust growth, segregation and recycling. The 3-D seismic velocity models of the crust and upper mantle, which will be developed as part of this project, will be included in event and strong ground motion characterization for Northern California and southern Oregon, a site of potentially devastating great earthquakes.

35.3 FlexArray along Cascadia Experiment for Segmentation (FACES)

FACES is a long array from the California/Oregon border to Seattle deployed at an average spacing of 40km. The majority of stations are in Oregon due to its relatively sparse coverage from permanent networks. The stations were installed in early November 2007. The availability of cellular phone coverage throughout the region allows deployment of modems on most of the stations for real time telemetry. This is the first FA experiment to employ this technology allowing constant monitoring of the state of the network from anywhere with Internet access.

The recurrence of Episodic Tremor and Slip (ETS) is widely observed, but poorly understood. Recent findings show segmentation in recurrence interval of ETS along the Cascadia Subduction Zone (*Brudzinski and Allen, 2007*). The region appears to be split into three primary zones of distinct recurrence intervals. The best preliminary correlation appears to be with the geologic terrain of the continental plate. The increased station density due to FACES throughout this region will better illuminate this phenomenon.

35.4 Innovations in station deployment

A common installation difficulty results from an uneven base upon which the seismometer is set. In these deployments, when possible, self-leveling grout was employed and left to set overnight. This allowed for minimal effort being exerted to level the sensors.

Heat fluctuations can damage both the sensor and the controlling electronics package and temperature changes can become a significant source of noise. To combat these dangers, the sensors are placed in a plastic bag and surrounded with insulating sand. The electronics package is protected by a standard plastic case with reflective material reducing the effect of direct sunlight.

The most exciting development in the current deployments is the utilization of telemetry through cellular phone service. A small cellular modem is installed with the electronics package of the sensor and sends station health information and realtime data back to the

BSL through cell phone towers. FACES is currently the largest deployment using this technology.

35.5 Acknowledgements

The authors would like to thank the following for their hard work installing and servicing various stations: Derry Webb, Marcos Alvarez, Lloyd Carothers, Eliana Arias Dotson, Pat Ryan, Lisa Linville, Pallavi Chethan, Kevin Jensen, Chris McMillan, Stefany Sit, Andrew Tran, Summer Ohlendorf, Dan'L Martinez, Valerie Zimmer, Will Levandowski, Amanda Thomas, Heidi Reeg, Nickles Badger, Tom Owens, Eileen Evans, Holly Brown, Joanne Emerson, Ajay Limaye, Rick Lellinger.

This work has been made possible with the resources available through the PASSCAL instrument center at New Mexico Tech.

Funding has come from NSF grants EAR0643392 and EAR0745934 for FAME and EAR0643007 for FACES.

35.6 References

Brudzinski, M. and R.M. Allen, Segmentation in Episodic Tremor and Slip All Along Cascadia, *Geology*, 907-910, 2007.

36. TMTS, the interactive moment tensor review interface, and the Berkeley Moment Tensor Catalog

Jennifer Taggart, Angela Chung, Rick McKenzie, Peggy Hellweg, and Doug Dreger

36.1 Research Objectives

Since 1992, the BSL has been calculating moment tensor solutions for selected events in Northern California (Romanowicz et al, 1993). At present, moment tensor solutions are calculated in real time for most events with M_w 3.5 and above in Northern California (Pasyanos et al, 1996). The newest version of the program used for reviewing them is a Web-based interface, TMTS. The implementation at UCB is based on a package developed at Caltech (Clinton et al, 2007) and uses the waveform moment tensor inversion code developed by Dreger (Minson and Dreger, 2008). This interface allows analysts to calculate solutions from any computer with Web access and a browser. The interface relies on recent waveforms in the DART and archived data at the NCEDC (see Chapter 3, Section 6.). In addition, TMTS allows the calculation of deviatoric moment tensor solutions and optionally the full moment tensor. In the past, solutions have been stored in the Berkeley Moment Tensor Catalog, a text file with the strike, rake, and dip of the fault plane solution as well as moment, M_w , and a listing of the stations used. The new moment tensor review interface connects to a database where all the information needed to recreate the moment tensor solution is saved (see Figure 2.81). Thus, porting the catalog to the new database required us to recalculate each moment tensor using TMTS.

36.2 Data Set

We selected earthquakes in the Berkeley Moment Tensor Catalog from within the reporting region for recalculation with the new interface and inclusion in the database. Geysers events and events outside the region were set aside. Events from the years 2004 and 2005 were assigned to the USGS for training purposes.

36.3 Approach

When recalculating the moment tensors with the new program, we made an effort to match the original solution as closely as possible. Provided three or more stations were used, the same stations were used for the recalculation. For earthquakes with M_w between 3.5 and 4.0 and with an original solution of high quality, we tried to match the strike, rake, and dip of the original solution to within 10 degrees and the M_w to within .1. For earthquakes with M_w above 4.0, the strike, rake, and dip were to match within 5 degrees and the M_w to within .05. We also attempted to match the value for M_0 .

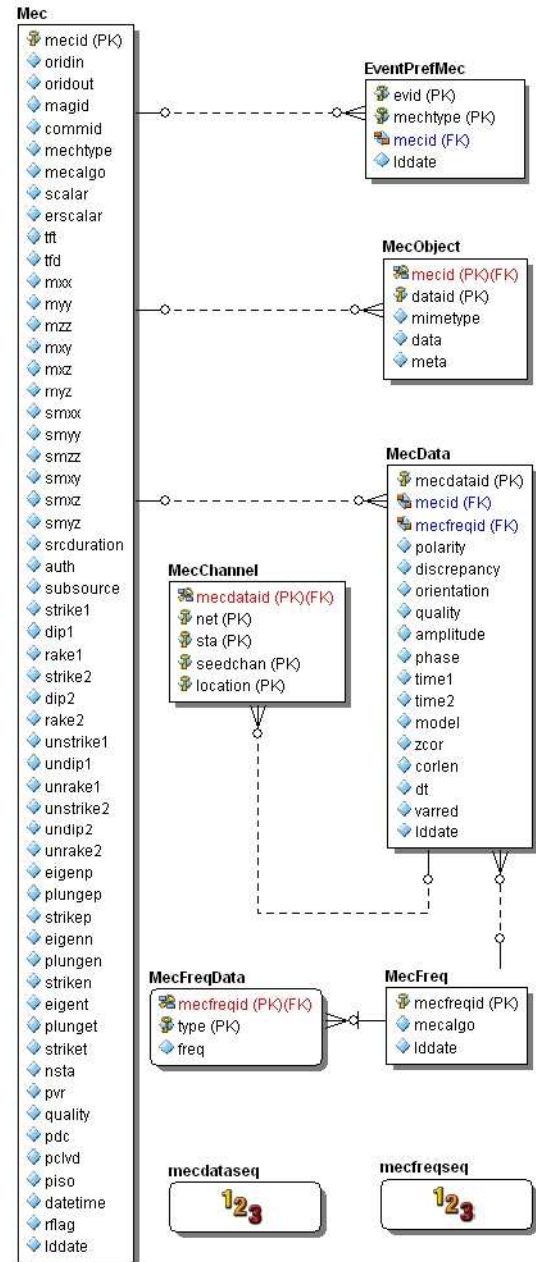


Figure 2.81: Tables and relationships in the database where the moment tensor information is stored.

TMTS has a number of features that make calculation of moment tensors faster. When an event loads, the program automatically selects a set of stations based on distance and azimuth. Stations can be changed using the buttons on the Station Normal page, accessible by a tab in the program. The Station Advanced tab takes the user to a page where other parameters can be changed. Users can choose between three filters, and, for each station, the correlation length between the seismogram and the synthetics can be changed to any value, facilitating analysis of different-sized earthquakes at different distances. Three sets of synthetic Greens functions are available to account for the velocity structure of different areas of California. The Zcorr, a value that determines how far to advance the synthetic seismogram and depends on

station-event distance, can be set to any value for each station to allow fine-tuning and correcting misfits. The depth can be fixed once it is known, allowing quicker recalculations when refining the solution. On the left hand side, next to the tabs, a plot of the variance reduction, a measure of fit, is shown at different depths. This plot can also be shown in another window or tab of the Web browser. A plot of variance reduction over percent double couple and plots of each full solution at the program's 12 chosen depths can be shown in this way as well. In contrast to the previous arrangement, where parameters had to be changed in text files and multiple programs had to be run at the command line, TMTS makes each option available as a button or box.

36.4 Significance of Findings

In Figure 2.82, selected mechanisms from the UCB catalog are compared with the deviatoric moment tensors calculated with the new program. At the top is the August 18, 1998 Bolinas event, an earthquake with an unusual moment tensor for that area. Next is an example of a shallow offshore event. An event from the Parkfield area and the October 31, 2007 Alum Rock event both show a high degree of double couple. In contrast, the Geysers earthquake at the bottom is an event where the compensated linear vector dipole component of the deviatoric solution is important. Also shown is the smaller of the two January 2008 Red Bluff events. Non double couple elements in the solution may be real (*Dreger et al, 2000, Dreger et al, 2008, Ford et al, 2008*), as is likely to be the case for the Geysers event. For small events, they may indicate a relatively poor signal-to-noise ratio.

Approximately 350 moment tensors for earthquakes in Northern California are now in the database with their complete waveforms and all of the parameters involved in their calculation. Table 2.2 shows the year by year breakdown of recomputed events. In Figure 2.83, a comparison of M_w from the old and new moment tensor catalog shows no systematic bias toward higher or lower values with the new program. Plans are in place to make the new Berkeley moment tensor database searchable so that researchers can call up full solutions of events that meet their criteria.

36.5 Acknowledgements

Implementation at UCB would not have been possible without the programming support provided by Alexei Kireev, Pete Lombard, and Doug Neuhauser.

Work on this project was supported by the CISN funding of the California Governor's Office of Emergency Services under contract 6023-5 and the United States Geological Survey project 07HQAG0013.

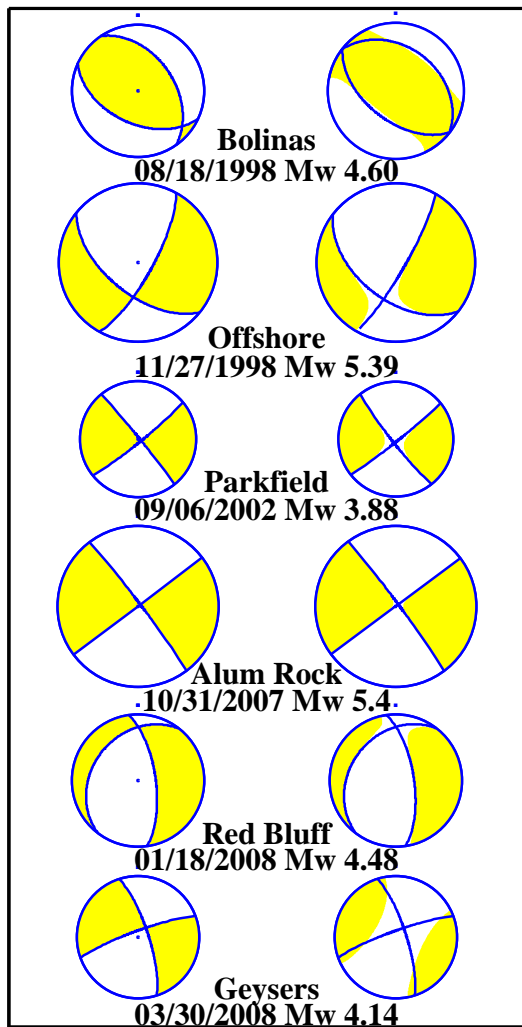


Figure 2.82: Comparison between selected moment tensors in the UCB catalog and deviatoric moment tensors calculated with the new program (right).

Year	Old Catalog	New Catalog
1995	68	50
1996	51	34
1997	68	54
1998	46	39
1999	42	38
2000	29	22
2001	28	24
2002	23	19
2003	41	34
2004	59	USGS
2005	20	USGS
2006	27	23
2007	34	22

Table 2.2: Table of events in old and new catalogs.

Dreger, D., S.R. Ford, and W.R. Walter (2008), Source analysis of the Crandall Canyon, Utah mine collapse, *Science*, **321**, 217, 2008.

Ford, S. R., D. S. Dreger and W. R. Walter, Source Characterization of the August 6, 2007 Crandall Canyon Mine Seismic Event in Central Utah, submitted to *Seism. Res. Lett.*, 2008.

Minson, S. and D. Dreger, Stable Inversions for Complete Moment Tensors, *Geophys. Journ. Int.*, in press.

Pasyanos, M.E., D.S. Dreger, and B. Romanowicz, Toward Real-Time Estimation of Regional Moment Tensors, *Bull. Seism. Soc. Am.*, **86**, 1255-1269, 1996.

Romanowicz, B. D. Dreger, M . Pasyanos, and R. Uhrhammer (1993). Monitoring of Strain Release in Central and Northern California Using Broadband Data, *Geophys. Res. Lett.*, **20**, 1643-1646, 1993.

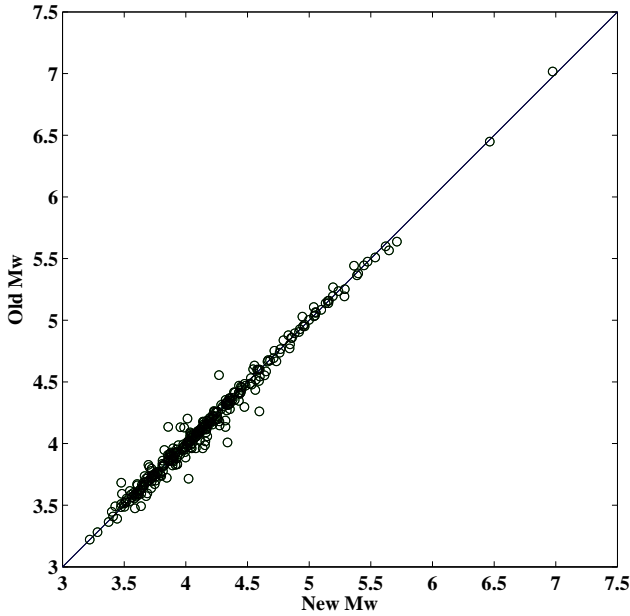


Figure 2.83: Comparison of values of M_w for moment tensors calculated with both programs.

36.6 References

Clinton, J.F., E. Hauksson, and K. Solanki, An Evaluation of the SCSN Moment Tensor Solutions: Robustness of the M_w Magnitude Scale, Style of Faulting, and Automation of the Method, *Bull. Seism. Soc. Am.*, **96**, 1689 - 1705, 2006.

Dreger, D. S., H. Tkalic, and M. Johnston, Dilational processes accompanying earthquakes in the Long Valley Caldera, *Science*, **288**, 122-25, 2000.

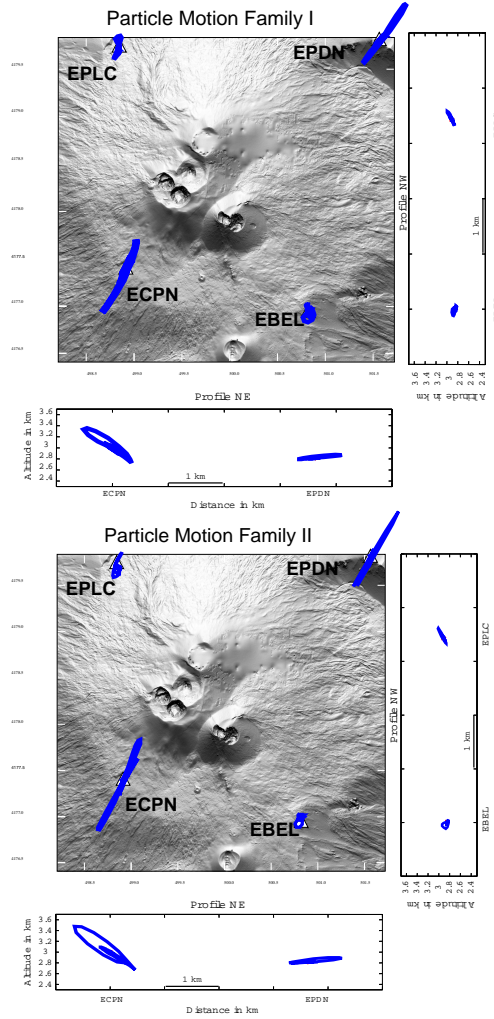


Figure 2.84: From Chapter 2, Section 23: Particle motion for very long period (VLP) events of Family I (top) and Family II (bottom). The map view shows particle motion in the horizontal plane; the two cross sections (to the right of and below the maps) show particle motion across the crater from ECPN to EPDN and from EPLC to EBEL.